MICROSTRUCTURE AND FUNCTIONALITIES IN EPITAXIAL MANGANITES BASED VERTICALLY ALIGNED NANOCOMPOSITE THIN FILMS

A Dissertation

by

MENG FAN

Submitted to the Office of Graduate and Professional Studies of
Texas A&M University
in partial fulfillment of the requirements for the degree of

DOCTOR OF PHILOSOPHY

Chair of Committee,	Haiyang Wang
Co-Chair of Committee,	Jun Kameoka
Committee Members,	Arum Han
	Choongho Yu
Head of Department,	Miroslav M. Begovic

May 2017

Major Subject: Electrical Engineering

ABSTRACT

Vertically aligned nanocomposite (VAN) presents as a novel material platform for creating high-quality self-assembled, nano-pillars of one phase in matrix of another structures. In the past decade, extensive efforts have been devoted and demonstrated the great potential of VAN thin films in enabling novel and enhanced functionalities. Mixed valence $La_{1-x}Sr_xMnO_3$ (LSMO) exhibits unique magnetic and transport properties, promising for spintronic device applications. In this dissertation, novel and enhanced magnetic and electrical functionalities including low-field magnetoresistance (LFMR), magnetic exchange bias (EB), etc., are explored using VAN design, with a focus on the LSMO based materials.

By selecting CeO_2 and CuO as the secondary phases and optimizing the growth conditions, large and tunable LFMR in a wide temperature region has been achieved in LSMO: CeO_2 and LSMO: CuO VAN films. Detailed analysis indicate that the phase boundaries, the secondary phase domain size, and the strain states in the films contribute to the enhanced LFMR in different temperature regions.

Perpendicular exchange bias (PEB) is desired in next-generation memories to offer perpendicular unidirectional magnetic anisotropy. By confining ferromagnetic (FM) and antiferromagnetic (AFM) hetero-interfaces coupling in the vertical direction, strong PEB effect are demonstrated in the LSMO: $LaFeO_3$ VAN films. The microstructures, PEB behavior correlated with the composition variation, strain tuning and cooling field effect

are analyzed. A spin-glass (SG) state at the vertical interfaces is ascribed to be responsible for the remarkable PEB here.

Conventional VAN films tend to present random distributed pillars in matrix structure. Achieving spatial ordering is timely demanded. Here, a novel approach are introduced for one-step self-organization growth of VAN films with long range ordering by substrate nano-templating. The $SrTiO_3$ (001) substrates with surface nanopatterns of alternating chemical terminations developed by thermal treatment are demonstrated to be effective for selective growth of well-ordered VAN structures, using LSMO: CeO_2 as a prototype. Remarkable enhanced magnetic and transport properties is achieved for the templated films.

The studies in this dissertation exploited the capability of the unique VAN structures in enhancing the magnetic and transport performance of LSMO based nanocomposite materials. Great enhanced LFMR, PEB as well as well-ordered nanostructures have been achieved. The VAN design provide a powerful way in enabling novel and enhanced functionalities, promising for spintronic devices applications.

DEDICATION

To my parents and my husband

ACKNOWLEDGEMENTS

I would like to sincerely thank my advisor, Professor Haiyan Wang, for her professional advice and guidance throughout my Ph. D. study. I also appreciate her great care, encouragement, support and trust for my research and life. I've benefited a lot from her insightful thought, extensive and solid knowledge, passion for science and rigorous attitude. She always gives us freedom and trust to pursue high quality research that we're interested in and simultaneously provides us with very impressive discussion and support. I'm also impressed by her hard work. Working with Prof. Wang has made me more experienced, independent and mature. I feel grateful to work in her group.

I'd like to acknowledge all my committee members, Dr. Jun Kameoka, Dr. Arum Han, Dr. Chongho Yu for their great help and supervision on my research. I want to thank my colleagues, Dr. Wenrui Zhang, Dr. Jie Jian, Dr. Liang Jiao, Dr. Fauzia Khatkhatay, Dr. Clement Jacob, Dr. Jijie Huang, Leigang Li, Han Wang, Bruce Zhang, Zhimin Qi, Xingyao Gao, Xing Sun, Xuejing Wang for their collaboration as well as valuable discussion, which helped a lot throughout my research. I also want to thank them for the friendship and support during my study.

I also like to acknowledge the faculty and staff at the Microscopy and Imaging center and Materials Characterization Facility for their help with equipment training and measurement. Thank the staffs and faculty in ECE department for their assistance and support for my study.

Finally, I would like to thank my parents and my husband for their love, support and encouragement.

CONTRIBUTORS AND FUNDING SOURCES

This work was supervised by a dissertation committee consisting of Professor Haiyan Wang of the Department of Electrical and Computer Engineering and Professor(s) Jun Kameoka and Arum Han of the Department of Electrical and Computer Engineering and Professor Choogho Yu in Department of Chemistry Engineering.

All work for the dissertation was completed by the student, in collaboration with Dr. Wenrui Zhang, Dr. Jijie Huang, Han Wang, Leigang Li, Xing Sun, Dr. Liang Jiao, Prof. Xinghang Zhang of the Department of Material Science and Engineering and , Dr. Jie Jian, Bruce Zhang, Dr. Fauzia Khatkhatay in the Department of Electrical and Computer Engineering.

This work was supported by the U.S. National Science Foundation under Grant Number: DMR-1643911 and DMR-1565822.

NOMENCLATURE

AFM	Antiferromagnetic
AFM	Atomic force microscopy
CMR	Colossal magnetoresistance
DE	Double exchange
EB	Exchange bias
EDX	Energy dispersive X-ray
FC	Field cooling
FE	Feroelectric
FM	Ferromagnetic
GMR	Giant magnetoresistance
H	Magnetic field
HAADF	High angle annular dark field
LFMR	Low-field magnetoresistance
M	Magnetization
MR	Magnetoresistance
MTJ	Magnetic tunneling junction
PEB	Perpendicular exchange bias
PFM	Piezoresponce force microscopy
PLD	Pulsed laser deposition
PPMS	Physical property measurement system
R	Resistance

RSM	Reciprocal space mapping
STEM	Scanning transmission electron microscopy
SPM	Scanning probe microscopy
T	Temperature
Tc	Curie temperature (for ferroelectric, ferromagnetic)
T_N	Antiferromagnetic Neel Temperature
TEM	Transmission electron microscopy
TMR	Tunneling magnetoresistance
VAN	Vertically aligned nanocomposites
VSM	Vibrating sample magnetometer
XRD	X-ray diffraction
ZFC	Zero field cooling

TABLE OF CONTENTS

Page

LIST OF FIGURES

Page

LIST OF TABLES

Page

CHAPTER I

INTRODUCTION

Vertically aligned nanocomposite (VAN), in which two immiscible materials can grow epitaxially together on substrate, has emerged as a new platform for exploring novel and enhanced functionalities in materials engineering. In the past decade, extensive efforts have been devoted to demonstrate the fascinating capability of the high-quality, size-tunable VAN structures in enabling interface-coupling and strain tuning phenomenon [1 2]. In this chapter, the background of the oxide materials, functionalities, and the motivation of the thesis research are discussed.

1.1 Functional metal oxide materials

1.1.1 Overview of functional oxides

Metal oxide is an important class of materials for both science and technology, and has attracted extensive efforts for investigation. The intrinsic complexity of the composition and structure can lead to varieties of properties and functionalities [3456]. With multiple interactive coupling of the lattice, charge, spin and orbital, metal oxides can show off a wide range of properties in respect of electric, magnetic, thermal, and optical as well as multi-functionalities, e.g., from insulator, semiconductor to metallic conductor, superconductor; paramagnetic- antiferromagnetic, to ferromagnetic; dielectric to ferroelectric, etc. For decades, metal oxide materials have been explored for wide applications, revolutionizing human life. For example, oxide semiconductors such as ZnO, InGaZnO (IGZO) can be used as channel materials in thin film transistors for high

performance displays [7, 8]; Doped ZnO or TiO_2, such as Al: ZnO (AZO), $InTiO_3$ (ITO) can be used as transparent conducting oxides (TCOs) in solar cells; $YBa_2Cu_3O_{7-x}$ (YBZO) has been investigated to be superconducting at high temperature (with curie temperature of tens of kelvin). Oxide ferroelectric including $BaTiO_3$, $Pb[Zr_xTi_{1-x}]O_3$ (PZT), has found wide applications in sensors, actuators, as well as transistor and memory devices. Ferromagnetic materials can be used in novel spintronic devices, like magnetoresistive random-access memory (MRAM), magnetic read head and sensors, etc. Next generation devices based on magnetoelectric coupling are strongly potential for low power consumption data storage applications. Phase transition in particular materials, such as VO_2, is interesting for resistive switching memories, as well as smart window usage.

1.1.2 Functional oxide thin films

Great improvement has been achieved in engineering the oxide bulk materials in terms of composition and microstructures for enhanced properties. While for integration into solid state devices, metal oxide thin films are essential and can provide more flexible tunability of the microstructure and functionalities with the rich forms of single phase epitaxial/amorphous/polycrystalline or nanocomposites [7, 9, 10]. With the development of substrates and advanced growth techniques, oxide thin films have made significant progress to explore novel phenomenon as well as enhanced functionalities. Examples include multi-ferroicity [9, 11, 12], high temperature superconductors [13], metal-insulator phase transition in VO_2 [14, 15], resistive switching in oxides of Cu_xO, TiO_2, doped $SrTiO_3$, Ta_2O_5 [16, 17], magnetoresistance [18, 19, 20], novel ionic transport [21], etc.

By taking advantage of the combination of properties of different materials as well as the strong interface coupling effects, hybrid nanocomposite thin films can obtain unattainable electronic, magnetic, optical, thermal or other properties than the single phase counterpart, providing a powerful way for exploration of novel functionalities and stabilization of new states. Hybrid nanocomposite thin films usually comes up with structures of multilayers (2-2 type), particular (0-3 type) and heteroepitaxial vertically aligned nanocomposite (VAN) (1-3 type), as displayed in Figure 1.1.

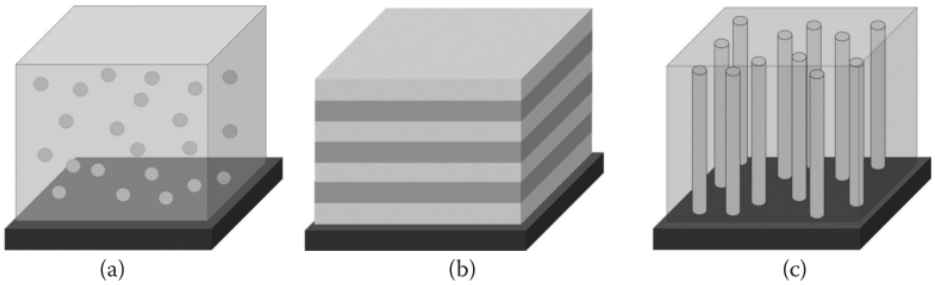

Figure 1. 1 Microstructures of hybrid nanocomposite thin films a) nanoparticles in matrix type nanocomposites (0-3 type), b) multilayer nanocomposites (2-2 type), and c) vertically aligned nanocomposites (1-3 type)[22].

1.1.3 Crystal structures of functional oxide materials

Functional metal oxides exhibit a wide variety of crystal structures, which are correlated to the unique properties. The structure as well as the composition and bonding determine directly on the materials properties. Table 1.1 gives a brief category of oxides crystal structures. Generally, metal oxides can be categorized into binary, ternary oxides based on the number of cation elements. Common binary oxide structures include rock salt, wurtzite, fluorite, rutile and corundum. Ternary oxides exhibit a wide range of

structures, which include ilmenite ($(AB)O_3$; A, B=metal), spinel (AB_2O_4), perovskite (ABO_3) and more complex perovskite derived structures (e.g. Ruddlesden-Popper series Dion-Jacobson, Aurivillius phases as well as layered perovskite structures). A wide range of properties in terms of ferroelectricity, magnetism, multiferroicity, conductivity, etc can be derived with the varieties of structures.

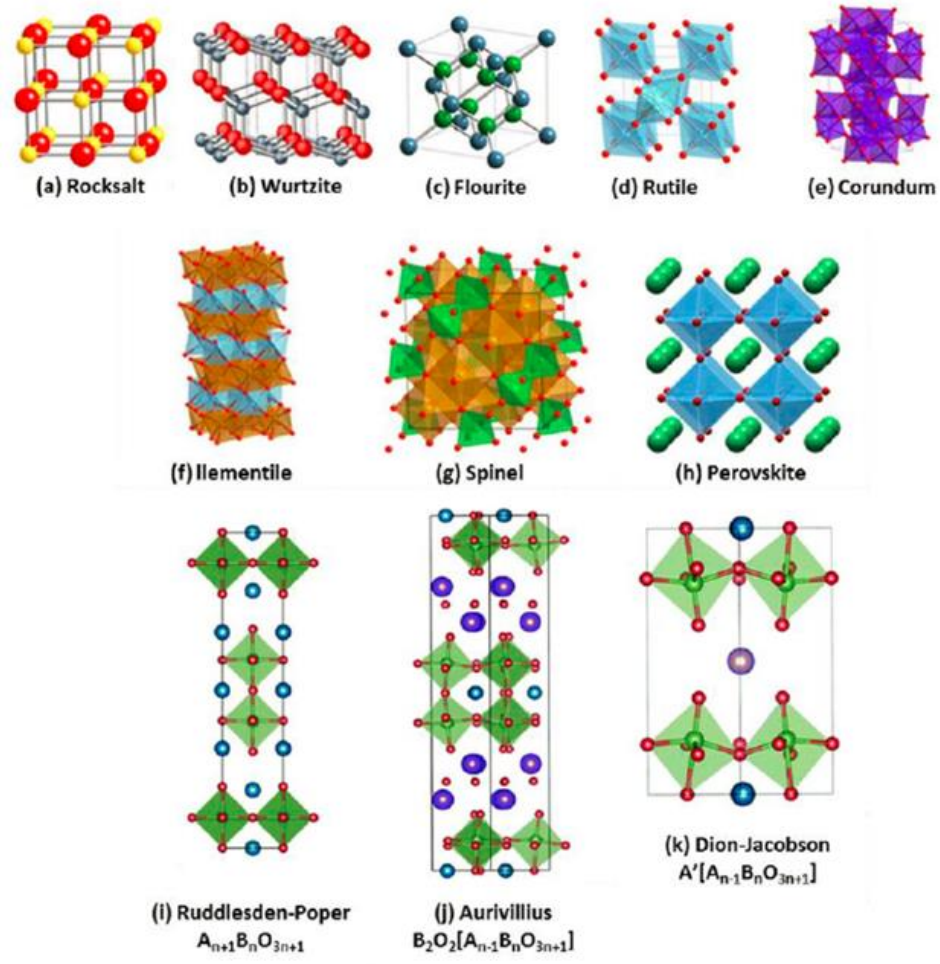

Figure 1. 2 Schematic illustrations of oxide crystal structures[23, 24].

Table 1. 1 Category and examples of common binary, ternary oxides

System	Crystal Structure	Representative Materials
Binary oxides	Rock Salt	MgO, CoO, NiO, MnO, Sm_2O_3, Nd_2O
	Wurtzite	ZnO, BeO
	Fluorite	CeO_2, ZrO_2, PrO_2
	Antifluorite	Li_2O, Na_2O, K_2O
	Cuprite	Cu_2O, A_2O, Pb_2O
	Rutile	TiO_2, IrO_2, MoO_2, RuO_2, SnO_2, WO_2,
	Corundum	Al_2O_3, V_2O_3, Cr_2O_3
Ternary oxides	Ilmenite	(Fe, Co, Ni, Mn)TiO_3, $LiNbO_3$, $NiMnO_3$
	Spinel	$LiTi_2O_4$, $CoFe_2O_4$, $MgAl_2O_4$, $NiFe_2O_4$
	Perovskite	$SrTiO_3$, $BaTiO_3$, $La_xSr_{1-x}MnO_3$, $BiFeO_3$
	Layered perovskite	$YBa_2Cu_3O_{7-x}$
	Ruddlesden-popper series	$A_{n+1}B_nO_{3n+1}$ (Sr_2RuO_4, $Sr_3Ti_2O_7$)
	Aurivillius phases	$[Bi_2O_2]$-$[A_{n-1}B_2O_7]$ (Bi_2WO_6)
	Dion-Jacobson	$A[A_{n-1}B_nO_{3n+1}]$ ($KLaNb_2O_7$)

1.1.3.1 Crystal structure of $La_{1-x}Sr_xMnO_3$

Mixed valence $La_{1-x}Sr_xMnO_3$ (LSMO), which belongs to manganites and exhibits unique magnetic and transport properties, has gained significant interests in the past decades [25, 26, 4]. With unusual strong correlation between the charge, spin and orbital, the LSMO family materials can exhibit rich properties ranging from paramagnetic insulator, ferromagnetic insulator, ferromagnetic conductor to paramagnetic metallic state. The general chemical formula for mangantites is $A_{1-x}B_xMnO_3$. The A-cations usually are La, Pr, and Nd and B-cation Sr, Ca, and Ba, etc [4]. The crystal structure of $La_{1-x}Sr_xMnO_3$ is cubic perovskite, shown as Figure 1.3. It has a corner shared octahedral in the unit cell with A and B cations coordinated with 12 and 6 oxygen ions, respectively. The different and easy doping of B cations can result in a drastic change in conductivity and ferromagnetic ordering concurrently. The phase diagram in respect of doping concentration and temperature is shown in Figure 1.4 [4]. Different phase regions of PMI, FMI and FMM can be achieved.

Another important concept for understanding manganites' structure and behavior is the "tolerance factor", which is strongly correlated with the lattice distortion, as all the manganites exhibit lattice distortion with doping. For an ideal cubic perovskite, the unit cell lattice parameter a, is geometrically related to the ionic radii (r_A, r_B, and r_O) as described in following equation [27],

$$a = \sqrt{2}(r_A + r_O) = 2(r_B + r_O)$$

The ratio of the two expressions for the cell length is called the Goldschmidt's tolerance factor t. It allows us to estimate the degree of lattice distortion. It can be described as

$$t = (r_A + r_O)/\sqrt{2}(r_B + r_O)$$

The tolerance factor t directly affects the structure and chemical bondings of the materials, thus the properties. In the case of $SrTiO_3$, a prototype ideal cubic perovskite, r_A = 1.44 Å, r_B = 0.605 Å, and r_O = 1.40 Å, resulting in t = 1. A deviation from 1 in the value of t represents a distortion to the cubic unit cell, which can result in a rotation of the $[BO_6]$ octahedral. Figure 1.4b exhibit the phase diagram of $A_{0.7}B_{0.3}MnO_3$ in respect of temperature and tolerance factor t for different composition [28].

Among the rich manganites, $La_{0.7}Sr_{0.3}MnO_3$ (LSMO) has the highest Curie temperature reported to be ~360K. It's also predicted and demonstrated to be a half metallic oxide with almost 100% spin polarization of electrons, which is highly desired for large tunneling magneto-resistance in applications of magnetic tunnel junction devices [29]. LSMO refers to $La_{0.7}Sr_{0.3}MnO_3$ in the following dissertation. LSMO has a pseudo-cubic structure with a bulk lattice parameter of 3.87 Å.

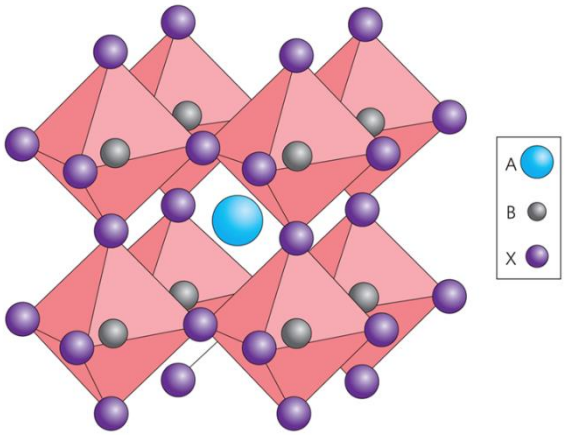

Figure 1. 3 Cubic perovskite crystal structure of lanthanum manganites. [30]

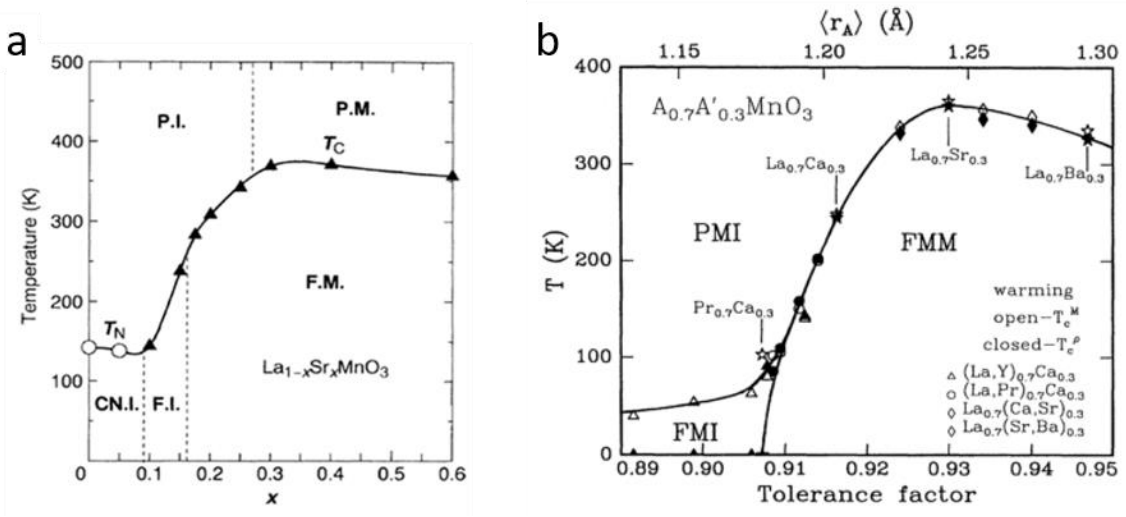

Figure 1. 4 a) Phase diagram of $La_{1-x}Sr_xMnO_3$ in respect of temperature and doping level. [4] b) Phase diagram of temperature vs tolerance factor for manganites $A_{0.7}B_{0.3}MnO_3$. [28]

1.1.3.2 Crystal structure of CeO_2, CuO

Cerium (IV) oxide (CeO_2) exhibits the fluorite crystal structure with lattice constant a=5.411 Å. The fluorite structure consists of a face-centered cubic (f.c.c.) unit cell of cations with anions occupying the octahedral interstitial sites. This can also be seen as a superposition of an f.c.c. lattice of cations (Ce^{4+}) with lattice constant a, and a simple

cubic (s.c.) lattice of anions (O^{2-}) with lattice constant of a/2. In this structure (shown schematically in Figure 1.5), each cerium cation is coordinated by eight nearest-neighbor oxygen anions, while each oxygen anion is coordinated by four nearest-neighbor cerium cations.

Fluorite structure oxides exhibit high radiation tolerance and high thermal stability. CeO_2 is a wide bandgap insulator that has gained widespread popularity as an automotive emissions-reduction catalyst [31] and, more recently, as an oxygen ion transporting electrolyte in solid-oxide fuel cells.

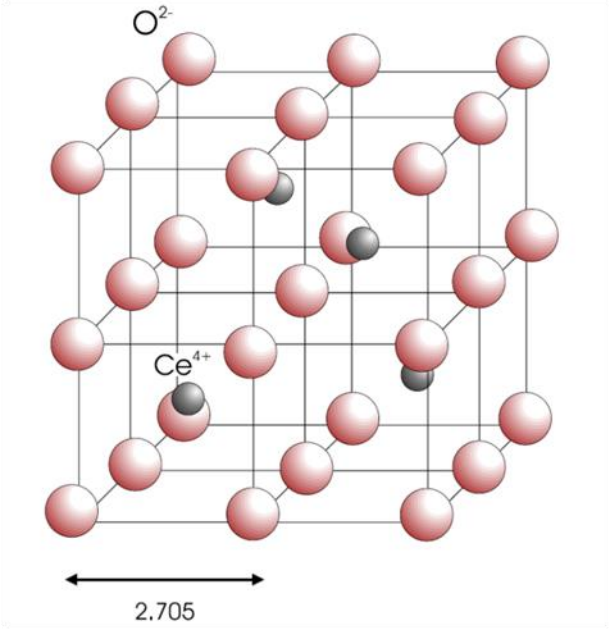

Figure 1. 5 Crystal structure of CeO_2 [32].

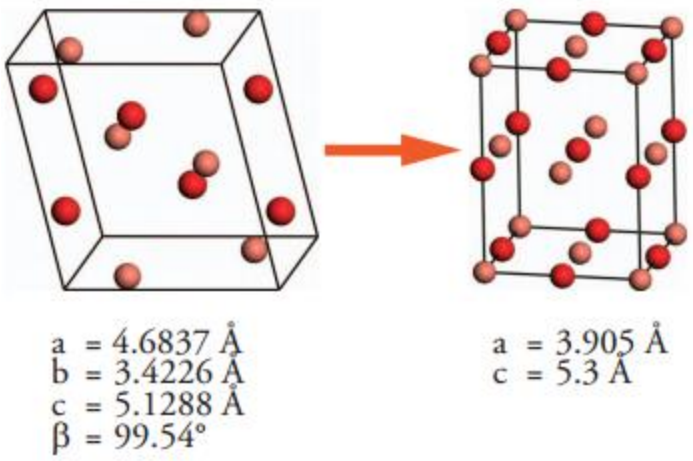

Figure 1. 6 CuO crystal structure [33]. The lighter colored atoms represent oxygen and the darker colored atoms represent copper.

Copper (II) oxide (CuO) is the only stable compound in the phase diagram of Cu-O system at 1 atm pressure. The natural structure of CuO, is monoclinic, different to the usual rocksalt structure for other monoxides. In CuO, the copper atom is coordinated by 4 oxygen atoms in an approximately square planar configuration [33]. The monoclinic tetramolecular cell has the following parameters: a = 4.6837 Å, b = 3.4226Å, c = 5.1288 Å, with β = 99.54°, shown in left of Figure 1.6. CuO is a p-type semiconductor, with a narrow band gap of 1.2 eV. Wide applications such as resistive switching memories, dry cell batteries has been developed with CuO. Meanwhile CuO displays antiferromagnetic properties with a Neel temperature of ~215K. Exchange bias effect has been observed in CuO nanoparticle systems. Recently tetragonal CuO has been developed with a nearly rocksalt structure through the use of epitaxy in ultrathin CuO film on STO substrate [34], shown as right of Figure 1.6.

1.1.4 Functionality

1.1.4.1 Ferroicity

Ferroic is related to the ordered phases and phase transition [35] and refers generally to ferroelectric (FE), ferromagnetic (FM) , ferroelastic, and ferrotoroidic. Upon cooling the materials down below specific temperature of Tc (Curie temperature), the materials undergo a spontaneous phase transition from disorder to ordered phase. In ferroelectrics, a spontaneous dipole moment is induced when lowering the temperature below Tc, leading to macroscopical spontaneous charge polarization. For ferromagnetic materials, spontaneous magnetization can be induced in the absence of external magnetic field. In ferroelastic crystals, in going from the nonferroic (or prototypic phase) to the ferroic phase, a spontaneous strain is induced. Such orders (charge polarization for FE, magnetization for FM, strain for ferroelastic) can be switched under external field and a hysteresis behavior exist due to the ferroicity. Figure 1.7 gives the schematic representation and hysteresis cycles of the four primary ferroic orders.

The spontaneous magnetization or charge polarization make the ferroic materials special for applications in non-volatile memories, as well as transistors such as FEFET, and spintronic transistors. Multiferroics are defined as materials those exhibit more than one of the primary ferroic orders, i.e, ferromagnetism, ferroelectricity, ferroelasticity in the same phase. The Multilayer devices such as magnetic tunneling junction, ferroelectric tunneling junction as well as multiferroic tunneling junction have been developed recently. The non-destructive reading process, fast switching and low power consumption of such devices offer great opportunity in next generation data storage and processing technique.

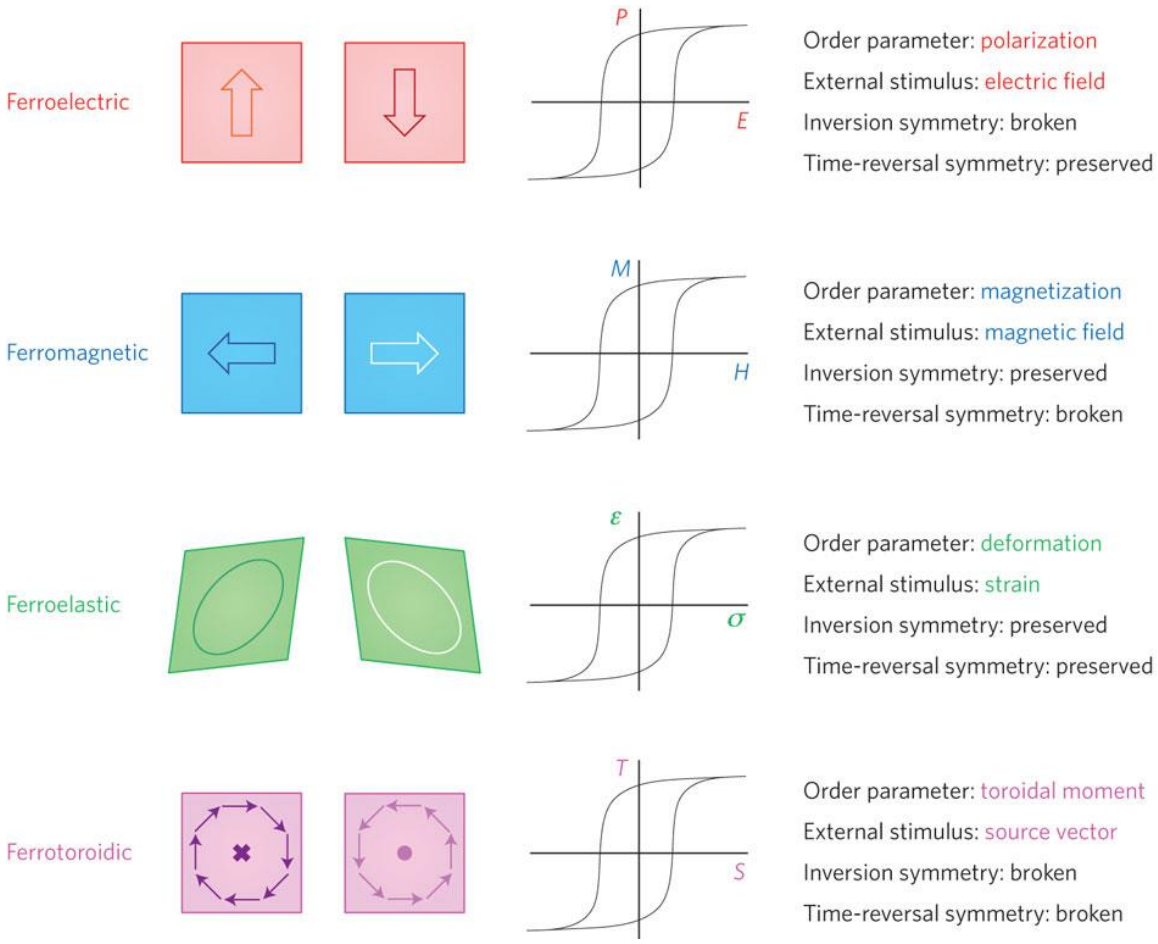

Figure 1. 7 Schematic representation and hysteresis cycles of the four primary ferroic orders [35].

1.1.4.2 Magnetoresistance

Magnetoresistance (MR) refers to the change of the resistivity of the materials under external applied magnetic field. The value is defined as MR=(R(H)-R(0))/R(0), in which R(H) is the resistance of the sample under a magnetic field H, and R(0) corresponds that of H = 0. The MR effect has been widely investigated for applications in magnetic data storage and sensors since the first discovery in 1856. Various materials, architectures are demonstrated to show MR effect. Depending on the structures and mechanisms, MR

effect can be classified as giant magnetoresistance (GMR), tunneling magnetoresistance (TMR), anisotropic magnetoresistance (AMR), colossal magnetoresistance (CMR) and low field magnetoresistance (LFMR).

Giant magnetoresistance means that the MR value significantly exceeds the anisotropic magnetoresistance, which has a typical value within a few percent [36]. Giant magnetoresistance (GMR) refers to a quantum mechanical magnetoresistance effect observed in thin-film multi-layered structures consisting of alternating ferromagnetic and non-magnetic metallic layers. Figure 1.8 gives a typical GMR behavior in Fe/Cr multilayered structures [36]. With the discovery of GMR, the 2007 Nobel Prize in Physics was awarded to Albert Fert and Peter Grünberg. In GMR system, depending on the magnetization directions of adjacent ferromagnetic layers, the electrical resistance can suffer a significant change, i.e, the resistance is relatively low for parallel alignment and relatively high for antiparallel alignment. The magnetization direction can be controlled by applying an external magnetic field. The GMR effect is based on the dependence of electron scattering on the spin orientation.

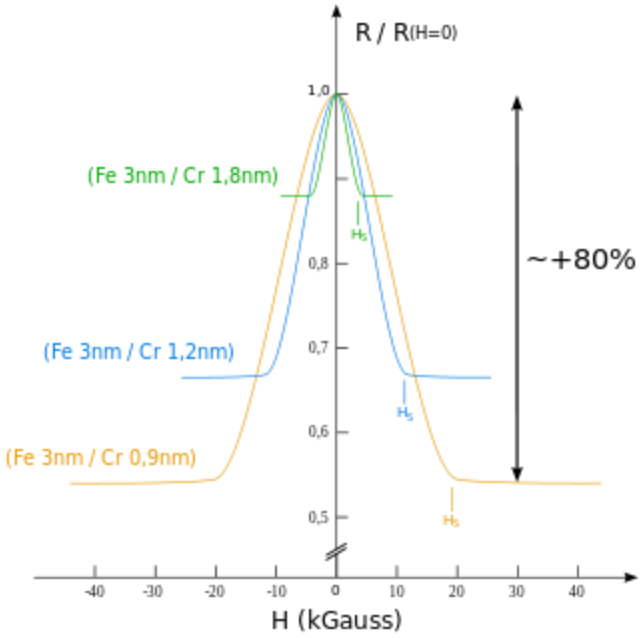

Figure 1. 8 Normalized resistivity of Fe/Cr multilayers as a function of magnetic field measured at 4.2 K [36].

CMR is a MR effect associated with a ferromagnetic-to-paramagnetic (PM) phase transition. Near the phase transition temperature, large MR effect is observed, which involves rich physics phenomena and receives significant research interests in the field of condensed matter physics. Since its discovery in 1950 by Jonker and coworkers, much research efforts have been devoted to understand the fundamental physics, which relates to a strong interplay among the spin, charge, orbital and lattice degrees of freedoms. Initially it is discovered in mixed-valence perovskite manganites in the 1950s by G. H. Jonker and J. H. van Santen [37]. A first theoretical description in terms of the double-exchange mechanism was given early, shown in Figure 1.9. In this model, the spin orientation of adjacent Mn-moments is associated with kinetic exchange of e_g-electrons [38]. In the parent compound, $LaMnO_3$ (insulating antiferromagnet, superexchange), Mn is in

a 3+ valence state. Upon doping by a divalent element (Ca^{2+}, Sr^{2+}, Ba^{2+}, Pb^{2+}) the Mn is driven into a mixed valence state Mn^{3+}/Mn^{4+}. The hopping of e_g electrons from Mn^{3+} to Mn^{4+} (the simultaneous jumps of the e_g electron of Mn^{3+} to O p-orbital and the electron with the same spin form O p-orbital to the empty e_g orbital of Mn^{4+}) is the basis for the conduction behavior and the ferromagnetic coupling in doped manganites. The electron hopping probability varies as the cosine of angle Θ between two spins in neighboring e_g orbitals, which allows larger mobile electron transfer at a lower Θ. The external magnetic field can align the core spins in a higher order from a pristine disorder states and then facility the electron hopping, leading to a drop in resistivity. In other words, alignment of the Mn-spins by an external magnetic field causes higher conductivity. Figure 1.10 gives a typical temperature dependent resistance (R-T) and magnetization (M-T) behavior of LSMO, the resistance is much decreased with applied magnetic field.

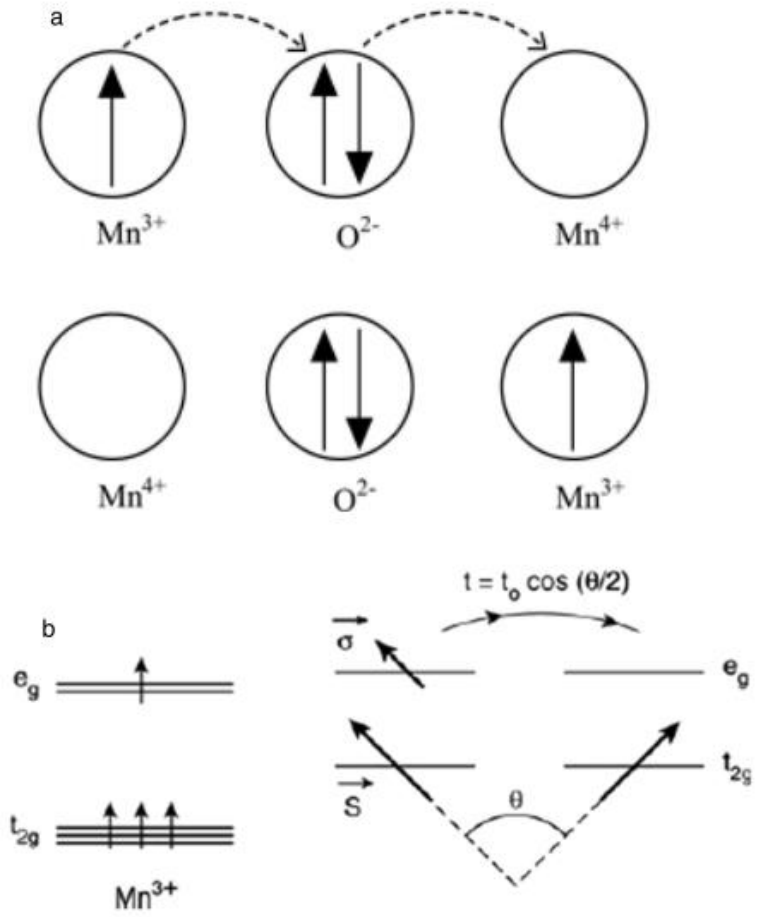

Figure 1. 9 a) Schematic representation of the double exchange mechanism proposed by Zener; b) sketch of de Gennes spin-canted states [38].

However the double exchange model could not explain the high insulating-like resistivity above the transition temperature. Although still no complete understanding of the phenomenon, there have been a variety of theoretical and experimental work, including DE interaction, Jahn-Teller distortion, super-exchange interaction and Hund's coupling, providing a deeper understanding of the relevant effects.

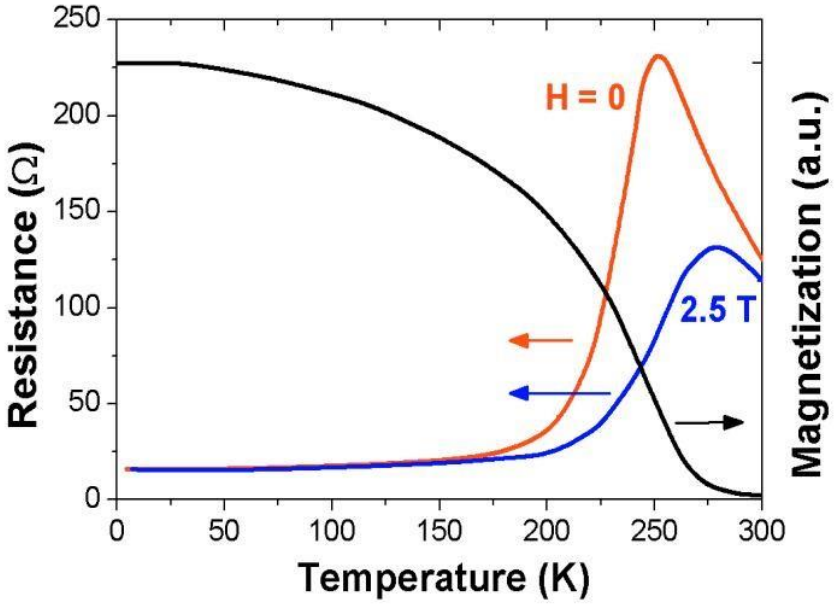

Figure 1. 10 Temperature dependent resistance (R-T) and magnetization (M-T) behavior of LSMO [39].

Low-field magnetoresistance refers to the large MR effect at a relative low magnetic field (typically no more than 1T). The LFMR mainly relies on extrinsic transport effect and is increased by spin-polarized tunneling through electronic barrier across structural disorders such as grain boundaries and phase boundaries[40, 41, 42]. Thus a variety of work to enhance the LFMR effect has been done by creating artificial boundaries in polycrystalline films or introducing secondary phases in nanocomposite films. Representative studies in this aspect include the growth of $La_{0.7}Ca_{0.3}MnO_3$ (LCMO) films on bicrystal substrates [42], and LSMO or LCMO-based nanocomposite thin films [26, 43, 44].

1.1.4.3 Exchange bias

Exchange bias (EB) refers to a shift of the magnetization hysteresis loop along field axis after field cooling process. It has gained great interest since the discovery in

1950s [45]. The EB effect usually occurs with the magnetic coupling across the interface shared by a ferromagnet (FM) and an antiferromagnet (AFM) when cooled in magnetic field through the Neel temperature (TN) of the AFM [46, 47, 48]. The classic schematic mode of EB is shown in Figure 1.11. At temperature of TN<T<Tc (i), the FM phase shows aligned FM spins while the AFM phase displays disordered spins. When the system is cooled down under a magnetic field across TN, the interfacial spins of the AFM phase will be aligned to the same direction of the FM spins (for interfacial FM coupling) (ii). When the field reverses, the interfacial AFM spins can exert a blocking torque on the FM spin rotation, resulting in a larger reversal field (iii). However, when the FM spins are reversing to the same direction of the interfacial AFM spins (v), the FM spins are easily reversed aided by the exchange coupling, leading to a relatively small reversal field. The 'aid and drag' effect lead to the difference between the absolute value of coercive field (iii and v) for increasing and decreasing magnetic field, resulting the shift along the field axis observed in the magnetization hysteresis loops.

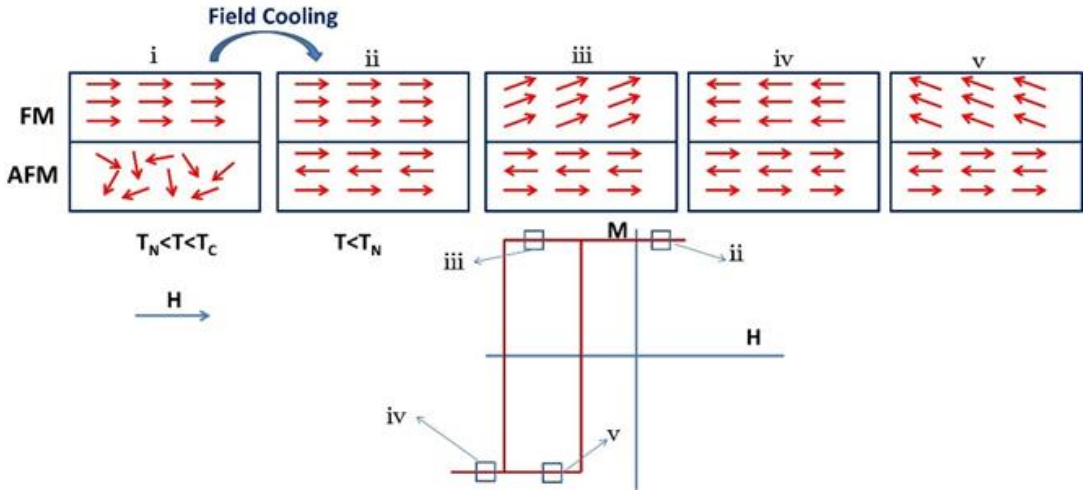

Figure 1. 11 Schematic mode of exchange bias [48].

As discussed above, in the EB system, the FM spins can be 'pinned' in one direction by interface coupling with the AFM spins. Such unidirectional magnetic anisotropy make the EB effect critical for applications in numerous spintronic devices, i.e., magnetic recording read heads and magnetic memory [49, 50]. So far, a variety of exchange coupled systems in forms of nanoparticles, inhomogeneous materials, nanocomposites, thin films have been developed and investigated [49]. In addition to FM/AFM interfaces, this effect has also been extensively explored and reported in FM/spin-glass (SG), [515253], FM/non-magnetic interfaces, [54,55] and FM/paramagnetic [50] interfaces recently. Several theoretical models are proposed to understand the EB effects observed [46], based on the assumption about the interface magnetic structure, ranging from ideal interface, interfacial AFM domain walls, random field model, spin-flop perpendicular interfacial coupling and compensated or uncompensated AFM interface layer due to the interface defects.

1.2 Vertically aligned nanocomposite thin films

1.2.1 Overview of VAN thin films

Hybrid composite materials have attracting lots of interest due to their advantage to combine different materials' unique functionality together to obtain unattainable properties [56, 57]. In hybrid composite thin films, different materials can be grown together on the substrate, leading to coupling of the phases, thus could form fascinating properties that cannot be obtained by single phase materials [58]. In general, nanocomposite thin films can be classified to 3 categories according to their microstructures, i.e, particular nanocomposites (0-3 type; Figure 1.1a), multilayered thin films (2-2 type; Figure 1.1b), and heteroepitaxial VAN thin films (1-3 type; Figure 1.1c) as discussed above. Among them, the VAN film has been emerging as powerful new system for materials engineering during last decade owing to its key advantages over conventional planar heterostructures, including simple self-assembled growth, high density of vertical heterointerfaces and efficient strain control, and strong coupling effects. Great progress has been made for a wide range of nanoscale functionalities using the unique VAN architecture.

The two-phase VAN system was first demonstrated in $La_{0.67}Ca_{0.33}MnO_3$: MgO (LCMO: MgO) thin films in 2002 [26, 59]. A systematic strain tuning with the MgO concentration variation was observed together with a structural phase transition, leading to a tunable magnetotransport properties in the films. In 2004, new $BaTiO_3$: $CoFe_2O_4$ (BTO: CFO) system was developed to have spinel CFO nanopillars embedded in BTO matrix structure [60], multiferroic coupling effect was demonstrated in such films through the elastic interactions at the interfaces between magnetostrictive CFO and electrostrictive

BTO. Later on, unusual strong vertical strain states was introduced in thick VAN films (up to um) with $BiFeO_3$: Sm_2O_3 (BFO: Sm_2O_3) and LSMO: ZnO nanocomposites [58], leading to a boost of extensive research interest in the VAN nanostructures [1, 2, 61, 62]. Table 1.2 summerized the demonstrated VAN systems with crystal structures and functionalities till now.

1.2.2 Growth and microstructure of VAN thin films

Figure 1.12 displays the typical microstructure of VAN thin films with the cross-sectional as well as plan-view TEM images. In VAN films, two immiscible materials co-growth epitaxially on the substrates form a pillar-in-matrix structures. The unique high-quality epitaxy and size-tunable VAN architectures offer great capability for cooperation of interface coupling effects through the vertical phase boundaries [61], [63].

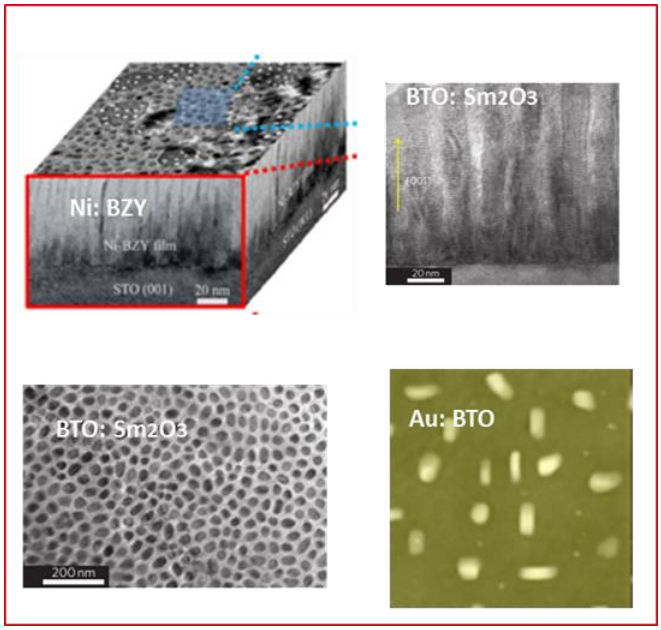

Figure 1. 12 Microstructures of VAN films a) overall 3D microstructure, b) cross-sectional and c) plan-view TEM images, d) STEM image [65, 66, 67].

Table 1. 2 Epitaxial VAN nanocomposite grouped by functionalities

Functionalities	VAN systems
Superconducting	$BaZrO_3$: $YBa_2Cu_3O_{7-d}$ (YBCO) $BaSnO_3$: YBCO; $BaHfO_3$: YBCO; Ba_2YTaO_6: YBCO; Ba_2YNbO_6: YBCO
Ferroelectric	$BaTiO_3$: Sm_2O_3; $BaTiO_3$: CeO_2; $BiFeO_3$: Sm_2O_3
Magnetic and magnetotransport	$La_{0.7}Sr_{0.3}MnO_3$ (LSMO): ZnO; LSMO: CeO_2; LSMO: Mn_3O_4; LSMO: NiO; $La_{1-x}Ca_xMnO_3$: MgO, $SrRuO_3$: $CoFe_2O_4$; Ni: $BaZr_{0.8}Y_{0.2}O_3$[57] Ni: CeO_2 Co: CeO_2
Multiferroic	$BiFeO_3$: $CoFe_2O_4$; $BaTiO_3$: $CoFe_2O_4$; $BiFeO_3$: $NiFe_2O_4$; La_2CoMnO_6: ZnO; $Bi_5Ti_3FeO_{15}$: $CoFe_2O_4$
Ionic transport	$SrTiO_3$: Sm_2O_3; $BiFeO_3$: $CoFe_2O_4$; $SrZrO_3$: RE_2O_3 (RE = rare-earth); $SrRuO_3$: ZnO
Dielectric and Optical	$Ba_{0.6}Sr_{0.4}TiO_3$-Sm_2O_3; $SrRuO_3$: $CoFe_2O_4$; $BiFeO_3$: Sm_2O_3; $SrRuO_3$-ZnO; Au-$BaTiO_3$
Exchange bias	LSMO: $BiFeO_3$; LSMO: $LaFeO_3$; LSMO: NiO

To design versatile VAN system with desired functionalities, a fundamental understanding of the growth mechanism is needed. Figure 1.13 illustrates a proposed simplified growth mechanism for a typical two phase VAN system based on diffusion and nucleation theory [62]. The process involves three stages, i.e, i) surface diffusion of the adatoms (clusters), ii) nucleation of the independent two phases, and the following iii) growth of the columnars all through the film thickness. Thus to grow a VAN architecture successfully, several key prerequisite conditions need to be met: 1) the two phases should have low solubility between each other, i.e, immiscible two phases with limit intermixing; 2) both phases should have similar growth kinetics and thermodynamic as well as chemical stability with the substrate and with each other.

Growth mechanism involving decomposition also occurs in certain systems, leading to unique VAN structures as well. Typical example is the Fe: $LaSrFeO_4$ films with single-crystalline alpha-Fe nanowires embedded in $LaSrFeO_4$ matrix resulted from the decomposition reaction $2La_{0.5}Sr_{0.5}FeO_3 \dashrightarrow LaSrFeO_4 + Fe + O_2$ during the deposition of $La_{0.5}Sr_{0.5}FeO_3$ under reducing conditions [64].

A large veriaties of structures including checkerboard, nanopillars and nanomaze structures with dimensions and shapes tunable have be obtained depending on the materials system and growth condition, making VAN films powerful in a wide range of functionalities.

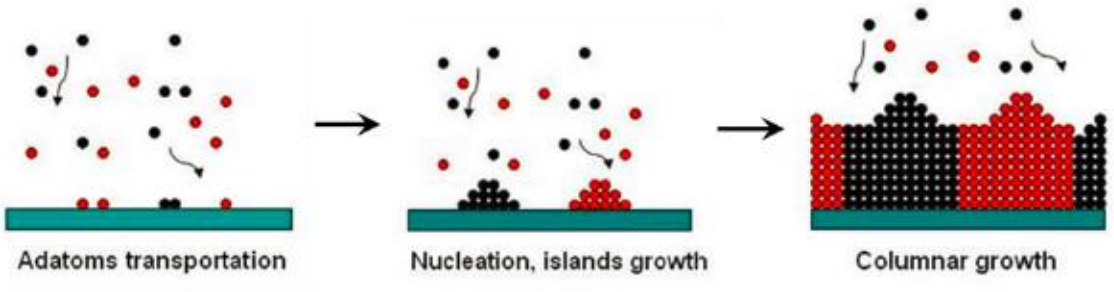

Figure 1. 13 Simplified growth mechanism for typical two phase VAN film [62].

1.2.3 Strain engineering in VAN thin films

In VAN architectures, high density of hetero-interfaces could introduce tunable strain and structural coupling effects, leading much enhanced properties. The overall lattice matching and strain imposition in the VAN systems is illustrated using ABO_3 perovskite as example (Fig.1.14) [61]. The substrate will give an epitaxy tensile strain to the film deposited on it with relative smaller lattice parameter (phase 1, a<c), and a compressive strain to the film with larger lattice parameter (phase 2, b>c). When two phases were grown coherently and immiscibly, the out-of-plane lattice could be coupled after the epitaxy strain relaxed, through the vertical interfaces [58]. Substrate induced epitaxial strain can supply disorder-free large biaxial strain (up to several percentage) [68], but the strain will be relaxed in thickness within tens of nanometers. While in VAN films, the high density of vertical interfaces can maintain the strain state all through the thick film. The tunability of the strain in the VAN films has been successfully exploited to achieve enhanced functionalities, such as elevating the ferroelectricity Curie temperature (Tc) in $BaTiO_3$: Sm_2O_3[69] $BaTiO_3$: CeO_2 [70] systems within micrometer thick films.

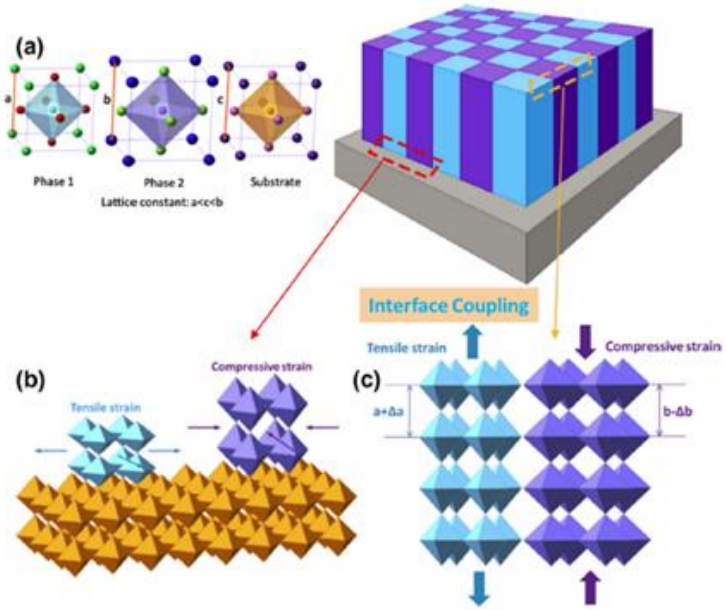

Figure 1. 14 Sketch of normal VAN structures, and mismatch strain illustration. a) unstrained unit cell of different phases and substrates, b) substrate induced epitaxy biaxial strain, c) vertical strain coupling through vertical hetero-interfaces [61].

1.2.4 Functionalities of VAN thin films

The atomic structure at the interface as well as defects in the vertical interfaces could also lead to interesting behavior in VAN systems. For example, direct electron energy loss spectroscopy shows that high concentration of mobile oxygen vacancies ($V_o^{"}$) were accumulated at the interface between $SrTiO_3$ and Sm_2O_3 in $SrTiO_3$: Sm_2O_3 composite thin films. The movement of $V_o^{"}$ toward or away from top Pt electrodes under electrical field can cause the films to behavior as a forming-free memristor devices [71]. In addition, robust local electronic conduction has also been observed at vertical interfaces of $BiFeO_3$: $CoFe_2O_4$ systems, distinguished with the insulating characteristics in both $BiFeO_3$ and $CoFe_2O_4$ phases [72]. Oxygen vacancies induced at the interfaces is believed to account for such behavior [72].

Besides the strain and structural coupling, the strong coupling between magnetic spin, electric charge and orbital through the heterointerfaces between the two phases in the VAN systems is also a powerful way to realize and understand novel functionalities. For example, multi-ferroicity has been proven in $BiFeO_3$: $CoFe_2O_4$ [73], $BaTiO_3$: $CoFe_2O_4$ [60] VAN films with interfacial magneto-electric coupling. Enhanced perpendicular magnetic anisotropy in $BiFeO_3$: $CoFe_2O_4$ VAN films has been observed from the interfacial antiferromagnetic/ferrimagnetic spin spin-flop coupling. Choosing ferromagnetic and antiferromagnetic materials as two phase, exchange bias effect was induced in $BiFeO_3$: $La_{0.7}Sr_{0.3}MnO_3$ VAN films by interfacial spin coupling [74]. The unique VAN structures is also benefit for enhanced magnetoresistance behavior with induced vertical tunneling junctions, demonstrated in LSMO: ZnO [75, 76], LCMO: MgO [26], LSMO: NiO [77, 78], LSMO: CeO_2 [79], etc.

1.3 Strain engineering in epitaxial oxide thin films

During the long history stream of material science, strain has been playing an important role for tuning materials' properties, triggering novel functionalities as well as obtaining insight of fundamental physics [68,61,80]. Great success have been achieved by strain engineering for improving transistors' mobility [81,82], engineering band structures [838485], enhancing properties of superconductors [86], ferroelectrics [67,87,88,89], and ferromagnetics [90,91], and even introducing new crystal structures [92] and inducing ferroic properties out of non-ferroic materials [93,94].

For the oxide thin film family, both epitaxy strain, that comes from the misfit with substrates and vertical strain in vertically aligned nanocomposite (VAN) systems, [58,76,62

have been investigated widely and demonstrated dramatic alternation of the properties, especially in recent years with the advancement of thin film growth technique and development of new substrates[24].

1.3.1 Strain engineered phase transition in ferroic oxides

Ferroelectronics, materials that exhibit field switchable stable and spontaneous electronic polarization, show wide application potential in sensors, actuators, memories, and transistors, thus form an important component of today's materials, attracting extensive interest. Most common ferroelectronics are ABO_3 perovskite oxides, like $PbTiO_3$, $BaTiO_3$, $BiFeO_3$, etc. [4, 95], with or without doping. During the development, strain engineering has been widely investigated and demonstrated critical influence on the phase structure and properties of ferroelectronics.

$BiFeO_3$ (BFO) is the most studied lead free ferroelectric materials due to its large polarization and coexisting of ferroelectricity and antiferromagnetic at room temperature[96]. High quality, free standing rhombohedral BFO single crystal can have a remanent polarization of ~100 $\mu C/cm^2$ [97, 98]. Its unique ferroelectricity is believed to be driven by lone-pair electrons of the Bi ion. For its thin film counterpart, different strain confinement can give various structure and properties. Under moderate compressive or tensile strain, BFO shows distorted rhombohedral structure, and have polarization direction along [111] with polarization of ~100 $\mu C/cm^2$, similar with its bulk, while compressive strain rotates the [111] polarization toward out-of-plane, making the [001] polarization larger, and tensile strain rotates the polarization to in-plane, giving smaller out-of-plane polarization [99100], shown in Figure 1.15a, b. However, BFO can show a unique tetragonal structure (T

phase) with a large c/a ratio of ~1.25 when grown on substrates that can give compressive epitaxial strain exceeds ~-4%[101], such as $LaAlO_3$ (LAO), $YAlO_3$ (YAO). This new T phase is predicted and experimentally determined to have a giant polarization of ~150 $\mu C/cm^2$, higher than any other perovskite. What's more, partially relaxed highly strained BFO films show coexistence of multiple polymorphs, and remarkable stripe-like domain patterns [96], making it promising for probe-based data storage and actuator applications. Recent work also shows that the highly strained BFO films, 45 nm BFO on LAO, can undergo a transition to a true tetragonal high-temperature state at 430 ℃, with an estimated Curie temperature above 800℃. While S' polymorph is needed for piezoelectric switching, restricting the switching temperature no higher than 300 ℃.

Strain effect has also been utilized to enhance the Curie temperature of ferroelectric materials. Phase field simulation shows that both tensile and compressive strain can elevate $BaTiO_3$'s Curie temperature (T_c). Figure 1.16a shows strain-temperature phase diagram of epitaxial $BaTiO_3$ thin film. With increasing in-plane strain, T_c of $BaTiO_3$ thin films increased, achieving ~540 ℃ on $DyScO_3$ substrate compared with 130 ℃ of bulk. However, the magnitude of strain that can be applied is limited by available substrates and strain relaxation. Recent work demonstrated that epitaxial strain can control process induced defect dipoles' ordering, inducing additional vertical strains and enhancing T_c without need to change substrates. Figure 1.16b gives temperature-dependence of out-of plane c lattice parameters of $BaTiO_3$ films grown at different laser fluences. There are two regimes of thermal expansion separated by a kink which indicates

a phase transition. $BaTiO_3$ films grown by combining PLD growth process and $GdScO_3$ (110) substrate strain shows Tc over 800 ℃ according to this work.

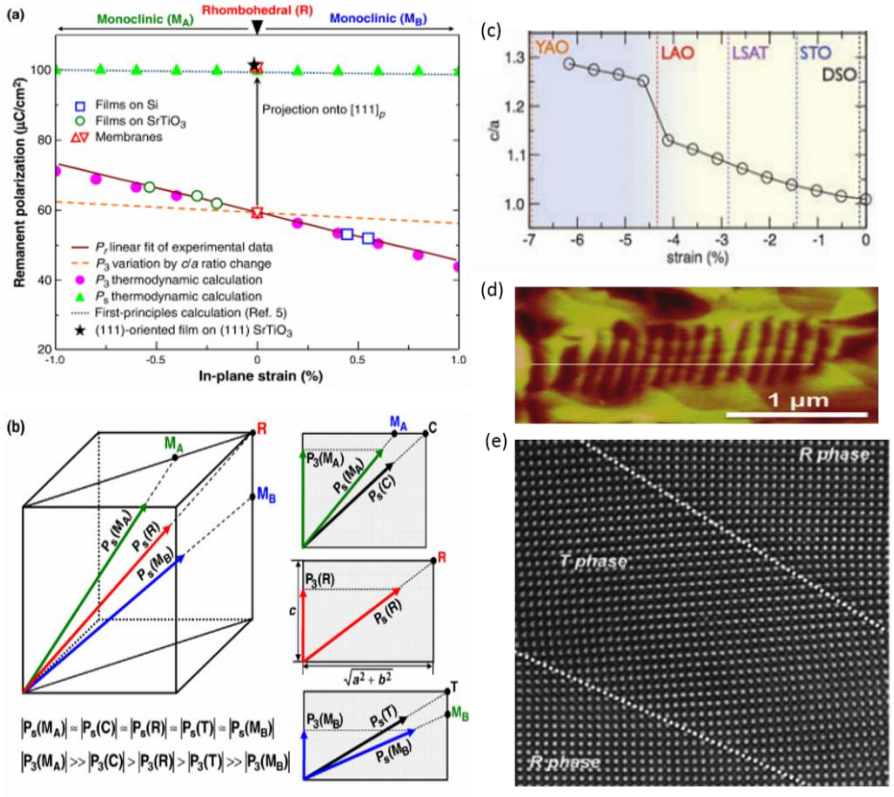

Figure 1. 15 a), b) Diagram showing moderate strain induced polarization rotation. a) Remanent polarization vs in-plane strain for $BiFeO_3$ films; b) the spontaneous polarization direction of the rhombohedral (R) and monoclinic (MA and MB) phases of $BiFeO_3$ [102]. c) Ab initio calculations of structure (c/a ratio) as a function of epitaxial strain of BFO films; d) Atomic force microscopy image of a partially relaxed BFO film grown on LAO substrate, showing strip like domain structure; e) High resolution TEM image of the mixed T and R phase BFO on LAO substrate [87].

Apart from epitaxial strain, vertical strain induced through nanocomposite gives possibility to enhance ferroelectricities of much thicker films. Shown in Figure 1.16c, d, micrometer-thick self-assembled $BaTiO_3$:Sm_2O_3 nanocomposite has demonstrated $BaTiO_3$ tetragonal-to-cubic structural transition temperature beyond 800 ℃, while remnant polarization persisted till 330 ℃. The interspersing grown Sm_2O_3 columns induced tensile strain for $BaTiO_3$ matrix by 2.35%, which helps $BaTiO_3$ to maintain its tetragonal structures, thus dramatically enhanced T_c.

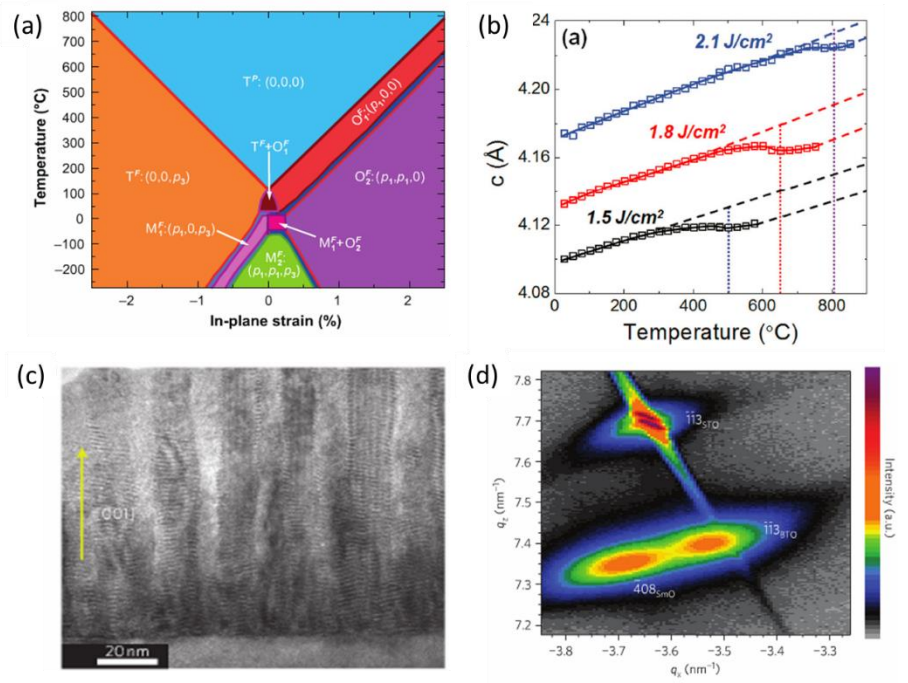

Figure 1. 16 a) Phase diagram of $BaTiO_3$ films as a function of temperature and substrate in-plane strain [103]; b) temperature dependent c lattice parameter of $BaTiO_3$ thin films grown with different laser fluences [104]. c) TEM image of vertical aligned $BaTiO_3$/Sm_2O_3 nanocomposite film and d) X-ray reciprocal space maps of the STO substrate for $BaTiO_3$/Sm_2O_3 nanocomposite, showing dramatically change of $BaTiO_3$ lattice constant by Sm_2O_3 induced strain [67].

By critical control, strain can also induce ferroic properties out of conventional non-ferroic material. As shown in Figure 1.17a, biaxial stain can tune $SrTiO_3$ to perform ferroelectricity and shift the Tc to room temperature [105], which has been demonstrated experimentally with development of thin film growth technique and invention of substrates with different lattice constant. What's more, magnetically ordered insulators $EuTiO_3$ that are neither ferroelectric nor ferromagnetic can be transformed into ferroelectric ferromagnets under proper strain, diagram shown in Fig. 4b, and experimental measurement confirmed that $EuTiO_3$ grown on (110) $DyScO_3$ substrate shows strong ferroelectric and ferromagnetic properties.

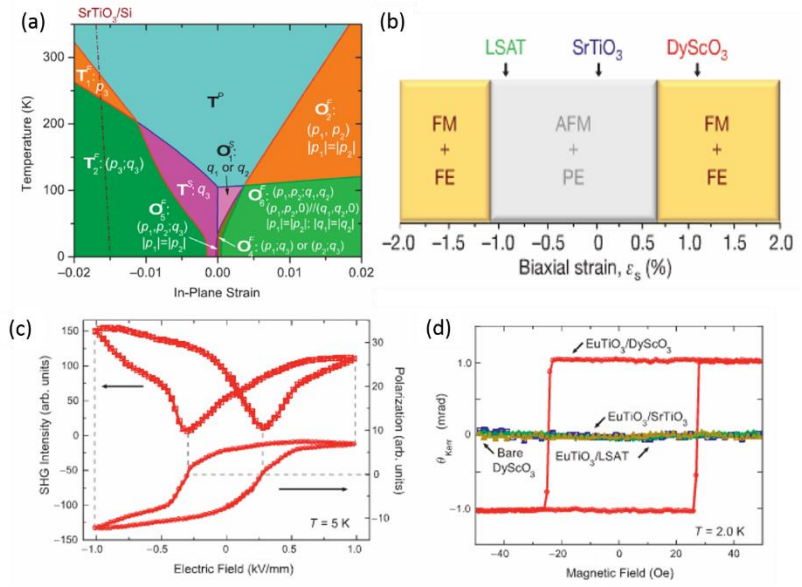

Figure 1. 17 a) Strain-temperature phase diagram of (001) $SrTiO_3$ [105]; b) First-principles epitaxial phase diagram of $EuTiO_3$ strained from 22% (biaxial compression) to 12% (biaxial tension, showing different ferroic properties with different strain state; c) SHG hysteresis loop (top) and corresponding polarization loop (bottom) for $EuTiO_3$ on $DyScO_3$ at 5 K. d) MOKE measurements at 2.0 K of $EuTiO_3$ on different substrates [93].

1.3.2 Strain controlled magnetic and mangetotransport

Metallic ferromagnetic materials have received much interest due to the technically importance in the emerging spintronics field. Among them, mangantites with chemical formula of $A_{1-x}B_xMnO_3$, in which A-cations usually are La, Pr, and Nd and B-cation Sr, Ca, Ba, is specially an important family of compounds. The colossal magnetoresistance (CMR) induced properly by "double-exchange" mechanism in mangantites draw them intensive research [106].

$La_{0.7}Sr_{0.3}MnO_3$ has maximum T_c of 360 K and is half-metal with high spin polarization, important for device applications. The magnetic and transport properties of LSMO thin films varies dramatically with strain. From both experimental, and first principle band structure calculations [107], phase diagram of LSMO shows that its c/a ratio which is determined largely by strain have significant influence on its orbital organization. The LSMO film transits from FM/metal state without strain to a C-AFM/insulator state at large compressive strain, while to an A-AFM/metal state under large tensile strain due to the Jahn-Teller distortions of the MnO_6 octahedra [108], shown as Figure 1.18. Figure 1.19 shows transport properties and Curie temperature of LSMO thin film grown on $LaAlO_3$, LSAT, $NdGaO_3$, $SrTiO_3$, $DyScO_3$, $GdScO_3$ etc. single crystal substrates, which can offer biaxial strain from -2.3% to +3.2% [91]. Both compressive and tensile strain can make the Tc of LSMO decreased, while large compressive strain (that on $LaAlO_3$) make it insulating, which consist well with previous prediction. Recently, an abnormal in-plane transport anisotropy is observed in large tensile strained LSMO film [109]. For A-AFM phase LSMO on $DyScO_3$, resistivity is lower along the longer a direction with anisotropy (ρ_b-

$\rho_a)/\rho_a$ of ~30% at low temperature, shown in Figure 1.20. While films grown on STO, NGO and LAO show negligible in-plane resistivity anisotropy. XAS study and first principle calculations suggest it to be triggered by preferred occupancy of the O $2p_x$ orbitals.

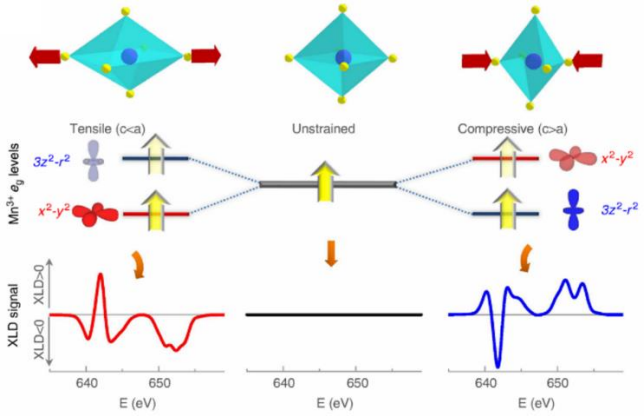

Figure 1. 18 Preferential orbital occupancy and linear dichroism. [108] Top: MnO_6 octahedral distortions as a function of strain; middle: subsequent effect of the JT distortion on the e_g levels of Mn^{3+} ions; bottom: X-ray linear dichroism simulated for the Mn L-edge of Mn^{3+} ion in a tetragonal crystal field with c<a (left), with c>a (right) and with octahedral field (center).

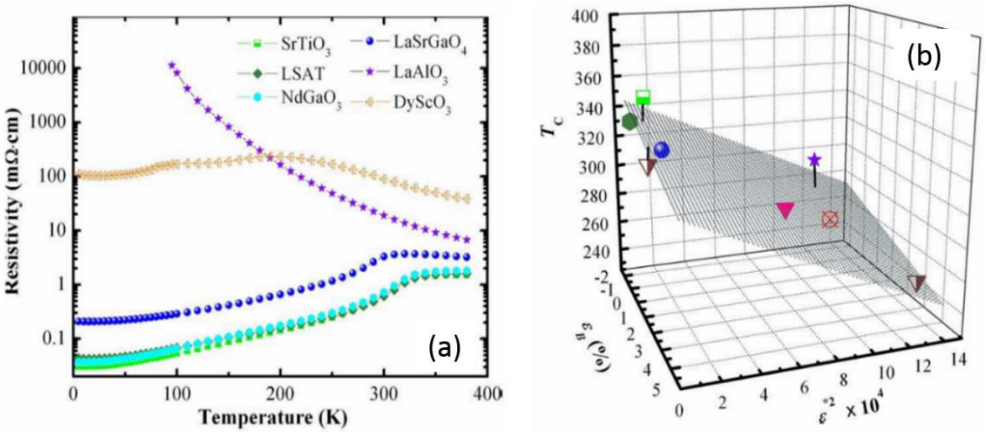

Figure 1. 19 a) resistivity vs temperature behavior of $La_{0.7}Sr_{0.3}MnO_3$ on different substrates. b) Curie temperature vs strains [91].

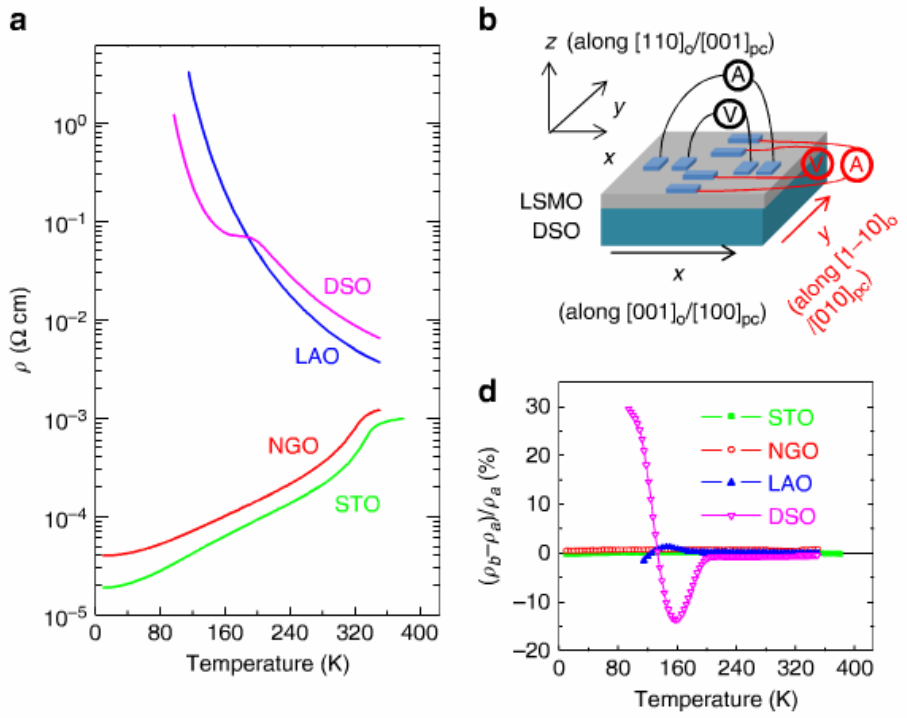

Figure 1. 20 In-plane resistivity anisotropy of LSMO on DSO substrate [109]. (a) Temperature dependence of resistivity of 8 nm LSMO thin films on different substrates under zero magnetic field. (b) Schematic illustration of the experimental set-up; (d) The in-plane resistivity anisotropy of 8 nm LSMO thin films on different substrates. Only the film on DSO under large tensile strain shows pronounced resistivity anisotropy.

Not only strain can tune mangantites' intrinsic properties, it can also induce new functionality. Since compressive or tensile strain favours LSMO C-AFM ($3z^2$-r^2) or A-AFM (x^2-y^2) ordering, respectively. Using the strain engineering, unexpected exchange bias (EB) effect was reported in a LSMO "single" film on (001) $LaSrAlO_4$ (LSAO) substrate recently [110]. It is demonstrated that the large compressive substrate strain has led to a reconstruction of structure and composition to form a $LaSrMnO_4$ AFM layer (Figure 1.21), inducing significant EB effect when contacted with the upper self-assembled FM

LSMO film. Same phenomenon has been found on fully strained $La_{2/3}Ca_{1/3}MnO_3$ films [111].

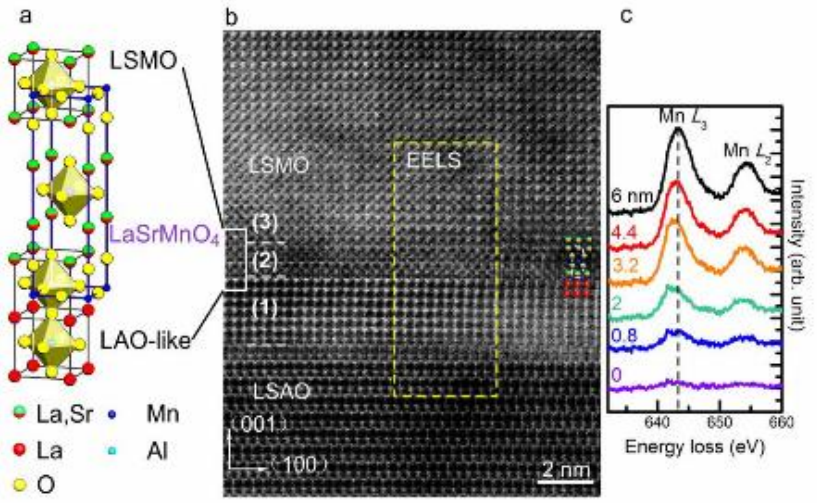

Figure 1. 21 Direct observation of self-assembled structures in LSMO films [110].

Epitaxial strain cannot be maintained till large film thickness, above a critical layer thickness, strain will be relaxed by misfit dislocations. Usually critical layer thickness is on order of a few nanometers. Given this, self-assemble vertically aligned nanocomposite (VAN) thin films which can induce large vertical strain in much thicker films, emerges as a promising strategy for practical applications [58]. LSMO:ZnO heteroepitaxial film have been investigated. The vertical mismatch between LSMO and ZnO can induce an out-of-plane dominant strain and offer significant ability in tuning its magneto-transport properties. Other VAN systems including $BaTiO_3$:Sm_2O_3, $BiFeO_3$:Sm_2O_3, LSMO:CeO_2, LSMO:MgO, $BiFeO_3$:$CoFe_2O_4$ and $BaZrO_3$:$YBa_2Cu_3O_7$-x have been developed during recent years, tuning properties for ferroelectronics, ferromagnetics, multiferroics, as well as superconducting materials, which have been discussed above.

1.4 Spatial ordering of VAN films

1.4.1 Literature review of ordered VAN growth

Nanostructures with ordering control is important for integration of the fascinating materials into devices for practical usage. Meanwhile, ordered nanostructures might also trigger new phenomenon that disordered structures cannot obtain. With the pioneering work in the field mostly focused on broadening possible materials systems and triggering novel properties [21], another timely demand for implementing VAN in future nanoscale devices is to achieve spatial ordering [1,112]. However most of the as-grown VAN films demonstrated up-to-date present very limited short range ordering and no long range ordering [1].

Since such in-plane ordering of the pillars could dramatically enrich the practical applications for the VAN films, several lithography and seeding techniques have been explored in achieving directed ordered growth, while with limited success [112,113,114,115,116,117].

Most of the demonstrations are on a specific system, i.e., $CoFe_2O_4$ (CFO)/$BiFeO_3$ (BFO). In 2012, Ryan Comes, etl, fabricated CFO seeds from CFO thin film using electron beam lithography (EBL) and ion milling. Patterned CFO pillars was first demonstrated on such seed locations [114]. The schematic flowchart is shown in Figure 1.22. The process involves the following steps: 1) Deposition of CFO film using pulsed electron deposition (PED). 2) Deposition of amorphous Si capping layer using RF sputtering, 3) Spin coating of sample with HSQ negative-tone e-beam resist, 4) Patterning of pillars using EBL, 5) Reactive ion etching of Si cap, 6) Ar ion etching of CFO film. 7) Deposition of 1 nm thick

BFO film using PED, followed by 8) Co-deposition of CFO and BFO using PED to form an epitaxial nanocomposite. Arrays of CFO nanopillars with period of 100, 150, and 200 nm were fabricated within 20-30 nm film thickness.

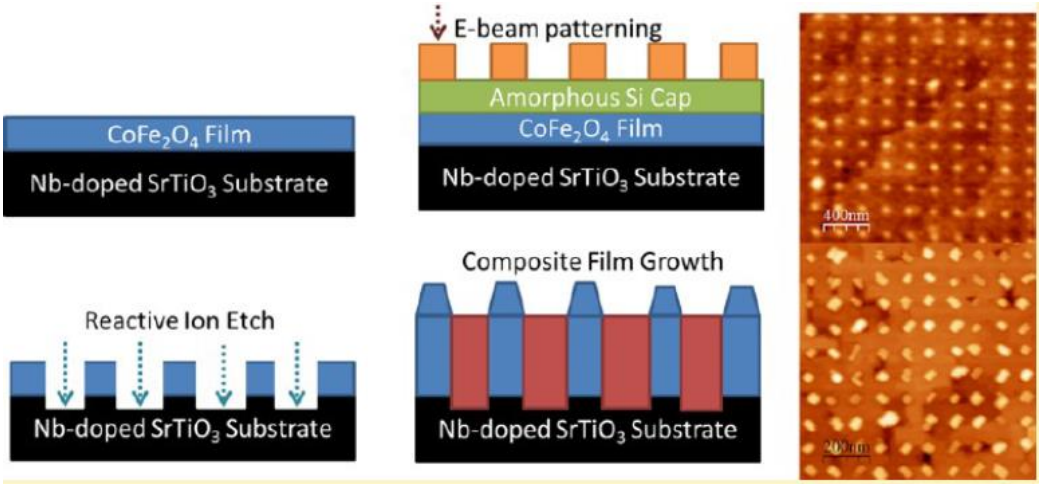

Figure 1. 22 Flowchart for the fabrication of ordered CFO in BFO matrix structure using EBL, etching and seeding process [114]. a) Deposition of CFO film using PED. b) Deposition of amorphous Si capping layer using RF sputtering, Spin coating of sample with HSQ negative-tone e-beam resist, and patterning of pillars using EBL. c) Reactive ion etching of Si cap and Ar ion etching of CFO film. d) Deposition of 1 nm thick BFO film using PED, followed by codeposition of CFO and BFO using PED to form an epitaxial nanocomposite.

Another approach is to use hard masks of EBL-patterned gold or anodic aluminum oxide (AAO) together with lift-off process enabled CFO nuclei to guide the pillar growth [115]. The procedure is shown in Figure 1.23. CFO seeds were directly grown on the substrate through a hard mask of AAO. Results shown that BFO: CFO nanocomposites grown on such seeds patterns mimic the initial seeds pattern and form ordered CFO arrays in BFO matrix structure. Hexagonal and square arrays of 200-300 nm period CFO islands were obtained in 50-60 thick BFO: CFO films.

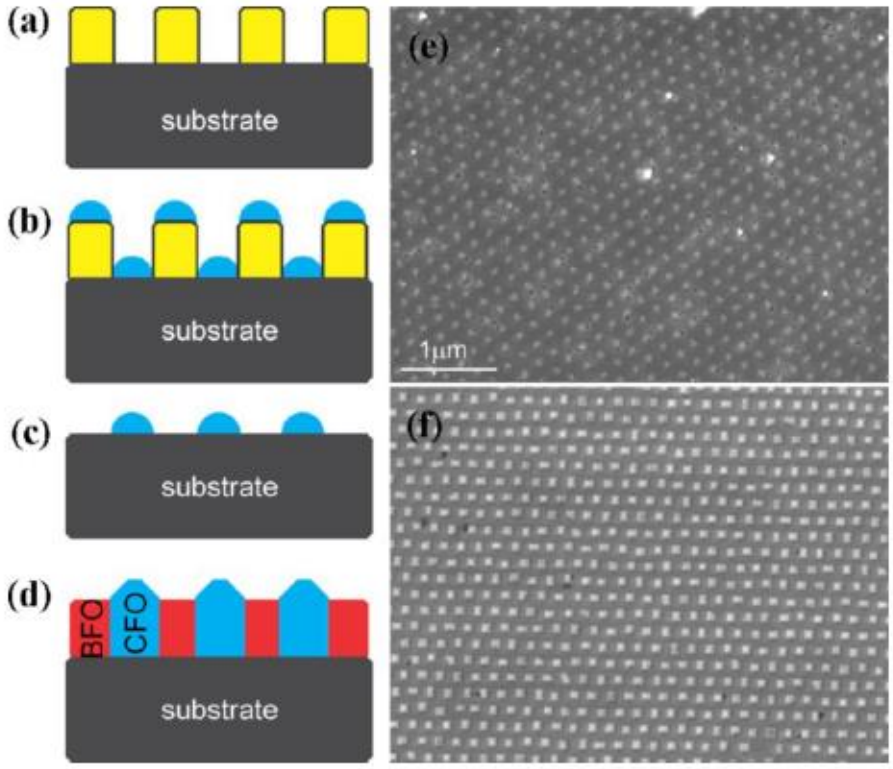

Figure 1. 23 Steps of the nucleation-induced process [115]: a) mask transfer on the substrate, b) deposition of CFO through the mask, c) formation of nucleation centers by removal of the hard mask, d) growth of the ordered nanocomposite by deposition from a mixed target. SEM images of CFO nucleation centers with hexagonal symmetry (e) and final resulted composite obtained.

Recently etch pits fabricated by focused ion beam (FIB) [112] and etched with mask of triblock terpolymer film [113] were used to seed the CFO growth, shown in Figure 1.24. benefited from the difference in surface energy between CFO and the substrates. The driving force for the selective nucleation of the CFO is the high energy of the {100}-oriented interface between the spinel and perovskite phases, [118] which is revealed by the poor wettability of CFO on (001) STO [119] and which induces the formation of discrete pillars. By forming inside substrate pits, which exhibit surfaces other than {100}, the spinel nuclei minimize their total surface energy. After annealing the patterned substrates

at 950 °C for 30 minutes, which induced (001) faceting of the pits, little or no spinel nucleation at the base of the pits were observed.

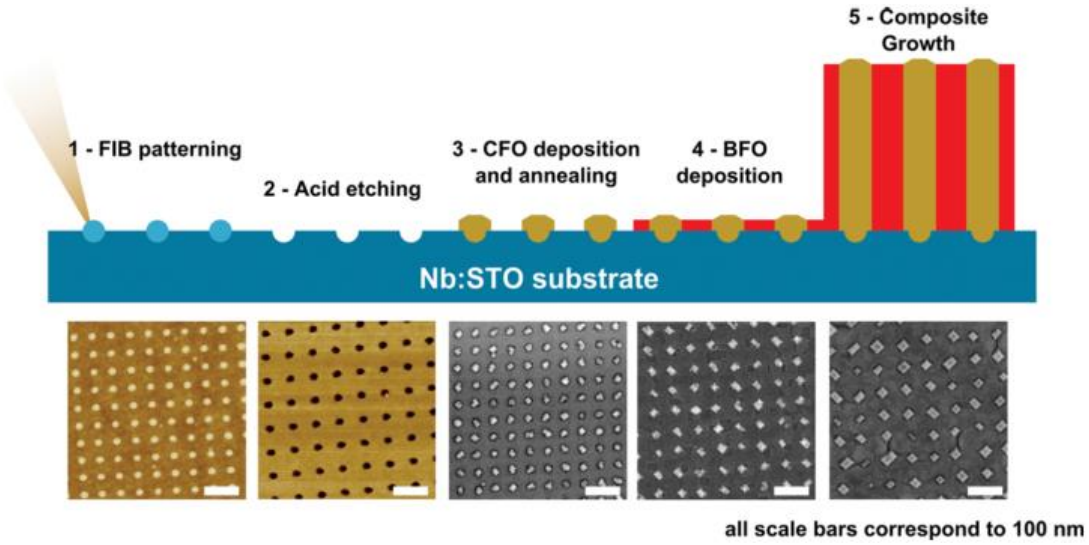

Figure 1. 24 Schematic of the templating process for vertical nanocomposites of CFO spinel pillars in a BFO perovskite matrix [112]. The lower images show example morphologies. From left to right: AFM of Nb:STO substrate after FIB, 60 nm period; AFM after etching, 80 nm period; SEM of CFO in pits, 60 nm period; SEM after BFO deposition, 75 nm period; and SEM after growth of the composite, 80 nm period.

Similar seeding method has also been utilized in controlled growth of $Fe/LaSrFeO_4$ and $(Fe, Zn)_3O_4/BiFeO_3$ nano-dots arrays with nanoimprint lithography (NIL) [116,117]. As we can see, although these approaches achieved well-ordered structures, they all involve sophisticated seeding procedure employing EBL, FIB, NIL or complex etching/lift-off process, the ordered areas are limited and the scale-up could be challenging.

1.4.2 Tailored substrate surface for templating nanostructures growth

With the advantage of the progress of single crystal substrates fabrication and substrate treatment techniques, oxide thin films has been demonstrated for varieties of novel functionalities. Both the substrate lattice structure and the surface are important for epitaxial thin film growth. As discussed before, substrate mismatch triggered epitaxial strain is powerful to tune the functionalities of oxide thin films. Lots of work have shown that tailoring the substrate surface could also stimulate novel structure and functionalities.

$SrTiO_3$ (STO) is the most popular substrate due to its good lattice match with most interesting perovskite oxides. STO has a lattice parameter of 3.905 Å. In the [001] direction, it has stacking SrO and TiO_2 atomic planes, shown in Figure 1.25 [120]. For as-fabricated polished STO (001) single crystalline substrates, At the surface, both SrO and TiO_2 terminations exist, with SrO termination being the minority, i.e, SrO takes about 5–25% of the total surface area. As substrate surface structure as well as energy plays an important role in the thin film growth, the STO (001) surface has been widely investigated. Reconstructions, nanostructures, cationic off-stoichiometry and precipitates at the surface have been observed depending on the chemical and/or thermal treatments. The large variety of reported results signals the strong sensitivity of STO (001) surfaces on the processing conditions, including interaction with chemicals, annealing (gas, temperature, time and rate) and the microstructure (defects, dopants, impurities, Sr off stoichiometry) of the single crystal. Varieties of process have been demonstrated to get single terminated STO substrate, either TiO_2 termination or SrO termination. Reports have shown that the substrate termination can impact a lot on the grown oxide thin films. For example,

controlled ordering of domains in $BiFeO_3$ film is presented[121], as well as a controlled selectivity between two types of domain walls is presented, i.e., 71° and 109°, by modifying the substrate termination, shown in Figure 1.26. Electrical properties also differ a lot for FTJs on A-site and B-site terminated substrate.

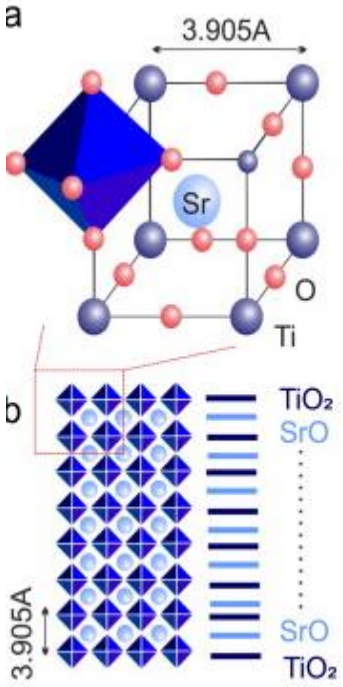

Figure 1. 25 Crystal structure (a) and stacking atomic planes (b) of STO (001) substrate [120].

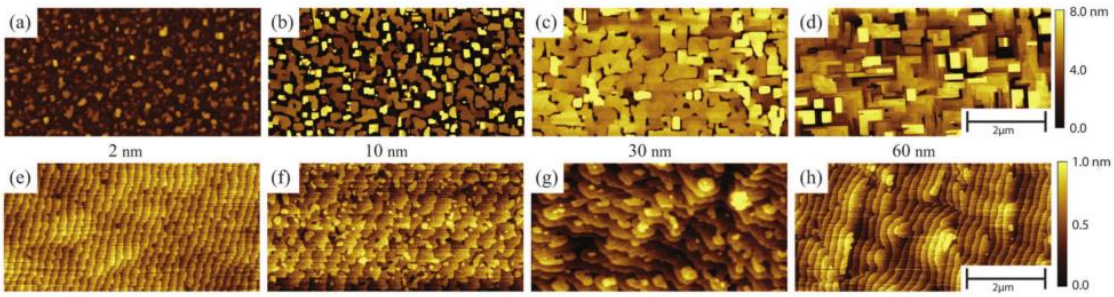

Figure 1. 26 Topography evolution of BFO thin films with thickness from 2 to 60nm on a-d) TiO_2-terminated and e-h) SrO-terminated STO (001) substrates [121].

Considering that the surface termination have important influence on thin films growth, recently, templated nanostructures has been demonstrated on substrates with nano-patterns of different termination. The small lateral sizes of SrO regions imply long step edges separating TiO_2 and SrO terminated regions and thus coalescence of the minority SrO terminated regions could occur at high temperature to reduce the overall surface energy. The final result would be a surface with well-ordered separated SrO and TiO_2 regions. This is observed after annealing at 1000°C, a temperature below the onset of massive diffusion of Sr from the bulk. Self-organized surface strips with alternating SrO and TiO_2 chemical terminations can be induced, with the lateral period adjustable by the substrate miscut angle [122, 123].

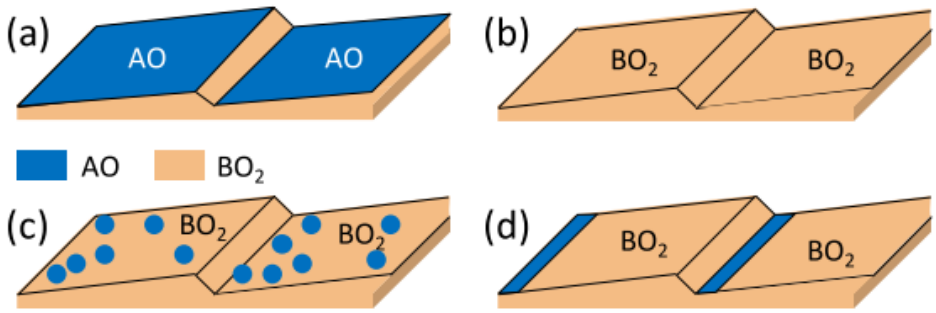

Figure 1. 27 Sketch of a (001)-oriented perovoskite surface exhibiting single chemical termination: AO(a) and BO_2 (b). Idem for surfaces in which BO2 and AO (majority and minority terminations, respectively) are randomly distributed (c) or confined along the steps (d). [123]

Similar results have also been observed on other most used substrates: (001)-oriented $La_{0.18}Sr_{0.82}Al_{0.59}Ta_{0.41}O_3$ (LSAT), $LaAlO_3$ (LAO), and $DyScO_3$ (DSO). All present ABO_3 perovskite-like crystal structures with alternating AO and BO_2 charged

planes along [001] and lattice parameters of 3.87 Å, 3.79 Å, and 3.94 Å, (pseudo cubic lattice parameter) respectively. Single termination as well as surface with both termination have been derived by annealing process in a wide range of conditions of time and temperature. A striped pattern of AO and BO2 terminations are reported for annealed LSAT (001) and DSO, similar with that of STO (001).

Such nano-patterned substrate with alternating termination has been demonstrated to be able to derive selective growth of oxide materials. It is reported that $SrRuO_3$ growth on single terminated STO (001) substrate undergoes a transition from 3D to 2D growth with thickness. At first, a fingerlike structure originated by three-dimensional ~3D islands that nucleated along the substrate steps can be observed. Afterward, adatoms stick preferentially in the valleys of the structure and the films become progressively smoother. At a thickness above 10–20 nm, the films are extremely flat and have a self-organized structure of terraces and steps, with the growth proceeding mainly by a step flow ~two-dimensional mechanism. [124]. And a termination transition were observed for SRO grown on STO [125] with thickness, indicating better wettability of SRO on TiO_2 terminated surface. Taking advantage of the distinguished growth of SRO on the two terminations, SRO nanoribbon that mimic the substrate termination striped nanopatterns were successfully demonstrated, with the thickness up to 15nm [126]. It is shown that SRO were selectively grown on TiO_2 terminated area, leaving trenches in the SrO terminated region, forming well-ordered nanoribbons, displayed in Figure 1.28.

The templated STO (001) substrate with self-patterened chemical termination have also been used to engineer interface atomic composition in $LaAlO_3/SrTiO_3$

heterostructures. Well confined 2D electron gas laterally in the order of ~100nm are observed, leading to interesting resistivity anisotropy behavior [127]. Figure 1.29 shows the SEM image and AFM phase image of a 6 u.c. thick LAO film grown on a nanotemplated STO (001) substrate with alternating chemical terminations.

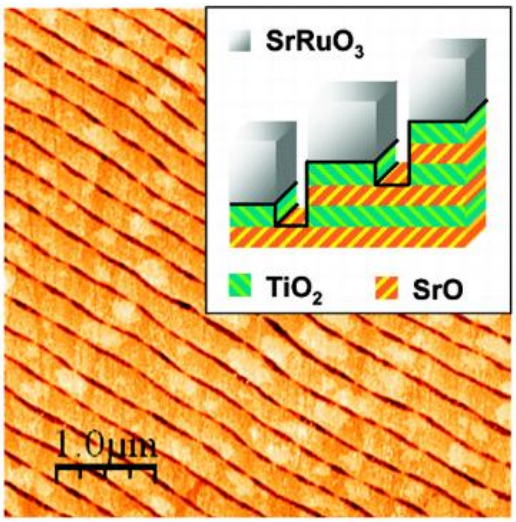

Figure 1. 28 Well-ordered $SrRuO_3$ nanostructures grown on templated STO (001) substrate with alternating SrO and TiO_2 terminated strips. $SrRuO_3$ was selectively grown on areas with TiO_2 termination. [126]

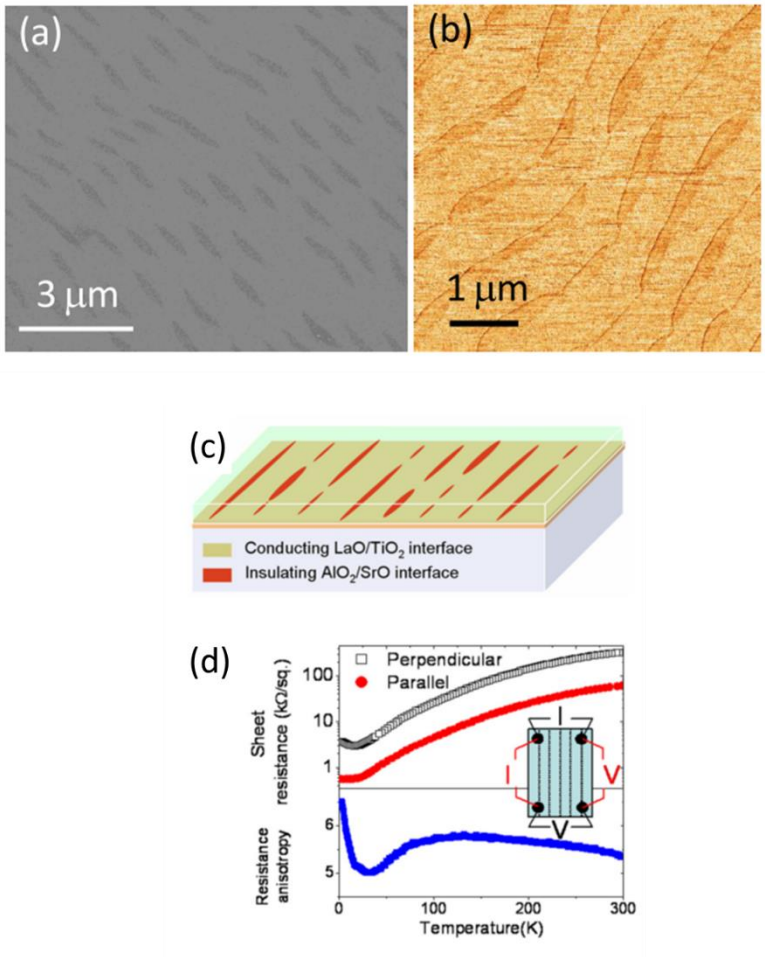

Figure 1. 29 Engineered ordered interface atomic composition in LaAlO3/STO heterostructures. a) SEM and b) AFM phase image of 6 u.c. thick LAO film on nanotemplated STO (001) substrate. c) Diagram of the distribution of interface 2D electron gas. d) Resulted resistivity anisotropy behavior. [127]

1.5 Research challenges and motivation

As discussed above, vertically aligned nanocomposite thin films have been emerging as powerful platform for materials engineering to explore novel functionalities, benefitted from its size tunable structures with high density of vertical heterointerfaces and high epitaxial quality. $La_{1-x}Sr_xMnO_3$ based materials is important for a wide range of applications, including magnetic memories, sensors, as well as in other all oxide solid state

devices, like ferroelectric tunneling juncitions, negative capacitors. At the same time, the LSMO family materials are also important for fundamental research in the area of condensed matter physics, especially spin-charge-structure couplings effect. In this dissertation, we have explored the LSMO based nanocomposite thin films using the powerful VAN design, to investigate the tunability of magnetic and transport properties as well as novel functionalities, including LFMR and perpendicular exchange bias. In addition, as spatial ordering is important for integration of fascinating VAN films into nanoscale devices, we also explored the capability of self-organized growth for VAN films with long range ordering utilizing substrate nano-templating techniques.

CHAPTER II

RESEARCH METHODOLOGY

2.1 Pulsed laser deposition

Pulsed Laser Deposition (PLD) is a versatile Physical vapor deposition (PVD) technique and has been used to deposit high quality films of a wide range of materials. In principle PLD uses pulses of laser energy to remove material from the surface of a target and get the film deposited on the substrate. Shown in Figure 2.1 is a setup diagram of PLD system. Generally it consists of a high energy laser source, a target (or several targets) and substrate with a distance of ~3-7 cm in a high vacuum chamber. During the deposition, high power laser pulses (with wavelengths of 157 nm, 193 nm, 248 nm, 308 nm and 351 nm) are used as energy source to melt, evaporate and ionize material from the surface of the target. A transient, highly luminous plasma plume expanding rapidly away from the target surface can be produced by the laser ablation. The ablated material is then collected on an appropriately placed substrate upon which it condenses and the thin film grows. In our experiment, KrF laser with wavelength of 248 nm is used. Before the deposition, the vacuum chamber is pumped to below $1*10^{-6}$ mbar. Laser frequency, energy, substrate temperature, oxygen pressure can be adjusted for optimize the film growth. A target-substrate distance of 5 cm is kept for all the films deposited.

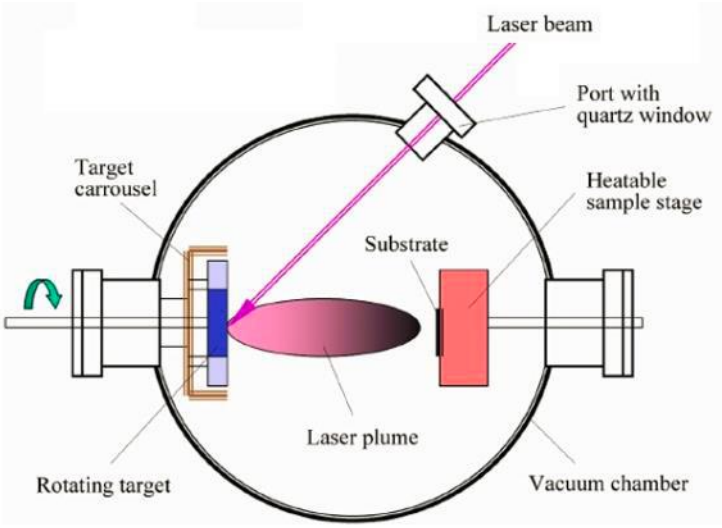

Figure 2. 1 Schematic experiment set-up for a pulse laser deposition system

PLD has significant advantages over other film deposition methods, beneficial for a wide range of materials growth. 1. With PLD, the chemical stoichiometry can be maintained from the target to substrate, which is beneficial for complex composition films growth. For example, exact chemical composition of a complex material such as YBCO, can be reproduced in the deposited film. 2. In PLD, high deposition rates can be achieved at moderate laser fluences, typically ~100s Å/min. The film thickness is easily controlled by the number of the laser pulses. 3. As laser is used as an external energy source, PLD offer an extremely clean process without filaments. Thus deposition can occur in both inert and reactive background gases, and in a wide range of gas pressure. 4. The use of a carousel, housing a number of target materials, enables multilayer films to be deposited without the need to break vacuum when changing between materials.

In spite of the advantages, industrial usage of PLD has been slow. Several reasons hinter its application in industry, including: 1. The plasma plume created during the laser

ablation process is highly forward directed, therefore the area of deposited material is quite small, (~1cm^2), compared to that required for industrial applications (~7.5 x 7.5 cm^2). In addition, the thickness of the films on the substrate could vary across the film, growth of uniform film is difficult. 2. Macroscopic globules of molten material, up to ~10μm diameter, exist in the ablated material, and such particulates arrived to substrate could impact a lot on the properties of the films deposited. 3. The fundamental processes, occurring within the laser-produced plasmas, are not fully understood; thus deposition of novel materials usually involves a period of empirical optimization of deposition parameters. In respect of the drawbacks of the nowadays PLD technique, it has been widely used in research environment, and wide range of novel functional materials have been developed using this powerful tool.

2.2 Structural characterization

2.2.1 X-ray diffraction

X-ray diffraction (XRD) is a non-destructive analytical technique that is used to identify the structure and chemical composition of crystalline materials. It can also be used to determine the crystal orientation, crystallite size, and stress in single crystal, powder, and thin film specimens. The technique is based on observing the scattered intensity of an X-ray beam hitting a sample as a function of incident and scattered angle, polarization, and wavelength or energy. Diffraction occurs when the wavelength of an incident beam is in the same order of the repeated distance in a crystal, as shown in Figure 2.2. The diffraction obeys Bragg's law：

$$n\lambda = 2d\sin\theta$$

where n is an integral, λ is the wavelength of the incident X-ray, d is the crystal lattice spacing and Θ is the diffraction angle.

At specific incident angle Θ and configuration of sample (rotation), the Bragg diffraction is satisfied for certain crystallographic plane, diffracted beam can be detected at the detector end. Otherwise the incident beam will be all scattered and no signal can be observed. For lattice constant and crystallization can be calculated with the peak position, and full width at half maximum.

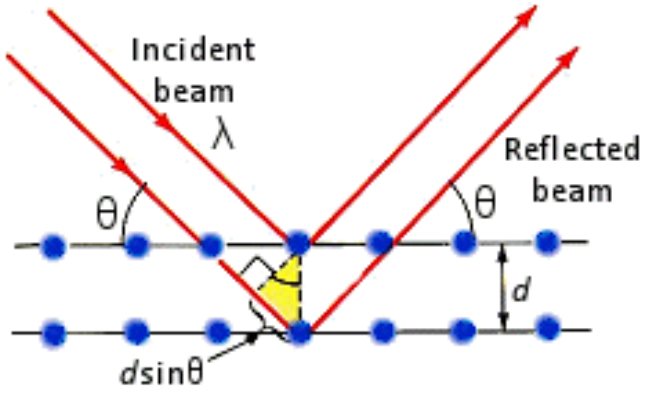

Figure 2. 2 Bragg diffraction for a set of crystal planes with interplanar spacing d.

2.2.2 Transmission electron microscopy

Transmission electron microscopy (TEM) is a powerful technique for characterization of materials with the information of morphology and crystallography. A beam of electrons is transmitted through an ultra-thin specimen, interacting with the specimen as it passes through it. An image is formed from the interaction of the electrons transmitted through the specimen. The transmission electron microscope (TEM) operates

on the same basic principles as the light microscope while uses electrons instead of visible light as illuminating species. For conventional optical microscopy, the resolution is limited by the minimum visible wavelength. In TEM, benefitted from the short wavelength of electrons generated, as equation below, far improved resolution can be achieved.

$$\lambda = \frac{1.22}{\sqrt{V}}$$

For an accelerating voltage of 200KV, a wavelength of 0.0027nm can be obtained.

Figure 2.3 shows two basic operation modes of TEM: the diffraction mode and the imaging mode. The switch between two different modes is conducted by changing the focal length to first image plane (imaging mode) or the back focal plane (diffraction mode) of the objective lens. Up to today, incorporated techniques have been developed in the TEM system, including high-angle annular dark field (HAADF) scanning transmission electron microscope (STEM), EDX and electron energy loss spectroscopy (EELS), giving more information of the chemical distribution.

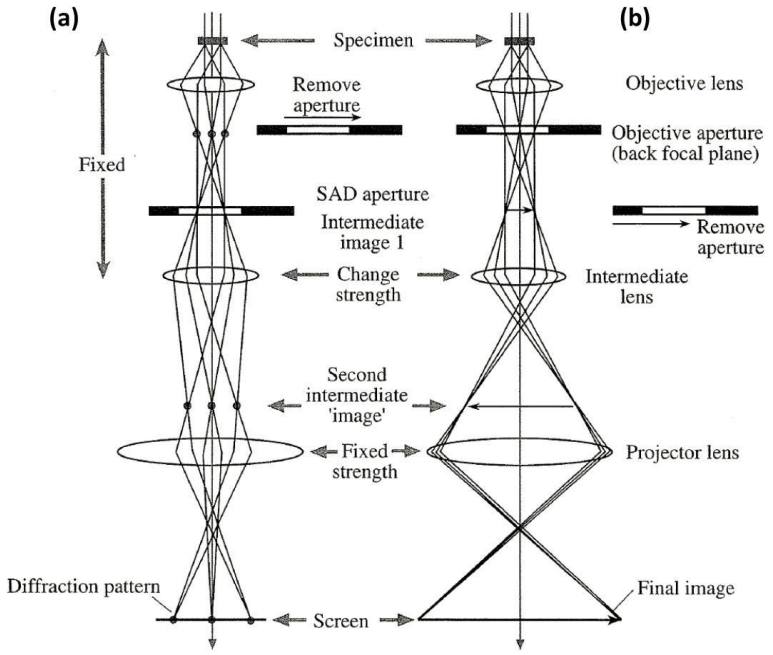

Figure 2. 3 The two basic modes of operation in a TEM: (a) diffraction and (b) imaging.

TEM sample preparation is important for reliable and high-effective TEM imaging. The main challenge of this work is obtain a sufficiently thin region with the thickness less than 100 nm in order to become electron transparent, while maintaining the original structure. In this dissertation, the samples used for (S)TEM analysis were prepared by a standard manual grinding and thinning process followed by an ion milling procedure in a precision ion polishing system (PIPS 691, Gatan). A thin area with a thickness below 100 nm can been obtained around the hole.

2.2.3 Scanning probe microscopy (SPM)

Scanning probe microscope consists of a family of microscopy froms where a sharp probe is scanned across a surface and some probe: sample interaction or interactions are monitored. Two primary SPM consist of scanning tunneling microscopy, atomic force microscopy (AFM) (contact-mode, tapping mode, non-contact mode). Other forms

include electric force microscopy, lateral force microscopy, piezoresponse force microscopy (PFM), magnetic force microscopy (MFM), conductive AFM etc. The variety of functionalities of SPM making it a fast and accurate technique to characterize materials to get informations about morphology, charge distribution, ferroelectricity, resistivity and so on.

Figure 2.4 illustrates how Atomic Force Microscopy works. AFM takes advantage of the repulsive force between the sample surface and the cantilever tip in contact with it. When scanning the tip across the sample surface, the vertical movement of the tip follows the surface profile, leading to a deformation of the cantilever, which can be measured with the reflected laser spot on the photo detector. By keeping the force constant when scanning, the cantilever deformation calculated surface profile can be recorded as the surface topography by the AFM.

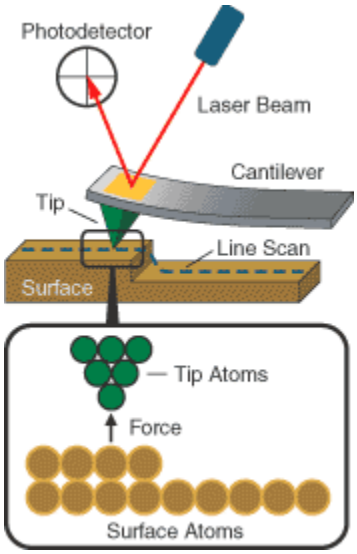

Figure 2. 4 Schematic set-up for an atomic force microscope. [128]

2.3 Magnetic and magnetotransport measurements

Magnetic and transport properties were measured using a Physical Property Measurement System (PPMS Model 6000, Quantum Design) installed with vibrating sample magnetometer (VSM). It can provide magnetic field in the range of ±9T and temperature from 1.9-400K with liquid He and heater. The temperature sweep rate ranges from 0.01 K/min to 12 K/min. Superior temperature control within 2 mK is achieved in this system assisted by a monitor thermometer adjacent to the sample.

For magnetization measurement, the sample is put in the VSM. Figure 2.5 gives diagram of sample holder and detection mechanism for VSM measurement. A sample is placed under an external uniform magnetic field and get magnetized. Then, the sample gets physically vibrated sinusoidally, typically by using a piezoelectric material. Commercial systems use linear actuators of some form, and historically the development of these systems was done using modified audio speakers, though this approach was dropped due to the interference through the in-phase magnetic noise produced, as the magnetic flux through a nearby pickup coil varies sinusoidally. The induced voltage in the pickup coil is used to calculate the sample's magnetic moment, as it is proportional with the sample's magnetization. While the applied outside magnetic field doesn't contribute to induce voltage in the coil. In a typical setup, the induced voltage is measured through the use of a lock-in amplifier using the piezoelectric signal as its reference signal. By measuring in the field of an external electromagnet, it is possible to obtain the hysteresis curve of a material. The vibrating sample magnetometer measures the magnetization of a

small sample of magnetic material placed in an external magnetizing field by converting the dipole field of the sample into an AC electrical signal.

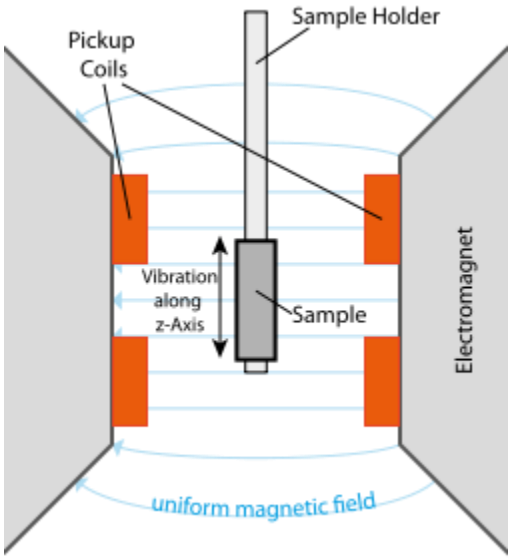

Figure 2. 5 Vibrating Sample Magnetometer - sample holder and detection mechanism.

For resistivity measurement, four point probe method with van der pauw configuration are used, shown as Figure 2.6. 100 nm gold electrodes were deposited with shadow mask by magnetron sputtering as the contact. There are two resistivity options in the PPMS system. AC transport option is optimized for samples from nΩ to kΩ and thus can be used to measure highly conducting materials such as metals. DC resistivity option is optimized for samples whose resistance is in the range of ~Ω to ~MΩ and thus can be used to measure the conducting and semiconducting materials. It can measure a resistance up to 5×10^6 Ω. The magnetotransport properties in this dissertation are conducted by the DC resistivity measurement due to relative large resistance in these nanocomposites.

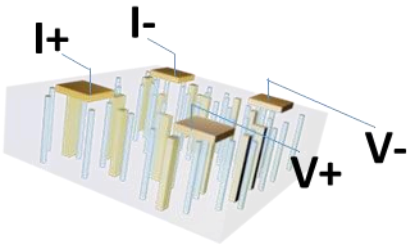

Figure 2. 6 The typical van der Pauw measurement setup for transport property investigation.

CHAPTER III

ENHANCED TUNABLE MAGNETORESISTANCE PROPERTIES OVER A WIDE TEMPERATURE RANGE IN EPITAXIAL $(LA_{0.7}SR_{0.3}MNO_3)_{1-x}$: $(CEO_2)_X$ NANOCOMPOSITES

3.1 Overview

Vertically aligned nanocomposite (VAN) $(La_{0.7}Sr_{0.3}MnO_3)_{1-x}$:$(CeO_2)_x$ (LSMO:CeO_2) thin films have been grown on $SrTiO_3$ (001) substrates by pulsed laser deposition (PLD). Tunable magnetoresistance properties as well as microstructures are demonstrated in these VAN films by modulating the film composition (x=0, 0.3, 0.4, 0.45, 0.5, and 0.55). The sample of x=0.3 shows a large low-field magnetoresistance (LFMR) in a high temperature range, i.e. over 10% at the range of 280 K to 320 K under 1 T and with a peak value of ~13.5 % at 310 K. While a vast enhancement of LFMR in a low temperature range of 20-150 K with peak of ≈34.3 % at 45 K for 1 T could be achieved with x=0.5. The enhanced LFMR properties can be attributed to both the phase boundary induced spin fluctuation and the magnetic tunneling effect through vertical ferromagnetic/insulator/ferromagnetic structures. The observed enhanced LFMR performance, especially at high temperatures, as well as its simple growth method offer LSMO: CeO_2 nanocomposites great potential to be used in spintronic devices in a large temperature range.

This chapter is reprinted with permission from "Enhanced tunable magnetoresistance properties over a wide temperature range in epitaxial $(La_{0.7}Sr_{0.3}MnO_3)$1-x: (CeO_2)x nanocomposites" by M. Fan, et al., Journal of Applied Physics, 2015, 118, 065301. © 2015 AIP Publishing LLC

3.2 Introduction

Half metallic mixed valence $La_{1-x}Sr_xMnO_3$ (LSMO) with high Curie temperature (T_C) has gained significant interests in the past decades due to their unique magnetic and transport properties [129,26,4]. Large intrinsic colossal magnetoresistance (CMR) were demonstrated in such materials, making them especially promising for spintronic device applications [106]. While such CMR phenomenon can only occur at high magnetic field (several Tesla), recently extensive efforts have been devoted to explore their extrinsic low field magnetoresistance (LFMR) properties [130,131,132]. It has been demonstrated that magnetoresistance (MR) behavior in LSMO at much lower magnetic fields could be obtained by natural or artificially introduced grain/phase boundaries, where spin polarized tunneling/scattering might occur [130,132]. Incorporating a secondary phase is an effective way to improve the LFMR in both composite bulk and thin films [26,131,133,43,134,135]. Enhanced LFMR, for example, -30% at 154K and 1T in $(LSMO)_{0.5}$: $(ZnO)_{0.5}$ columnar film [76], -33% at 10K and 0.5T for LSMO: MgO composite film on LAO substrate [134], -41% at 10K and 1T in $(LSMO)_{0.3}$: $(NiO)_{0.7}$ thin films [43], and 75% at 20K and 1T in LSMO: ZnO percolation threshold [135,75], have been achieved. However, LFMR in both polycrystalline LSMO and composite thin films have always been reported only in the temperature range well below T_C. Large LFMR in high temperature range is of interests for higher temperature memory devices and thus worth investigation. It has been previously predicted that high-temperature LFMR in LSMO composite films can be induced by tuning the grain size and spin coupling at the phase boundaries [43].

Vertically aligned nanocomposite (VAN) thin films in which two immiscible phases could achieve self-assembled co-epitaxial growth offers a powerful solution for microstructure tuning and interface coupling [61]. Greatly improved and controllable LFMR properties have been demonstrated in VAN LSMO: ZnO [135,75], LSMO: Mn_3O_4 [136], LSMO: NiO [43] , LSMO: CeO_2 [133] films. However, enhanced LFMR in high measurement temperature range is still lacking as most of the LSMO nanocomposite work was demonstrated with high secondary phase concentration and MR enhancement at low temperatures.

In this work, we investigated the epitaxial $(La_{0.7}Sr_{0.3}MnO_3)_{1-x}$: $(CeO_2)_x$ $(L_{1-x}C_x)$ VAN nanocomposite films on $SrTiO_3$ (001) (STO) substrate with the goal to tune the LFMR properties in the high temperature range. CeO_2, with a wide band gap of 5.5-8 eV [137], is chosen as the secondary phase because of its simple structure and good lattice match with both LSMO and STO as well as the extreme refractory property [131133]. Enhanced LFMR in a wide temperature range have been observed, and discussed with the unique structural domain architectures.

3.3 Experimental

$L_{1-x}C_x$ nanocomposite films (thickness of ~40-60nm) with x=0, 0.3, 0.4, 0.45, 0.5, and 0.55, corresponding to an approximate volume percentage of CeO_2 of 0%, 22%, 30.6%, 35%, 39.8%, and 44.6%, respectively, were deposited on single crystalline STO (001) substrates by pulsed laser deposition (PLD). The composite targets were prepared with a conventional ceramic sintering process from high purity stoichiometric La_2O_3, $SrCO_3$, MnO_2 and CeO_2 powders. During deposition, substrate temperature was kept at

750 ℃ and a 200 mTorr oxygen pressure was maintained. KrF excimer laser (λ=248nm) with a repetition rate of 10 Hz was used. After deposition, all films were cooled at 10 ℃/min under 200 Torr O_2. X-ray diffraction (XRD) (PANalytical Empyrean XRD) and transmission electron microscopy (TEM) (FEI Tecnai G2 F20 operated at 200 kV) were used to analyze the crystallinity and microstructure of the as-deposited films. Magnetotransport properties were examined using a Physical Property Measurement System (PPMS Model 6000, Quantum Design) in a four point probe configuration (in Van der Pauw geometry) with magnetic field applied out-of-plane. 100 nm gold electrodes as the contacts were deposited with shadow mask by magnetron sputtering. The MR is evaluated by the following equation: MR (%) = $[(\rho_0-\rho_H)/\rho_0] \times 100\%$, where ρ_H, ρ_0 are the electrical resistivity with and without applied magnetic field, respectively.

3.4 LSMO: CeO_2 film growth and microstructure

Figure 3.1a shows XRD *θ-2θ* plots of the $L_{1-x}C_x$ nanocomposite films. In the composite films, both LSMO and CeO_2 grow highly textured along (00*l*) on STO substrate without any obvious impurity peak. This is expected from the good lattice matching between LSMO (a = 3.870 Å) and STO (a = 3.905 Å), as well as CeO_2 with a 45° rotation and STO, since $a_{CeO2}/\sqrt{2}$ =5.411 Å/$\sqrt{2}$=3.83 Å. In addition, for $L_{0.7}C_{0.3}$, diffraction peaks originated from the CeO_2 (022) might also exist and overlap with LSMO (002) due to the similarity of the lattice spacing, which is confirmed by SAED pattern (inset of Figure 3.1a). A left shift of LSMO (00*l*) peak is associated with increasing CeO_2 atomic ratios, as clearly shown in the enlarged LSMO (002) region in Figure 3.1c, which indicates the increase of LSMO out-of-plane *d* spacing in Figure 3.1b. This suggests that the strain state

of LSMO is converted from -0.49% compressive strain (~3.851Å) for x=0 to a 0.59% tensile strain (~3.893Å) for x=0.5. This is possibly due to the vertical lattice coupling between LSMO (a = 3.870 Å) and CeO_2 (a=5.411 Å) and increased vertical strain applied to LSMO with increasing CeO_2 composition. In pure LSMO film, lattice mismatch between LSMO with STO substrate leads to an in-plane tensile strain and an out-of-plane compressive strain ($a_{LSMO}<a_{STO}$) on LSMO; however, the lattice mismatch between CeO_2 and LSMO favors a tensile strain on LSMO in the out-of-plane direction, which drives the strain state from the compressive strain to an tensile strain with increasing CeO_2 concentration. ϕ scans were conducted to investigate the in-plane orientation relationship of these two phases on STO. As shown in Figure 3.1d, LSMO shows a clear cube-on-cube growth with LSMO (110)// STO (110), while CeO_2 shows an in-plane rotation of 45° relative to the STO substrate, i.e., CeO_2(110)//STO(100).

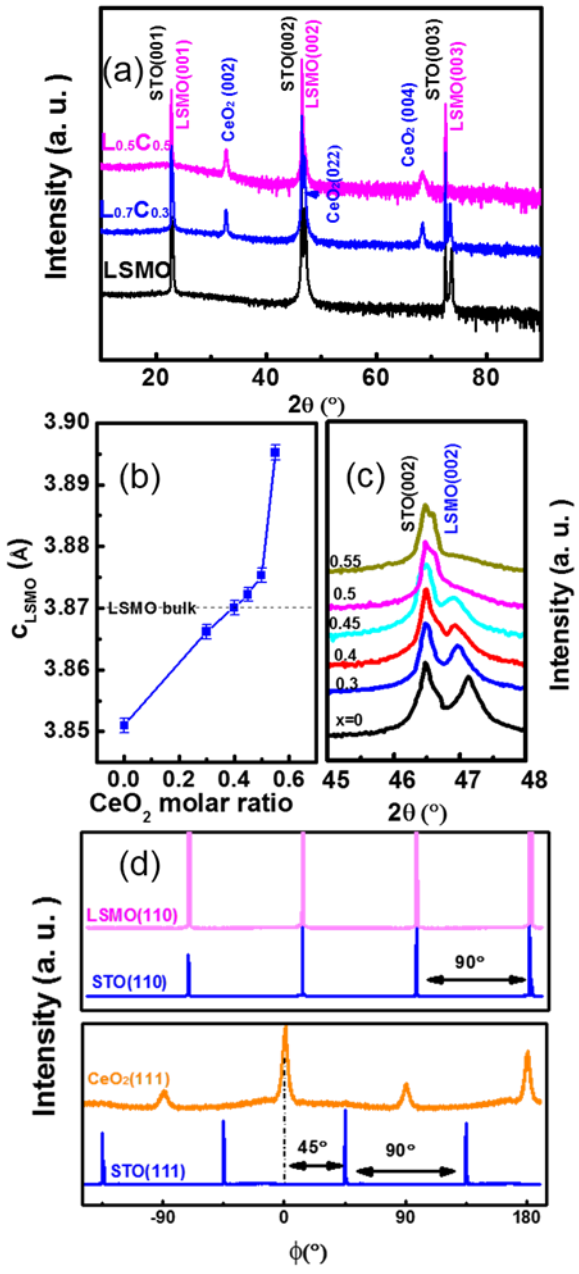

Figure 3. 1 (a) XRD θ-2θ scan of LSMO:CeO_2 nanocomposite and pure LSMO film. (b) out-of-plane lattice parameter of LSMO with different CeO_2 molar ratio. (c) Enlarged local XRD results of the nanocomposites with various CeO_2 concentration. (d) ϕ scan of STO (111), CeO_2 (111), STO(110) and LSMO (110) planes of $(LSMO)_{0.5}(CeO_2)_{0.5}$.

To further investigate the microstructures of the nanocomposites, detailed plan-view and cross-section TEM studies were conducted on all the samples with various compositions. Figure 3.2 shows the plan-view TEM images for three different compositions (x=0.3, 0.4, and 0.5), confirming the epitaxial growth of both LSMO and CeO_2. Interestingly, very different domain structures have been developed with various CeO_2 concentrations. Low magnification and high resolution TEM images in Figure 3.2a and b of sample x=0.3 shows rectangular domains of CeO_2 embedded in LSMO matrix, with clear and sharp phase boundaries. The rectangular domains have a width of 1-2 nm and two preferred orientations orthogonal to each other. When x increases to 0.4, the rectangular domains become wider to 2-3nm with the average width of ~2.64 nm. Further increasing x to 0.5 (Figure 3.2d), high density circular domains of CeO_2 with domain size of ~3-7nm emerge with rectangular ones. At the same time, phase boundary roughness becomes significant. Different domain structures are critical for the magnetic and transport properties, which are discussed in a later section.

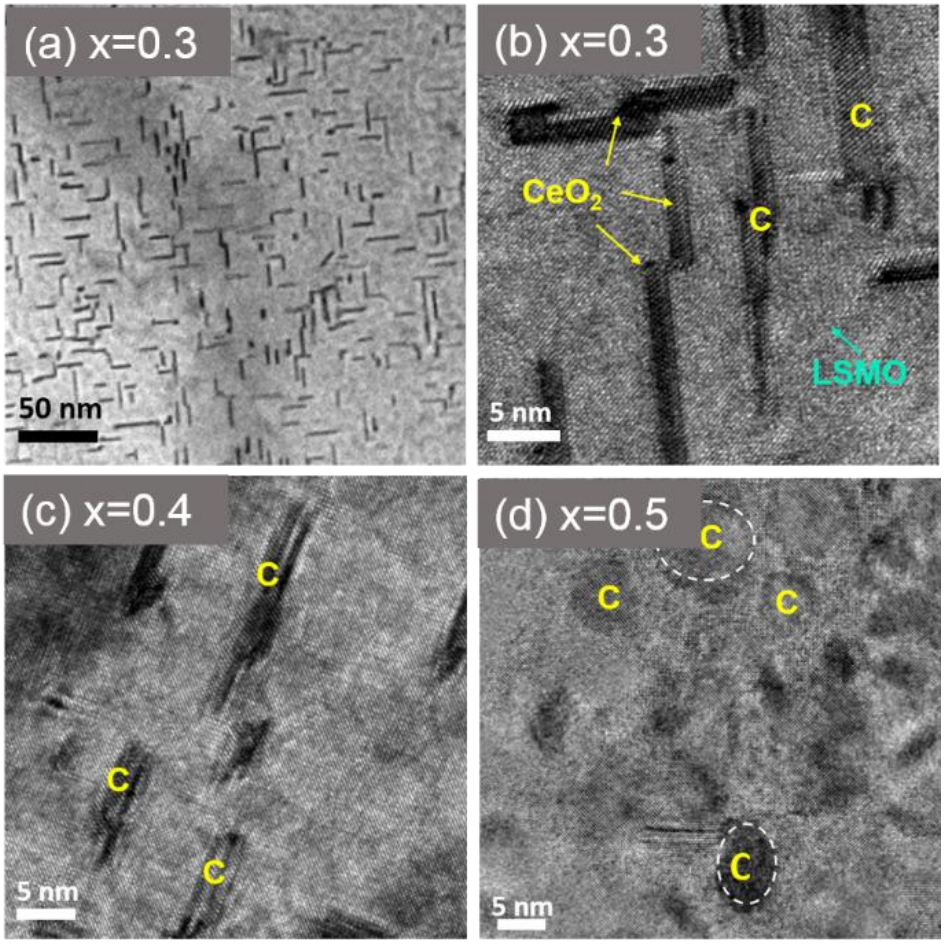

Figure 3. 2 (a) Low-magnification plan view TEM image of $(LSMO)_{0.7}(CeO_2)_{0.3}$ nanocomposites. High resolution TEM images of plan view samples of $(LSMO)_{1-x}:(CeO_2)_x$ with different CeO_2 atomic concentration: (b) x=0.3; (c) x=0.4; (d) x=0.5.

Cross-sectional TEM images of $L_{0.7}C_{0.3}$ and $L_{0.5}C_{0.5}$ are shown in Figure 3.3 a, c and b, d, respectively. The images clearly show LSMO and CeO_2 columns vertically grown on STO substrate. Distinct diffractions from LSMO and CeO_2 in the selected area electron diffraction (SAED) pattern indicate high quality epitaxial growth of both phases in the nanocomposite films. The orientation relationship can be determined to be $CeO_2(002)\|LSMO(002)\|STO(002)$ and $CeO_2[220]\|LSMO[200]\|STO[200]$ in $L_{0.5}C_{0.5}$, consistent with the above XRD results, i.e., LSMO grows cube-on-cube, while CeO_2

grows with a 45° in-plane rotation relatively to the STO substrate. While in $L_{0.7}C_{0.3}$, double-epitaxial CeO_2 with a second orientation of CeO_2 (022)‖LSMO(002)‖STO(002) with CeO_2[200]‖LSMO[200]‖STO[200] can be seen, which might be resulted from the smaller CeO_2 molar ratio and limited adatoms' diffusion during the growth. A similar double-epitaxial growth was reported for $LaFeO_3$ on STO (001) substrates [138]. From the high-resolution TEM (HRTEM) image, different atomic lattice fringes for two phases can be clearly distinguished, shown in the inset. The rectangular shaped lattice fringes correspond to CeO_2 lattice and the square shaped fringes correspond to LSMO. CeO_2 domain with size of 1-2nm for $L_{0.7}C_{0.3}$ and 3-7nm for $L_{0.5}C_{0.5}$ can be identified and is consistent with the plan-view images.

3.5 Resistivity and magnetotransport properties of LSMO:CeO_2 VAN films

Temperature dependent zero-field resistivity (R-T) curves of the $L_{1-x}C_x$ nanocomposite films are examined in Figure 3.4a. It can be seen that, with increasing CeO_2 composition the resistivity of the nanocomposite increases in the entire temperature regime, while the metal-insulator transition temperature (T_{MI}) decreases at the same time. This property modulation by insulating CeO_2 may be attributed to the phase boundary effect, which has been proposed previously [133, 76]. Insulating CeO_2 embedded in LSMO matrix could serve as energy barriers among LSMO domains, and introduce magnetic disorder at phase boundaries. The resistivity above T_{MI} can be fitted by the adiabatic small-polaron hopping model: $\rho = \rho_a T exp(E_a/(k_B T))$, where E_a is the activation energy which could suggest the barrier height of the phase boundary [133]. The fitted E_a value increases with increasing CeO_2 molar ratio, from 0.05304 eV for x=0.4 to0.06711 eV and

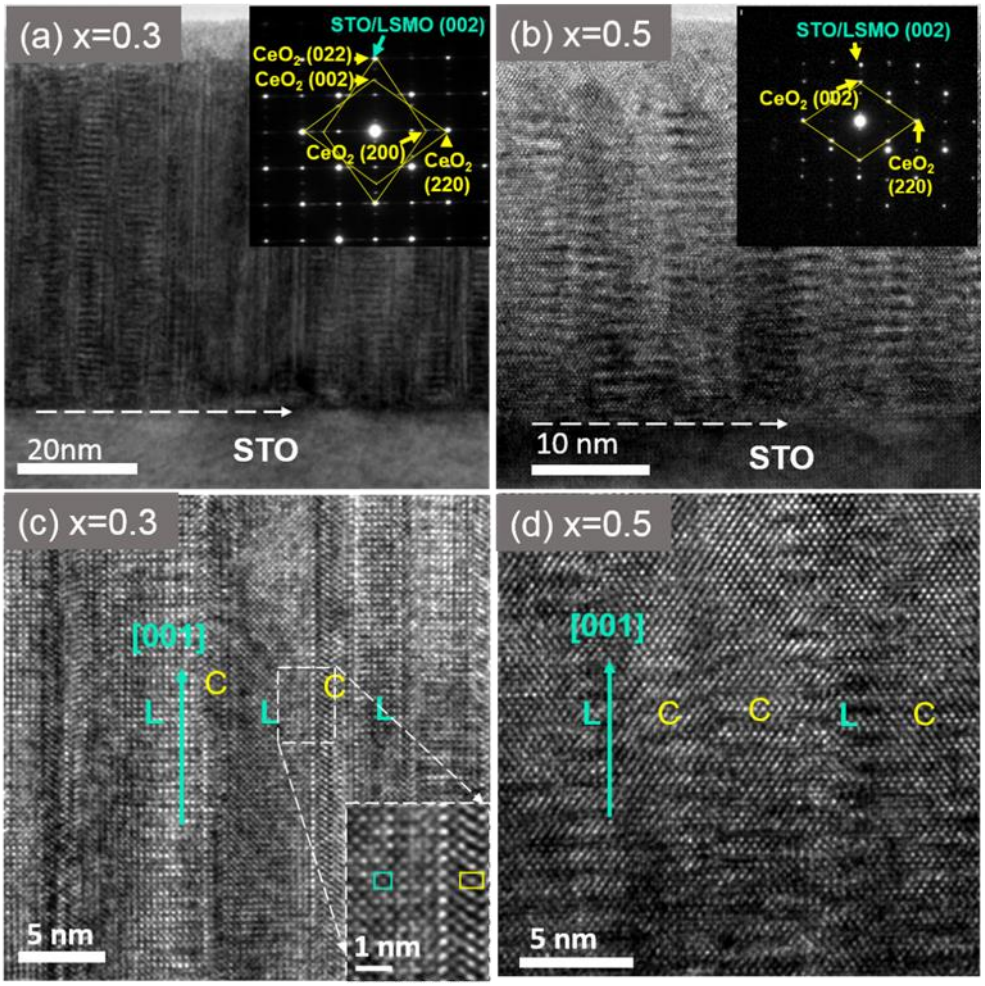

Figure 3. 3 Low magnification cross-section TEM image and corresponding Selected Area Electron Diffration (SAED) pattern (inset) of (a) x=0.3 and (b) x=0.5 sample. High resolution Cross-section TEM images of sample of (c)x=0.3, (d)x=0.5. Inset of (c) shows higher magnification image of the outlined region in (c).

0.07025 eV for x=0.45 and 0.5, respectively. The resistivity below T_{MI} is fitted using a parallel connection channel model [13176], given by $1/\rho=G/\rho_i+1/\rho_{LSMO}$, where ρ_i and ρ_{LSMO} denote the resistivity for insulating and conducting channels, respectively. The geometrical factor (G) suggests the relative contributions of insulating channel. The fitting results indicate a dramatic increase of G with increasing CeO_2 concentration, with G of 1 for x=0.3 to G of 26.34 and 42.09 for x=0.4, 0.45, respectively. Insert of Figure 3. 4a

shows the resistivity fitting curve of x=0.45 sample. Both regimes fit well and suggest the enhanced phase boundary effect with increasing CeO_2 concentration. In addition, it is believed that the strain may have impacts on both the magnetic and transport properties of LSMO thin films [139,140], e.g., T_{MI} could decrease with both compressive and tensile strain [139]. While the reports also suggested that the LSMO films under small strain ($|\varepsilon| \leq 0.6\%$) show properties quite similar as that of the single crystal counterpart, e.g., Tc in the range of 340-370K [139]. In this case, the strain of LSMO is relatively small, i.e. from ~-0.49% to ~0.59%. Thus the strain effect in this system could be relatively minor compared to the phase boundary effects.

The magnetoresistance (MR) results of the nanocomposite films are plotted in Figure 3.4b. It is clear that each composite film has its specific MR peak. With the increasing CeO_2 concentration, the MR peak magnitude increases and the peak position shifts to lower temperature, which couples with T_{MI}. Noted here, quite large MR values at the high temperature range, i.e., over 10% for the range of 280-320 K and with a peak value of ~13.5 % at 310 K under 1 T, could be observed in the $L_{0.7}C_{0.3}$ film. The high temperature LFMR performance reported here is superior to previous reported values, e.g. 8% at 280 K, 1 T with negligible MR at 300 K for $LSMO_{0.8}$:$ZnO_{0.2}$ film [135], and a high MR% of ~15 % at 200-270 K, 1 T but a low MR% of ~5% at 300 K in nano-checkerboard-like LSMO:NiO nanocomposite films [43]. The current result is even comparable with the MR% of 11% at 300 K, 0.9 T reported in double perovskite $Sr_2FeMoO_6/Zn_xFe_{1-x}Fe_2O_4$ (SFMO/ZFO) composite [141]. Furthermore, for samples with higher CeO_2 concentrations, MR enhancement is more significant at a lower temperature range, with the maximum

value of ~34.3% achieved at 45 K for $L_{0.5}C_{0.5}$. The great LFMR performance in VAN LSMO: CeO_2 nanocomposite films is highly desirable for the applications in both room temperature and low temperature spintronic devices.

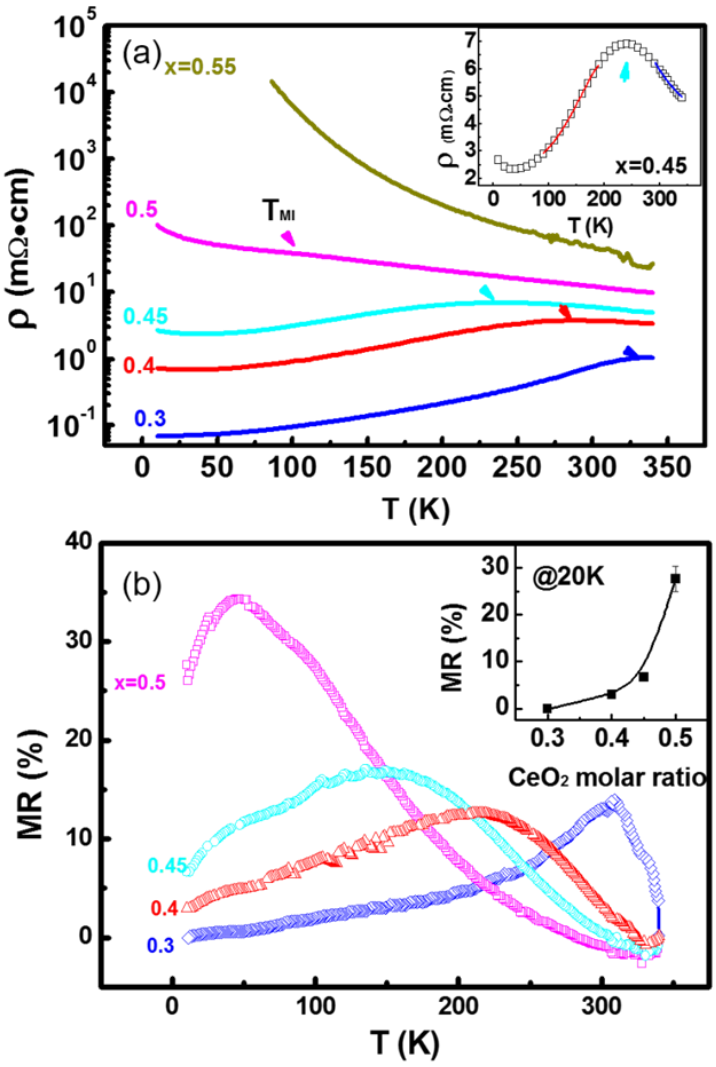

Figure 3. 4 (a) R-T plot of $(LSMO)_{1-x}:(CeO_2)_x$ nanocomposites. Inset of (a) shows fitting of the electrical resistivity of the x=0.45 sample. (b) Temperature dependence of MR for $(LSMO)_{1-x}:(CeO_2)_x$ nanocomposites. Inset of (b) shows MR at 20K for each CeO_2 concentration.

Overall the systematically tunable LFMR enhancement close to T_{MI} in LSMO:CeO_2 could be attributed to the enhanced spin-fluctuation depression effect, mechanism similar to that of CMR [76]. For the case of CMR, it is believed that the competition between super exchange coupling and double exchange interaction could induce a strongly perturbed spin lattice in the regime of the ferromagnetic transition and construction of magnetic polarons [25]. Under magnetic field, the spin-fluctuation gets depressed, leading to a dramatic drop of the resistivity near the transition temperature [25] [76]. In the case of LSMO:CeO_2, with increasing CeO_2 concentration, the increased disorders introduced by the secondary phase CeO_2 could further enhance the spin-fluctuation suppression effect, leading to an systematically increased MR near T_{MI}. The large high-temperature MR in $L_{0.7}C_{0.3}$ is correlated with the unique domain structure of CeO_2 for this composition, i.e., the rectangular domains with the width as fine as 1-2 nm and sharp LSMO/CeO_2 interfaces (Figure 3.2b), which favors a good balance between spin fluctuation for enhancing LFMR and the insulating phase boundary effects for maintaining high T_{MI}. At the same time, at temperatures well below T_{MI}, tunneling magnetoresistance (TMR) effect in vertical LSMO/CeO_2/LSMO junctions can contribute strongly to enhance LFMR. Shown as the inset of Figure 3.4b, MR at 20 K shows monotonous increase with increasing CeO_2 molar ratio, with a vast enhancement emerging at x=0.5. This could be attributed to the fully decoupled FM domains of LSMO at this composition near the percolation threshold, which has been previously reported [135].

3.6 Summary

In summary, the microstructure and magnetotransport properties of $(LSMO)_{1-x}:(CeO_2)_x$ nanocomposite thin films with various molar ratios of CeO_2 secondary phase have been explored. Two-phase growth and systematically tunable LFMR at different temperature regimes have been achieved with unique domain structures. The enhanced LFMR is attributed to a spin-fluctuation depression mechanism close to T_{MI} and spin-dependent tunneling effect in FM/I/FM junctions at low temperatures. This suggests that both phase boundary density and secondary phase morphology play a key role in the overall magnetotransport properties. The results also demonstrate the great potential of two-phase VANs with enhanced LFMR, especially at high temperatures, towards the room temperature spintronics.

CHAPTER IV

MICROSTRUCTURE, MAGNETIC AND TRANSPORT PROPERTIES OF $(LA_{0.7}SR_{0.3}MNO_3)_2$: $(CUO)_1$ NANOCOMPOSITE THIN FILMS

4.1 Overview

$(La_{0.7}Sr_{0.3}MnO_3)_2$: $(CuO)_1$ (LSMO: CuO) nanocomposite thin films fabricated on $SrTiO_3$ (001), $LaAlO_3$ (001) and MgO (001) substrates by pulsed laser deposition were investigated in respect of the microstructure, magnetic and electrical properties. X-ray diffraction (XRD) and transmission electron microscopy (TEM) results show that LSMO: CuO films grow as highly textured self-assembled vertically aligned nanocomposite (VAN), with a systematic domain structure and strain tuning effect. High low-field magnetoresistance of 80% are achieved in LSMO: CuO grown on $LaAlO_3$ (001) substrate.

4.2 Introduction

Metallic ferromagnetic materials have received much interest due to the technically importance in the emerging spintronics field. Among them, mangantites with chemical formula of $A_{1-x}R_xMnO_3$, in which A-cations usually are La, Pr, and Nd and R-cation Sr, Ca, Ba, is specially an important family of compounds. The colossal magnetoresistance (CMR) induced properly by "double-exchange" mechanism in mangantites draw them intensive research [26,4]. In addition to the intrinsic CMR phenomenon, extensive efforts have been devoted to explore their extrinsic low field magnetoresistance (LFMR) properties recently [130,132]. It has been demonstrated that MR behavior in $La_{1-x}Sr_xMnO_3$ (LSMO) at much lower magnetic fields could be obtained by natural or artificially introduced grain/phase boundaries, where spin polarized tunneling/scattering might occur. Efforts have been devoted to incorporate a secondary phase which are demonstrated to be an effective way to improve the LFMR in both composite bulk and thin films [26,43,134,135]. Enhanced LFMR have been obtained in nanocomposites of LSMO: CeO_2 [19], LSMO: ZnO [76], LSMO: NiO [43], LSMO: MgO [142], etc, for different temperature range and magnitude.

However, pioneer work for enhancing the extrinsic low-field magnetoresistance (LFMR) by incorporating a secondary phase all used wide-bandgap insulators, which induce high energy barrier and large resistivity at the same time [43, 142]. In addition, the effects of substrate on the performance of the films is rarely reported. In this work, we investigated the epitaxial $La_{0.7}Sr_{0.3}MnO_3$ based nanocomposite films using CuO as the secondary phase and investigated the magnetic and transport properties of the films on

different substrates. CuO is a small bandgap semiconductor with Eg of ~1.2eV [143], and also an antiferromagnetic material with Neel temperature (T_N) of ~215K [144]. The LSMO: CuO nanocomposite films were grown on $SrTiO_3$ (001) (STO), MgO (001) and $LaAlO_3$ (001) (LAO) substrates by PLD under different frequency. Enhanced and systematically tunable LFMR are achieved, correlated with the columnar structures as well as the strain states.

4.3 Experimental

All the thin films were prepared by pulsed laser deposition (PLD) with KrF excimer laser (λ = 248 nm). Before the deposition, the chamber was pumped down to $<10^{-6}$ Pa. During the deposition, adjustable deposition frequency (1 to 10Hz), oxygen pressure, were used for optimization and investigation. The composite targets used were prepared using a conventional solid state sintering process from high purity stoichiometric powders, i.e, La_2O_3, $SrCO_3$, MnO_2, CuO. The powders were mixed well and pressed into pellets first. Then the pellets were annealed at 1300 °C, forming condense targets.

The crystallinity and microstructures of the films were investigated by X-ray diffraction (XRD) (PANalytical Empyrean XRD), and transmission electron microscopy (TEM) (FEI Tecnai G2 F20 operated at 200kV). The samples used for TEM analysis were prepared by a standard manual grinding and thinning process followed by an ion milling procedure in a precision ion polishing system (PIPS 691, Gatan). Magneto-transport properties were examined using a Physical Property Measurement System (PPMS Model 6000, Quantum Design) in a four point probe configuration (in Van der Pauw geometry) with magnetic field applied out-of-plane. 200-nm-thick gold electrodes as the contacts

were deposited with shadow mask by magnetron sputtering. The MR is evaluated by the following equation: MR (%) = $[(\rho_0-\rho_H)/\rho_0] \times 100\%$, where ρ_H, ρ_0 are the electrical resistivity with and without applied magnetic field, respectively. The magnetizations of the films were measured with Vibrating Sample Magnetometer (VSM) in the PPMS system.

4.4 Thin film growth and microstructure of LSMO: CuO VAN films

Figure 4. 1a shows XRD θ-2θ plots of the LSMO: CuO nanocomposite films on MgO, STO and LAO substrates under 10Hz. For all the composite films, both LSMO and CuO grow highly textured on STO substrate without any obvious impurity peak. LSMO grown epitaxially along the (00l) of the substrates, and CuO grown along (110) and (111) direction. For films under different frequency, a left shift of LSMO (00l) peak is associated with increasing growth frequency (XRD not shown here), which indicates the increase of LSMO out-of-plane d spacing. The derived out-of-plane lattice parameter of LSMO is plotted in Figure 4.1b. It can be observed that LSMO suffered with a compressive strain for all the samples, which implies that the substrate strain is still impressive, for the film thickness of ~65nm. While the lattice mismatch between the LSMO and CuO gives a small out-of-plane tensile strain. This is possibly due to the vertical lattice coupling between LSMO (a = 3.870 Å) and CuO (c (110) *2= 5.5 Å) and increased vertical strain applied to LSMO with increasing growth frequency. Figure 4.1c displays the out-of-plane d spacing of LSMO and CuO as respect of the substrates. Distinguish strain states for the samples can be seen for different substrates. The film on LAO shows up with the largest out-of-

plane tensile strain of ~2.6%, followed by that of 0.5% and -0.25% for MgO and STO, respectively.

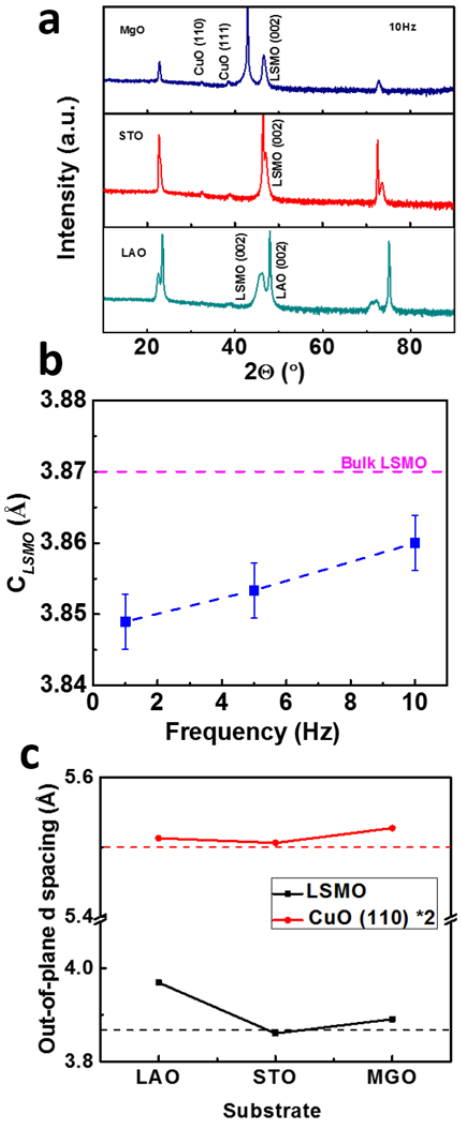

Figure 4. 1 a) XRD θ-2θ plots of LSMO: CuO nanocomposite films on MgO (001), STO (001) and LAO (001) substrates. b) out-of-plane lattice parameter of LSMO in LSMO:CuO films grown on STO under different frequency. c) out-of-plane d spacing of LSMO and CuO in LSMO: CuO films on different substrates.

The microstructures of the LSMO: CuO nanocomposite films were investigated with TEM imaging. A systematical microstructure tuning effect were observed with different growth frequency. Figure 4. 2a and c are the cross-sectional TEM images of LSMO: CuO on STO (001) grown under 1Hz and 10Hz respectively. The corresponding selective area electron diffraction pattern (SAED) shown in inset of Figure 4. 2a with distinguish diffraction dots indicate high quality epitaxial growth of the nanocomposite films. The domain size is greatly reduced with increased deposition frequency. Clearly large clusters with the dimension in the range of 100-200nm and separated with ~200nm can be observed in the LSMO matrix for the sample under 1Hz. In addition, significant outer growth can be seen for the clusters. However, for the film grown under high frequency of 10Hz, shown in Figure 4. 2c, the film is much smoother, the column size is in the range of ~10-20nm with much smaller spacing. The systematical domain size tuning effect is consistent with the diffusion model previously used to describe similar self-assembled systems [11679], as the ad-atoms of one phase can diffuse longer time to form larger domain under slow growth rate. Interestingly it can be noticed that both straight and oblique CuO domains exist in the films. High resolution TEM image of Figure 4. 2b and 2d gives an out-of-plane d spacing of 0.23nm, 0.27nm for the oblique and straight CuO pillars, corresponding to CuO (111) and CuO (110), respectively, consistent with the XRD results.

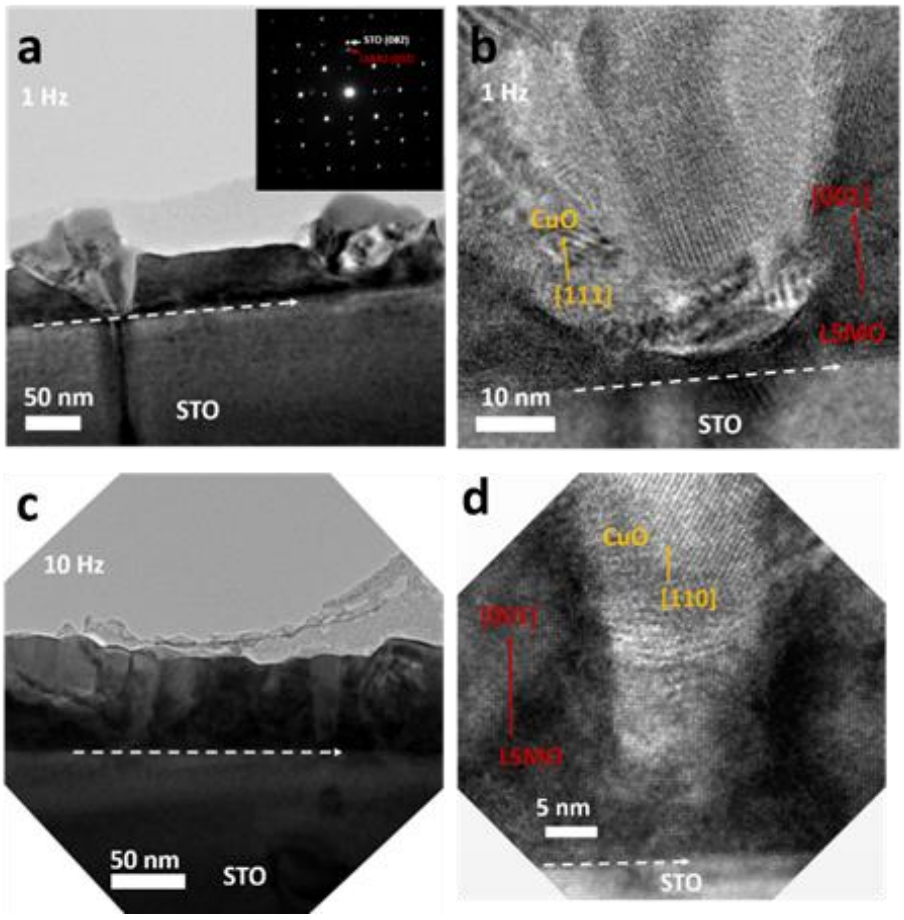

Figure 4. 2 Microstructures of LSMO: CuO nanocomposite films a) and b) Cross-sectional TEM image of LSMO: CuO on STO (001) grown under 1Hz. Inset of a) is the corresponding SAED pattern. C and d) Cross-sectional TEM images of LSMO: CuO on STO (001) grown under 10Hz.

In order to examine the chemical distribution in the LSMO: CuO system, X-ray energy-dispersive spectroscopy (EDS) analyses were perform with STEM imaging. Figure 4. 3 shows typical EDS mapping result of the LSMO: CuO film on LAO substrate grown under 10Hz. The features of straight and oblique CuO nanopillars embedded in the LSMO matrix are clearly seen in the distributions of each element. No obvious inter-diffusion exist in between the CuO pillars and LSMO matrix. Both the TEM, STEM and

the EDX results suggest that the LSMO: CuO has been grown as highly epitaxial self-assembled nanocomposite.

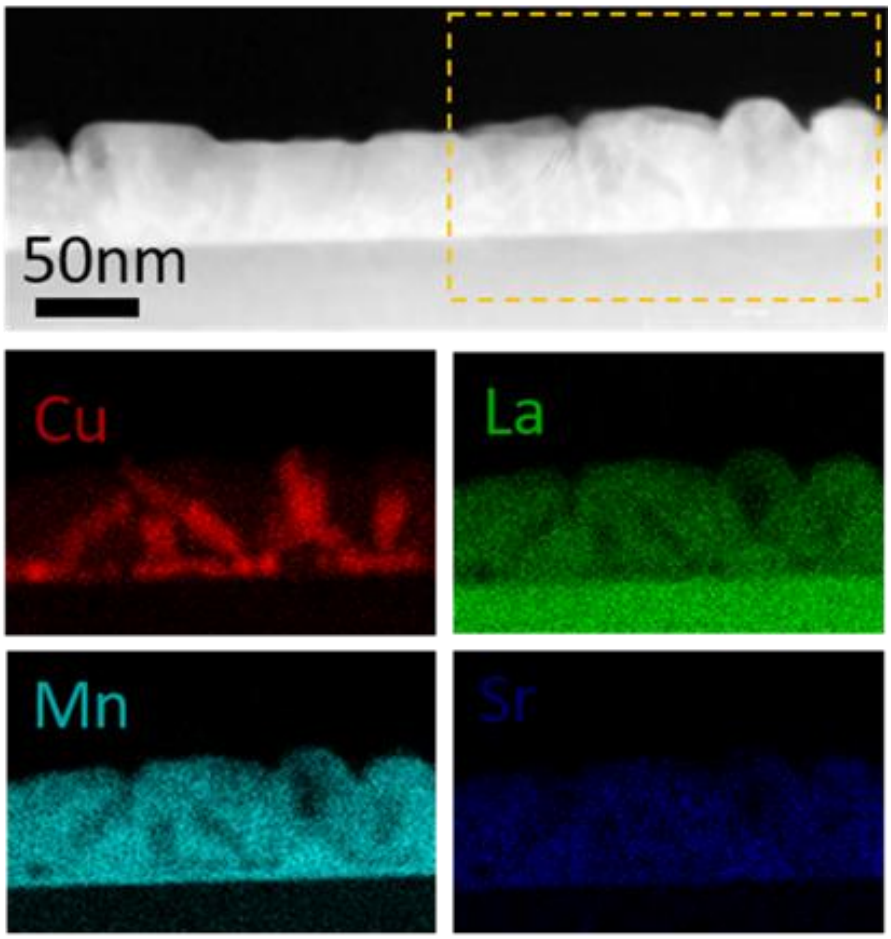

Figure 4. 3 STEM and EDX mapping results of LSMO: CuO on LAO (001) substrate grown under 10Hz.

4.5 Magnetic and magnetotransport properties of LSMO: CuO VAN films

The temperature dependent resistance R-T curve for the nanocomposite films deposited under different laser frequencies is plotted in Figure 4.4a. It can be observed that with increasing frequency, the resistance of the nanocomposite increases, and the metal-insulator transition temperature shifts to lower temperatures. This property

modulation is mainly correlated with the enhancement of the phase boundary and grain boundary effect due to reduced domain size and increased disorder [197976], as observed in the TEM images, rather than the strain effect. As the strain such films is relatively small, which is less than 0.6%, here the strain effect could be neglected compared to the phase boundary effect. The MR results measured under 1T in terms of frequency are plotted in Figure 4. 4b. With increasing deposition frequency, the MR peak magnitude increases and the peak position shifts to lower temperature, which couples with T_{MI}. The MR peak value is derived to be 8% at 275K, 9% at 235K and 14% at 195K, for 1Hz, 5Hz and 10Hz, respectively. The increase of MR and decrease peak position can be attributed to the increased decoupling of LSMO domains because of the reduced domain size and enhanced disorder at the phase regions.

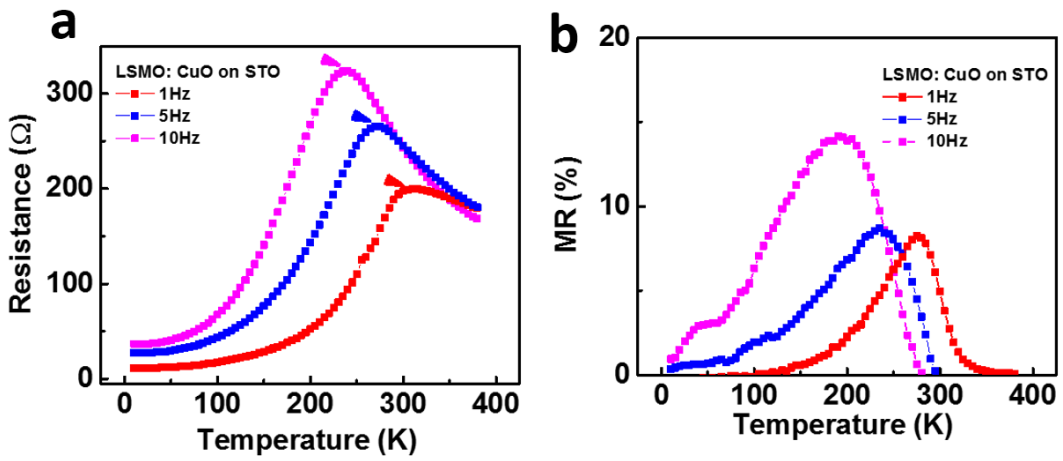

Figure 4. 4 a) R-T and b) MR-T curves for LSMO: CuO films on STO under different laser frequencies. Measurement is under 1T.

Then the magnetic and transport performance of the LSMO: CuO films on different substrates LAO (001), MgO (001), STO (001) were compared. Figure 4. 5a

plotted the temperature dependent magnetization (M-T) behavior of the LSMO: CuO films grown under 10Hz on these substrates. The Curie temperature (Tc) can be derived to be ~350K, ~250K, ~220K for the film on STO, MgO and LAO substrates. The Tc modulation is easily understood and could be correlated with the phase boundary effect together with the distinguished strain state. First, the disordered phase boundaries could suppress the double exchange coupling in LSMO matrix, leading to decrease of Curie temperature [19]. Second, the biaxial distortion which is induced from substrate strain effect, will increase the Jahn-Teller splitting of the e_g electron levels and will cause decrease in Tc [140]. Here the relationship that Tc (LAO) <Tc (MgO) < Tc (STO) consistent well with the strain ϵ （LAO） > ϵ (MgO) > ϵ (STO), which is also consistent with previous report of pure LSMO films [91].

Figure 4. 5b gives the temperature dependent resistance behavior of the films. It can be observed that the films on STO, MgO and LAO show typical Metal insulating transition behavior with TMI of ~250K and ~200K, ~50K, respectively. which is correlated with the phase transition similar to the mechanism of CMR [19]. A small upturn at low temperature also exists for the sample on LAO substrate. This upturn portion of the resistivity is reported to be comply with the Coulomb blockade model: $\rho = \rho_0 \exp(\frac{T_0}{T})^{1/2}$, where T_0 depends on the tunneling barrier height. [43] The MR behavior measured under 1T are plotted in Figure 4. 5c. It is clear that each film has its specific MR peak, which couples with T_{MI}. The MR behavior around the T_{MI} can be understood similar as CMR. Here all the LSMO: CuO nanocomposite films comes up enhanced MR value than their pure LSMO counterpart grown under same condition, which could be ascribed to the phase

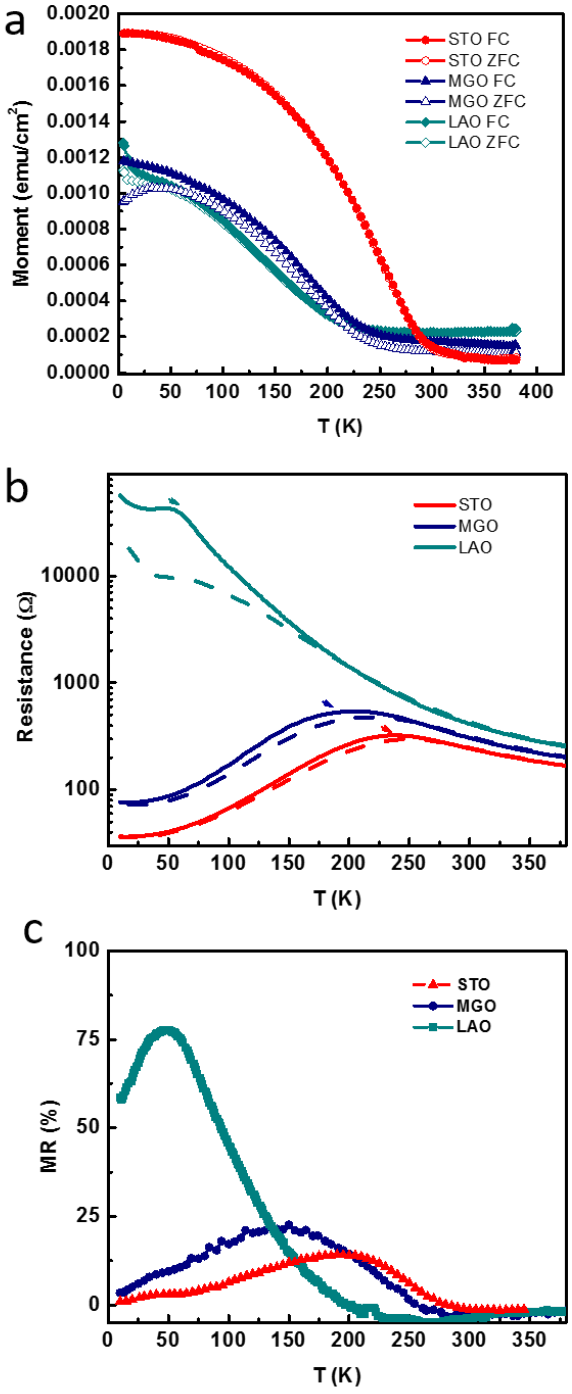

Figure 4. 5 Magnetic and transport properties of LSMO: CuO thin films on STO, MgO and LAO substrates. a) M-T, b) R-T and c) MR-T behavior under 1T.

boundary induced spin fluctuation [43]. Noted here, quite large MR values of ~80% are obtained in the film on LAO substrate, which imply that the large strain (over 2%) combined with the phase boundary effect in the films could result distinguishable MR behavior.

4.6 Summary

In summary, we explored the growth of the $(LSMO)_2$: $(CuO)_1$ nanocomposite thin films with various frequency and different selected substrates. Detail microstructure analysis with XRD and TEM indicate the films were grown as VAN structures with CuO pillars embedded in LSMO matrix. Systematical magnetic and transport properties tuning effect has been observed, correlated with the phase dimension and density. High MR value of 80% is achieved for the film on LAO substrate, indicating large strain combined with phase boundary effect as an efficient method for enhanced MR performance.

CHAPTER V

STRONG PERPENDICULAR EXCHANGE BIAS IN EPITAXIAL $LA_{0.7}SR_{0.3}MNO_3$: $LAFEO_3$ NANOCOMPOSITE THIN FILMS

5.1 Overview

Strong exchange bias (EB) in perpendicular direction has been demonstrated in vertically aligned nanocomposite (VAN) $(La_{0.7}Sr_{0.3}MnO_3)_{1-x}$: $(LaFeO_3)_x$ (LSMO:LFO, x=0.33, 0.5, 0.67) thin films deposited by pulsed laser deposition. Under a moderate magnetic field cooling, an EB field as high as ~800 Oe is achieved in the VAN film with x=0.33. Such enhanced EB effects can be attributed to the vertical FM-LSMO/AFM-LFO interface coupling associated with a disordered spin-glass status. The VAN design paves a powerful way for integrating perpendicular EB effect within thin films, providing a new dimension for advanced spintronic devices.

This chapter is reprinted with permission from "Strong perpendicular exchange bias in epitaxial $La_{0.7}Sr_{0.3}MnO_3$:$LaFeO_3$ nanocomposite thin films" by M. Fan, et al., APL Materials, 2016, 4, 076105.

5.2 Introduction

Exchange bias (EB), referring to a shift of the magnetization hysteresis loop along field axis, has gained great interest since its discovery in 1950s [45]. With the unidirectional magnetic anisotropy it provides, EB effect has found critical applications in numerous spintronic devices, i.e., magnetic recording read heads and magnetic memory [49,50]. The EB effect is believed to originate from the magnetic coupling across the ferromagnet (FM)/antiferromagnet (AFM) interface when cooled in magnetic field through the Neel temperature of the AFM [4647]. In addition to FM/AFM interfaces, this effect has also been extensively explored in FM/spin-glass (SG) [51,52,53], FM/Non-magnetic [54,55], FM/paramagnetic [50] interfaces recently. Most EB effects reported in thin films are based on multilayer structures where the magnetization of FM layer is pinned in the in-plane direction, which is parallel to the coupling interfaces. However, for next generation memories that require high thermal stability and high density, perpendicular EB (PEB) is more desirable [145,146]. So far, reported PEB in multilayer architectures can only be triggered in very thin FM films (less than 10 nm), found in layered noble metals Co/(Pd,Pt) [147], DyCo [145] and CoFeB-based spin valves [146], which all require precise heterostructure thickness control with sophisticated facilities, hampering the practical integration. Considering that the exchange bias originates mostly from the interface coupling, it is highly expected that PEB could be derived in structures with high density of coupling interfaces in the vertical direction.

Vertically aligned nanocomposite (VAN) thin films in which two phases of materials can be self-assembly grown epitaxially, provide a powerful way for vertical

interface coupling and microstructure tuning [21] and have been explored extensively for novel and enhanced functionalities[19,75,148,67]. Recently, by selecting FM $La_{0.7}Sr_{0.3}MnO_3$ (LSMO) and AFM $BiFeO_3$ as the two phases of VAN film, exchange bias in the perpendicular direction has been observed [74]. In addition, with careful design of the VAN thin film growth, high densities of interface can also be engineered to align to specific directions[149], making it promising for enhanced EB with controlled orientation. Enormous opportunity in exploring new VAN materials systems, performance tunability as well as the understanding of the fundamental EB mechanisms are left and lacking, worth investigation.

In this work, we investigated the co-growth of FM LSMO (a=3.87 Å, pseudo-cubic) and AFM $LaFeO_3$ (LFO, a=3.940 Å, pseudo-cubic) on $SrTiO_3$ (STO, a=3.905 Å) substrate to explore EB effect in the perpendicular direction. LFO is selected based on its good lattice matching with both STO and LSMO, and the large magnetic anisotropy [150]. Strong PEB phenomenon has been observed, and can be modulated by the strain tuning effect with composition variation. Detailed microstructure and magnetic properties analysis suggest that the exchange coupling at the vertical LSMO/LFO interfaces associated with a SG state are responsible for the pronounced PEB properties here.

5.3 Experimental

$(LSMO)_{1-x}$: $(LFO)_x$ nanocomposite films (with the film thickness of ~1000nm) with x=0.33, 0.5, 0.67, were grown on single crystalline STO (001) substrates by pulsed laser deposition. The composite targets were prepared with a conventional ceramic sintering process from high purity stoichiometric La_2O_3, $SrCO_3$, MnO_2 and Fe_2O_3

powders. During deposition, substrate temperature of 800 ℃ and oxygen pressure of 200 mTorr was maintained. A KrF excimer laser (λ=248nm) with a repetition rate of 10 Hz was used. All films were cooled at 10 ℃/min under 200 Torr O_2 after deposition. X-ray diffraction (XRD) (PANalytical Empyrean XRD) and transmission electron microscopy (TEM) (FEI Tecnai G2 F20 operated at 200 kV) were used to analyze the crystallinity and microstructure of the films.

The out-of-plane magnetizations of the films were measured by a commercial Physical Property Measurement System (PPMS Model 6000, Quantum Design) with Vibrating Sample Magnetometer (VSM). The temperature dependent magnetization (M-T) data was collected during the heating cycle, after cooling down the samples from 350K to 5K with (Field-cooling FC) or without (Zero-field-cooling ZFC) applied magnetic field. Hysteresis loops were obtained after cooling the sample from 300K under specific magnetic field down to the desired temperature.

5.4 Growth and microstructure of LSMO: LFO VAN films

Figure 5.1a shows XRD θ-2θ plots of the pure LSMO and LSMO: LFO nanocomposite films. Both LSMO and LFO phases grow highly textured along (00*l*) on STO substrate without any obvious impurity peak. To further investigate the crystal structure and the strain states of the composite films, reciprocal space mapping (RSM) were performed near the (113) STO peak. Figure 5.1c and Figure 5.1d show typical RSMs for $LSMO_{0.67}LFO_{0.33}$ and $LSMO_{0.33}LFO_{0.67}$. Clearly separated and systematically shifted LSMO (113) and LFO (113) peaks can be seen, indicating a strong strain tuning effect with the composition modulation. It can also be noticed that the LSMO and LFO peaks

spread little in the out-of-plane direction, suggesting small or no strain relaxation through the thickness of the film, consist with the general feature of VAN films that the strain status is dominated by the strain coupling between the two phases in the vertical direction rather than by the STO substrate[61,151,67,149]. The calculated out-of-plane lattice parameters of LSMO are plotted in Figure 5. 1b and summarized in table 1. The vertical strain state of LSMO was converted from compressive (-0.17%) for x=0 to tensile (+1.3%) for x=0.67, and LFO suffers from a compressive strain in the VAN films (-1.16% for x=0.33), suggesting strong strain coupling across the LSMO and LFO heterointerfaces.

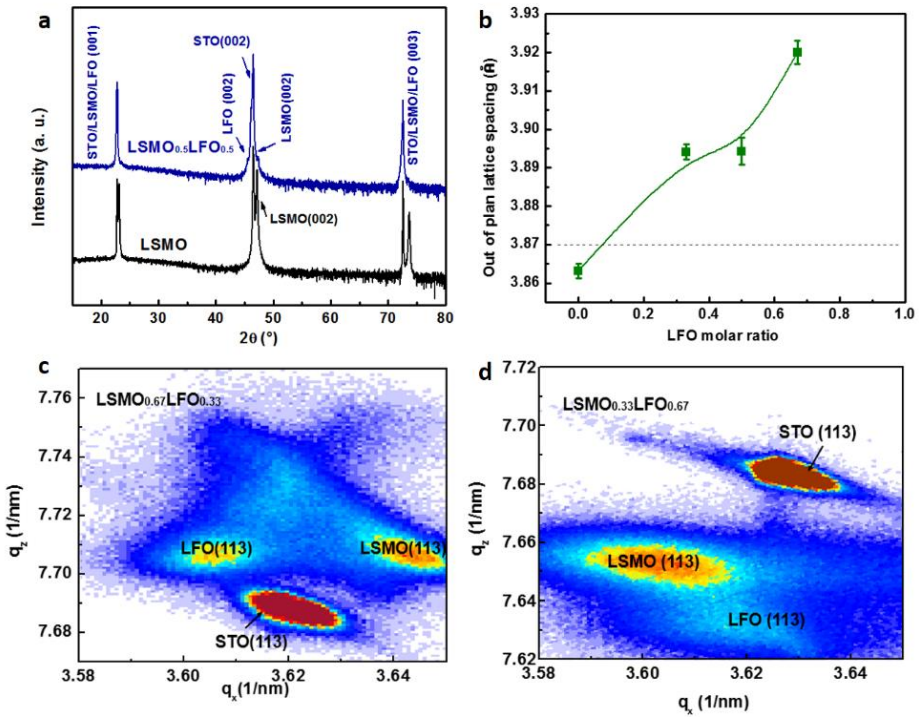

Figure 5. 1 a) XRD θ-2θ plots of pure LSMO and the $LSMO_{0.5}LFO_{0.5}$ nanocomposite films. b) Out-of-plane lattice parameter of LSMO with different LFO molar ratios. Reciprocal space maps near STO (113) of c) $LSMO_{0.67}LFO_{0.33}$ and d) $LSMO_{0.33}LFO_{0.67}$.

Table 5. 1 Lattice parameters and strain in LSMO and LSMO: LFO VAN films.

VAN sample	*lattice constant of LSMO [Å]* c_{LSMO}	*out-of-plane strain in LSMO [%]* $\frac{c_{LSMO} - c_{bulk\ LSMO}}{c_{bulk\ LSMO}}$	*Lattice constant of LFO [Å]* c_{LFO}	*out-of-plane strain in LFO [%]* $\frac{c_{LFO} - c_{bulk\ LFO}}{c_{bulk\ LFO}}$	*Out-of-plane Interfacial strain [%]* $\frac{c_{LFO} - c_{LSMO}}{c_{LSMO}}$
LSMO	3.86	-0.17	-	-	
$LSMO_{0.67}LFO_{0.33}$	3.893	+0.59	3.894	-1.16	0.025
$LSMO_{0.5}LFO_{0.5}$	3.895	+0.64	3.91	-0.76	0.38
$LSMO_{0.33}LFO_{0.67}$	3.9205	+1.3	3.93	-0.25	0.24

Detailed microstructure analysis was conducted via TEM and scanning transmission electron microscopy (STEM) for the composite films, as shown in Figure 5. 2. Figure 5. 2a displays a typical cross-section TEM image of the $LSMO_{0.67}LFO_{0.33}$ film, showing vertically self-assembled two phase growth with columnar structures on the substrate, further evidenced by the energy-dispersive X-ray spectroscopy (EDX) results (inset of Figure 5. 2a) taken under the STEM mode. The EDX line scan shows alternating Mn-rich and Fe-rich regions. High resolution TEM (Figure 5. 3) suggests exact one-to-one lattice matching between LSMO and LFO, consist with the small calculated lattice mismatch (1.7%) between them. Plan-view TEM image of $LSMO_{0.5}LFO_{0.5}$ (Figure 5. 2c) shows LFO phases embedded in the LSMO matrix, with domain diameter of 2-10 nm.

Figure 5. 2b, 2d, and inset of 2d are the TEM, STEM image and the selected area electron diffraction (SAED) pattern of $LSMO_{0.33}LFO_{0.67}$ film, respectively. The bright and dark columns in the STEM image correspond to the LFO (darker contrast) and LSMO (brighter contrast) phases. LFO domain diameter is determined to be less than 10nm also. Distinguished diffraction dots in the SAED pattern indicate high epitaxial quality of the composite film. Both LSMO and LFO grow cube-on-cube on STO substrate, with the lattice matching relations of $(002)_{LSMO}//(002)_{LFO}//(002)_{STO}$ and $(020)_{LSMO}//(020)_{LFO}//(020)_{STO}$.

5.5 Magnetic properties and exchange bias effect in LSMO: LFO VAN films

Magnetic properties of the films were analyzed using PPMS with VSM. After field cooling process starting from 300K, which is well below the Neel temperature of LFO (~740K)[152], obvious PEB effect was observed at 5K for all the $(LSMO)_{1-x}$: $(LFO)_x$ films, while pure LSMO film showing no obvious EB effect. Figure 5. 4a shows a typical magnetic hysteresis loop of the $LSMO_{0.67}LFO_{0.33}$ film at 5 K after field cooling under 1 T. It is obvious that the hysteresis loop shifted to the left along the magnetic field axis, which is opposite to the cooling field direction. The EB field H_{EB} and coercive field H_c are calculated using $H_{EB} = -(H_1 + H_2)/2$ and $H_c = |H_1 - H_2|/2$, where H_1 and H_2 are negative and positive fields at which the magnetization equals zero, respectively. A large EB field of ~690 Oe was derived, accompanied with a coercive field H_c of ~1600 Oe. A training effect has also been observed with the fifth scan of the hysteresis loop giving a H_{EB} of 545 Oe. Similar EB behavior also shows up with smaller magnitudes of H_{EB} for VAN films of x=0.5 and 0.67 (not shown here). Both the horizontal shift of the hysteresis

loop and the coercivity enhancement correspond to the characteristic features of the exchange bias [47,46], indicating robust exchange coupling at the vertical direction in the VAN systems. The EB phenomenon here is much stronger compared to reported LSMO based multilayers/nanostructures, which is typically less than 300Oe[153,154,155,156], and also comparable with (LSMO)1-x:($BiFeO_3$)x nanocomposite, in which a 1000Oe shift was observed for x=0.25 [74].

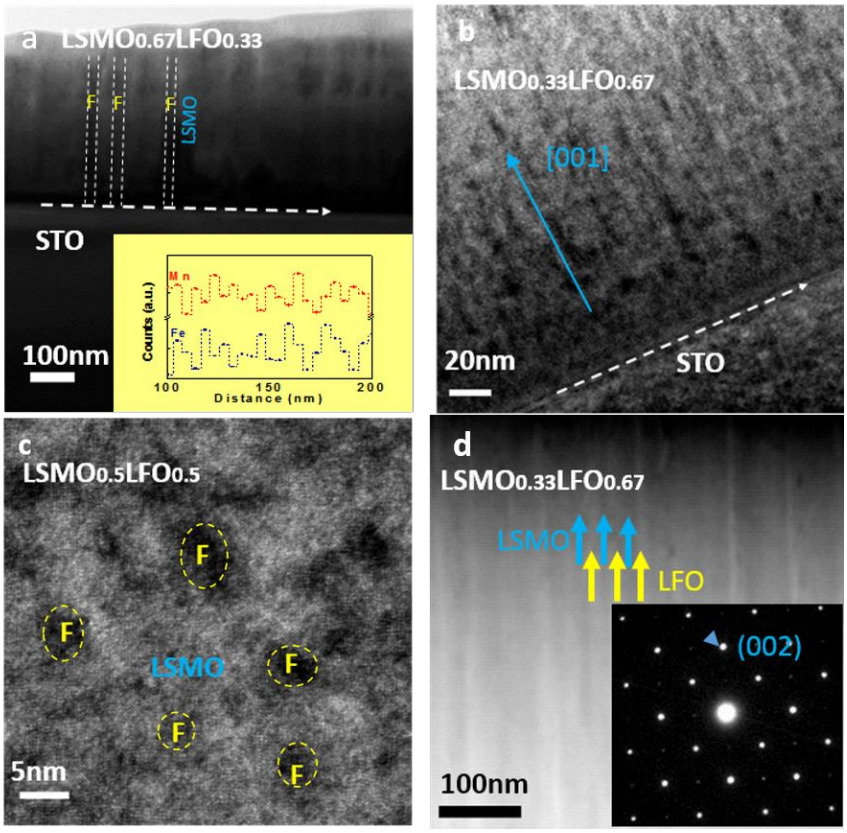

Figure 5. 2 Self-assembled vertically aligned nanostructures of $(LSMO)_{1-x}$: $(LFO)_x$ VAN films. a) Cross-sectional TEM image of the $LSMO_{0.67}LFO_{0.33}$ nanocomposite film. Inset of a) EDS line scan results across several pillars. b) Cross-sectional TEM image of $LSMO_{0.33}LFO_{0.67}$ VAN film. c) Plan-view TEM image of $LSMO_{0.5}LFO_{0.5}$ sample showing LFO nanopillars embedded in LSMO matrix. F indicates LFO. d) Cross-sectional STEM image and diffraction pattern (inset of d) of $LSMO_{0.33}LFO_{0.67}$.

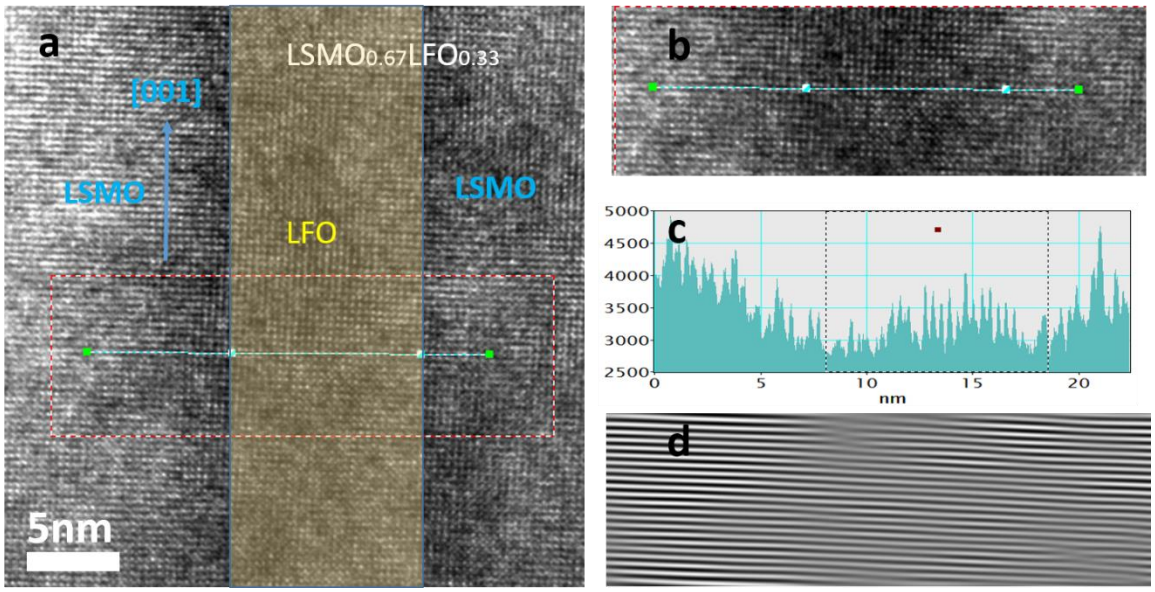

Figure 5. 3 a) High resolution TEM image of $LSMO_{0.67}LFO_{0.33}$, showing vertical aligned LSMO and LFO phases. b) Enlarged view of the area marked in a). c) The intensity profile along the line marked in b), indicating a LFO pillar width of ~11nm. d) FFT image of b), showing one-to-one lattice matching between LSMO and LFO.

To understand the PEB effect here, M-T behavior measured in 1000Oe of the films have been investigated and plotted in Figure 5. 4b. Systematic modulation can be seen: The magnetization of the nanocomposite films reduces in the entire temperature regime with increasing LFO concentration, consist with the FM LSMO volume ratio[157]. The ferromagnetic transition temperature is derived to be ~200K, ~150K and ~50K for x=0.33, 0.5 and 0.67, respectively, which can be linked to strain tuning and phase boundary effect in the VAN films: The spread of LSMO mosaic in the out-of-plane directions could impact on the Mn-O-Mn bond length and angle, thus affecting the exchange energy [139,108]. In addition, insulating AFM LFO embedded in LSMO matrix could serve as energy barriers among LSMO domains, suppressing the long-range double exchange interaction [19].

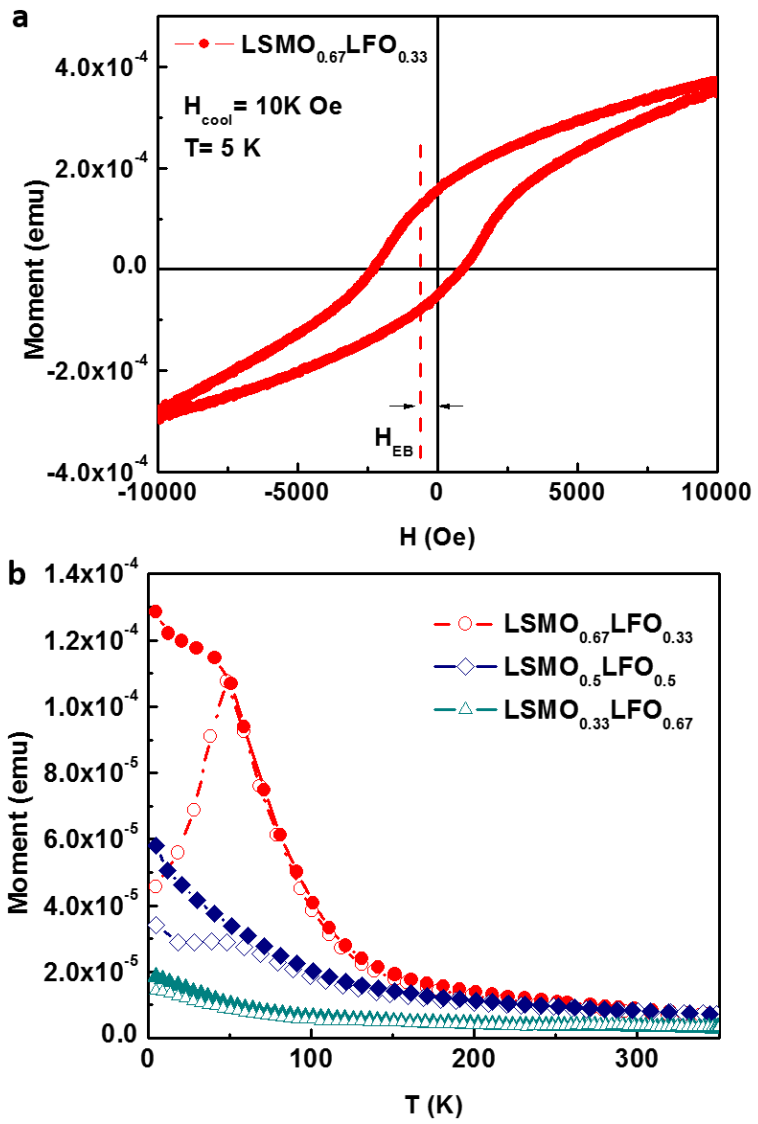

Figure 5. 4 a) Magnetization hysteresis curves of $LSMO_{0.67}LFO_{0.33}$ VAN film measured at 5 K after field cooling in +1 T, b) Field cooling and zero field cooling magnetization versus temperature plots for $(LSMO)_{1-x}(LFO)_x$ VAN films.

A peak at Tp in ZFC M-T curves and obvious bifurcation below Tirr behavior between the ZFC and FC curves were observed, the features mostly suggests a spin disordered/spin glass (SG) state [74,153,158], where Tp is close to Tirr[153], and different with superparamagnetic systems where the magnetization of FC increases monotonously with decreasing temperature[159,155]. The SG state can be linked to the competition of the FM double-exchange and AFM super-exchange couplings at the LSMO/LFO interfaces. Considering that the G-type AFM order in $LaFeO_3$ is not expected to pin the LSMO FM spins because of its fully compensated spin arrangement at the interfaces [154,160,161], we suggest that the EB behavior here might be correlated with the SG state, as discussed in previous reports with $La_{0.7}Sr_{0.3}MnO_3$:$SrMnO_3$[155], $La_{0.7}Sr_{0.3}MnO_3$:$LaSrMnO_4$[153] layered structures, etc. In the VAN films, after cooling under an applied magnetic field along the vertical direction, frozen FM spins can be induced at the SG interfaces, giving an additional torque on the LSMO FM spins, which the external field has to overcome when flipping. To further confirm the role of the frozen FM spins at the interfaces [162], the ZFC M-T curve at high magnetic field of 1T (shown in Figure 5. 5a) and temperature dependent H_{EB} (Figure 5. 5b) were investigated. For $LSMO_{0.67}LFO_{0.33}$, the H_{EB} decreases to 0 at ~20K, consist with the spin freezing temperature (Tf) estimated from the M-T curve.

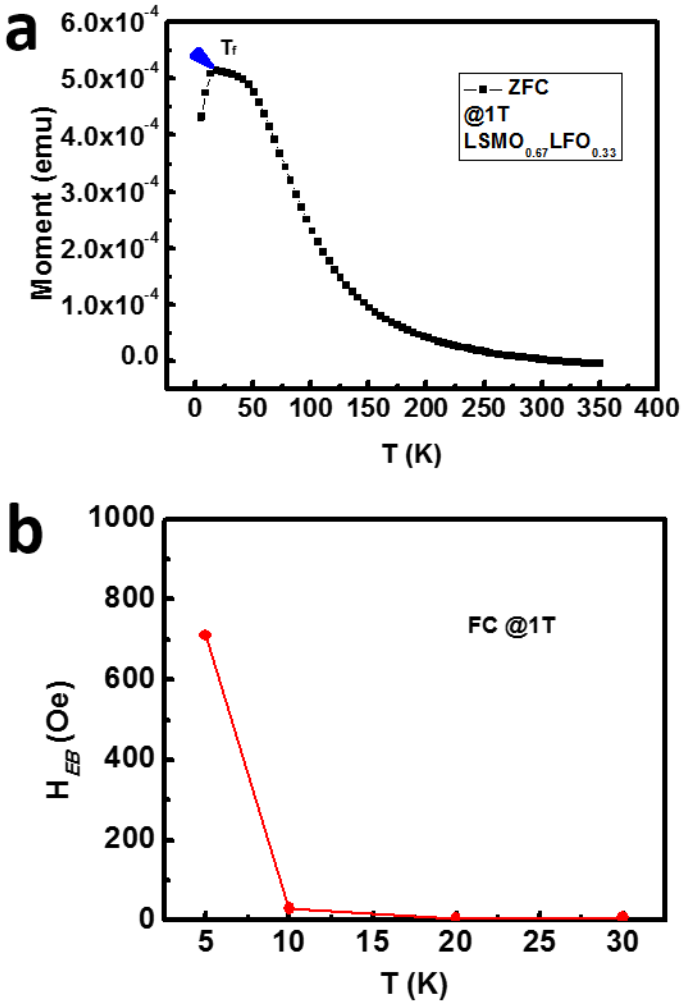

Figure 5. 5 a) ZFC M-T curve of $LSMO_{0.67}LFO_{0.33}$ b) Temperature dependent H_{EB} behavior of $LSMO_{0.67}LFO_{0.33}$ after cooling with 1T applied magnetic field.

The dependency of H_{EB} (4a) and H_c (4b) on cooling field (H_{cool}) gives further evidence supporting the role of the interfacial frozen spins associated with the SG in PEB. The data was collected after field cooling from 300K to 5K. The H_{EB} increases with increasing H_{cool} initially and then decreases gradually, and the H_c increases in the entire regime under investigation. This behavior normally occurs at FM/AFM interface

associated with disordered SG moments, which could be frozen at low temperatures [153,158,163,164], as reported in FM-AFM multilayer [163], cluster-glass compounds such as $La_{1-x}Sr_xCoO_3$ [165], Fe nanoparticles embedded in iron oxide matrix[164], etc. The initial increase of H_{EB} could be explained by increased exchange coupling resulted from the larger number of interfacial spins frozen in the field direction. The decrease of H_{EB} under high magnetic field may be correlated with the Zeeman coupling effect[154, 164], which can compete with interfacial exchange coupling.

Last, composition modulated PEB can be observed in Figure 5. 6, with H_{EB} (x=0.33) > H_{EB} (x=0.67) > H_{EB} (x=0.5) in the investigated region. This behavior might be linked with the strain states in the systems, because of the critical role of strain on determining the spin frustration [155,139,166]. The spin frustration at the interface can occur in both AFM and FM phases[155], thus depends on both the LSMO and LFO and their interfacial strain. Large strain in LSMO or LFO and small interfacial strain can lead to large spin frustration in the system [155,157,139,166]. Summarized in table.1, sample of x=0.33 and 0.67 exhibit stronger spin frustration than that of x=0.5, due to the large LFO strain of -1.16% and small interfacial strain of 0.025% for x=0.33 and large LSMO strain of 1.3% and 0.24% interfacial strain for x=0.67. While sample of x=0.5 has an interfacial strain of 0.38% and both LSMO and LFO phase has small strain (0.64% for LSMO and -0.76% for LFO). As is expected that systems with stronger disorder-induced frustration will support greater exchange bias[51,167], the strain induced spin disorder consist well with the observed experimental results qualitatively, i.e, H_{EB} (x=0.33) > H_{EB} (x=0.67) > H_{EB} (x=0.5). In addition, the larger LFO pillar size (~12nm) in $LSMO_{0.67}LFO_{0.33}$ might also

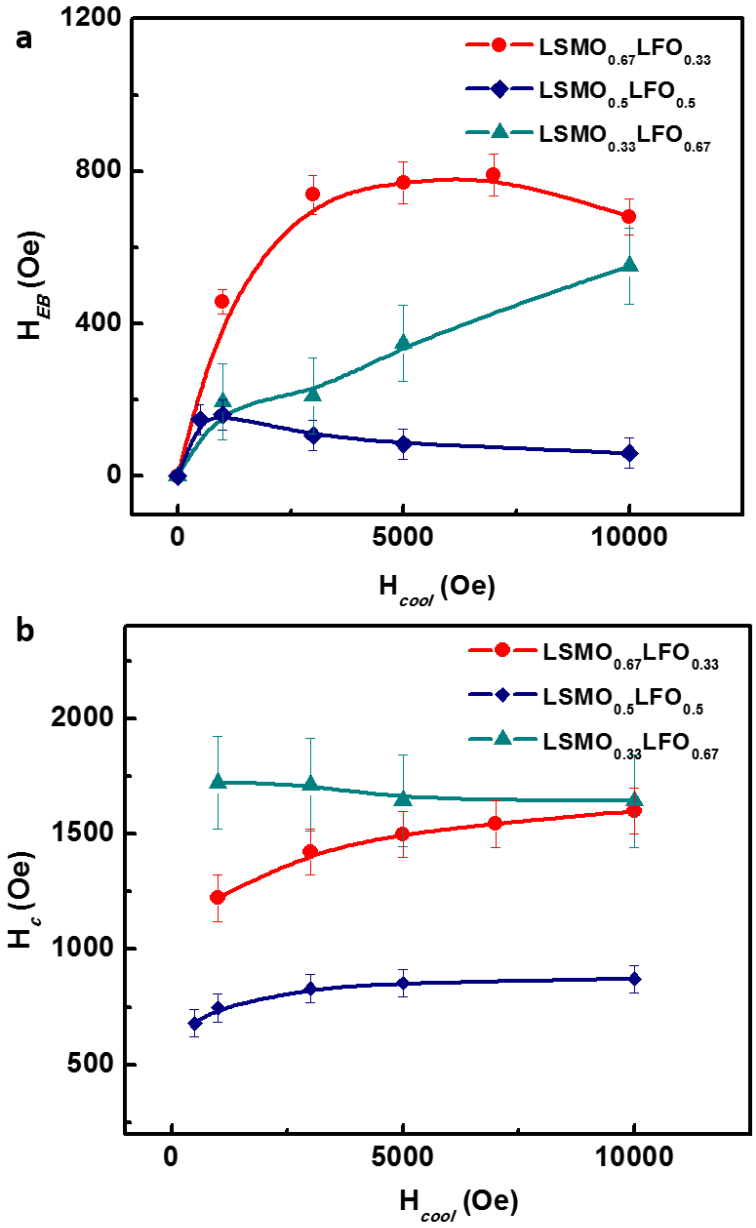

Figure 5. 6 Cooling field effect on the exchange bias behavior. a) H_{EB} and b) Hc of $(LSMO)_{1-x}$: $(LFO)_x$ VAN films as a function of the cooling field.

enhance the H_{EB}, as H_{EB} usually increases with t_{SG} initially and then saturates [168,51,53]. Future experiments are still needed to explore the depth-dependent magnetic profiles at the interface to get the idea of the real thickness of the disordered region.

5.6 Summary

Using unique vertically aligned nanocomposite structure design, we have demonstrated highly textured $(LSMO)_{1-x}$: $(LFO)_x$ films grown on STO substrates. By confining the FM/AFM hetero-interfaces in the vertical direction, significant exchange bias in the out-of-plane direction for micrometer-thick VAN films have been observed, which is promising for advanced spintronic devices application. Detailed microstructure and magnetic property analysis suggest that the disordered spin-glass states at the LSMO/LFO interfaces related to magnetic frustration is responsible for the EB effect, with the interfacial frozen spins giving an additional torque on the LSMO FM spins. Systematic property modulation can be achieved by strain tuning effect with composition control.

CHAPTER VI

SELF-ORGANIZED EPITAXIAL VERTICALLY ALIGNED NANOCOMPOSITES WITH LONG RANGE ORDERING ENABLED BY SUBSTRATE NANOTEMPLATING

6.1 Overview

Vertically aligned nanocomposites (VAN) thin films present as an intriguing material family for achieving novel functionalities. However, most of the VAN structures tend to grow in a random fashion, hindering the future integration in nanoscale devices. Previous efforts for achieving ordered nano-pillars structures have been focused on specific systems, and rely on sophisticated lithography and seeding techniques, making large area ordering quite difficult. In this work, we present a new technique to produce self-assembled nanocomposites with long range ordering through selective nucleation of nanocomposites on termination patterned substrates. Specifically, $SrTiO_3$ (001) substrates have been annealed to achieve alternating chemical terminations and thus enable selective epitaxy during the VAN growth. LSMO: CeO_2 nanocomposites, as a prototype, are demonstrated to form well-ordered rows in matrix structure, with CeO_2 (011) domains selectively grown on SrO terminated area, showing enhanced functionality. This approach provides a large degree of long range ordering for nanocomposite growth that could lead to unique functionalities and takes the nanocomposites one step closer towards future nanoscale device integration.

6.2 Introduction

Vertically aligned nanocomposites (VAN), in which two phases can grow epitaxially together on substrates, emerges recently as a new platform for enabling novel and enhanced functionalities as well as exploring fundamental physics [1,2,142,58,11]. Extensive efforts have been devoted in the past decade and demonstrated their fascinating capabilities in enabling interface-coupling and strain tuning phenomenon based on the high-quality, size-tunable, one phase pillars in matrix of other structures [1,2,22]. Major improvements have been made including enhanced flux pinning in superconductors[13], enhanced ferroelectricity[67], enabled multiferroic properties [11,12], tunable magnetoresistance [19], novel ionic transport[21] , perpendicular exchange bias [169],[170] and exotic optical properties [66], etc.

With the pioneering work in the field mostly focused on broadening possible materials systems and triggering novel properties[1,2], another timely demand for implementing VAN in future nanoscale devices is to achieve spatial ordering [2,112]. However most of the as-grown VAN films demonstrated up-to-date present very limited short range ordering and no long range ordering[2]. Since such in-plane ordering of the pillars could dramatically enrich the practical applications for the VAN films, several lithography and seeding techniques have been explored in achieving directed ordered growth, while with limited success [112,113,115,117]. Most of the demonstrations are on a specific system, i.e., $CoFe_2O_4$ (CFO)/$BiFeO_3$ (BFO). Using electron beam lithography (EBL) and ion milling, CFO seeds were formed from CFO thin film and patterned CFO pillars were achieved on the seed locations [114]. Another approach is to use hard masks of

e-beam lithography (EBL)-patterned gold or anodic aluminum oxide (AAO) together with lift-off process enabled CFO nuclei to guide the pillar growth [115]. Etch pits fabricated by focused ion beam (FIB) [112] and etched with mask of triblock terpolymer film [113] were used to seed the CFO growth recently, benefited from the difference in surface energy between CFO and the substrates. Similar seeding method has also been utilized in controlled growth of $Fe/LaSrFeO_4$ and $(Fe, Zn)_3O_4/BiFeO_3$ nano-dots arrays with nanoimprint lithography (NIL) [116,117]. Although these approaches achieved well-ordered structures, they all involve sophisticated seeding procedure employing EBL, FIB, NIL or complex etching/lift-off process, the ordered areas are limited in size and the scale-up could be challenging. At the same time, the pillar dimension and spacing can be restricted critically by the current lithography techniques. Furthermore, other VAN systems with spatial ordering are desired to be explored [2].

In this work, we present a self-organization approach for directing ordered VAN growth based on selective nucleation of two phases on chemical termination features produced on substrate surface by a simple thermal treatment. On $SrTiO_3$ (001) substrate surface, alternating SrO and TiO_2 termination strips can be formed under appropriate annealing. Taking advantage of such in-plane 1D ordered chemical termination nanopattern and the selective nucleation of the materials, well-ordered LSMO: CeO_2 nanocomposites with CeO_2 (011) pillars aligned in 1D in-plane (rectangular domains) within LSMO matrix have been achieved, over the entire substrate area. The physical properties of the achieved highly ordered VAN films have been investigated compared with the ones directly grown on raw substrates, demonstrating the power of such ordered

VAN structures. The cost-effective and simple process can be applied to different materials systems to induce 1D arrays in plane, providing great advance towards nanoscale devices and novel tunable functionality.

6.3 Growth approach illustration

The schematic diagram of the templating and growth procedure employed here is shown in **Figure 6. 1**. It is known that STO (001) has SrO-TiO_2-SrO stacking, and the as-received STO substrates have surface with quite small SrO and TiO_2 terminated regions randomly distributed, thus the bare STO could perform as a quasi-uniform surface shown in Figure 6. 1a [122]. VAN films directly grown on such substrates usually have random nucleation sites of the two phase materials and disordered pillars in matrix as shown in Figure 6. 1b. After a specific thermal treatment, the SrO terminating areas on the surface could coalesce to form a band along the step edges, and thus self-organized surface strips with alternating SrO and TiO_2 chemical terminations can be induced (Figure 6. 1c) [122,123]. Taking advantage of the termination dependent nucleation, such surfaces with alternating termination patterns could serve as template for directing phases' growth during the composite deposition (Figure 6. 1d). Different from the random growth on untreated substrate as in Figure 6. 1b, well-ordered pillars in matrix structure can be expected on such treated substrates (Figure 6. 1d).

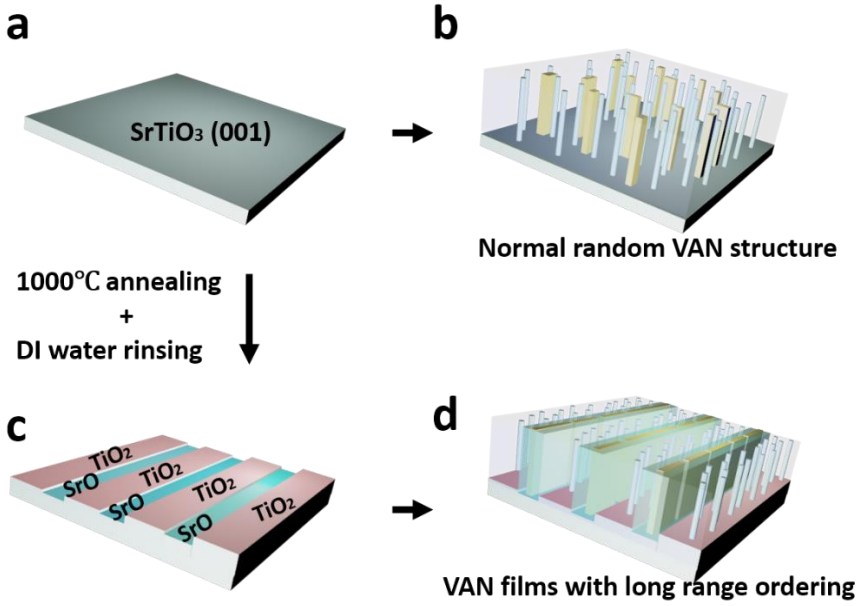

Figure 6. 1 Schematic diagram of the self-organized VAN film growth. a) As-received $SrTiO_3$ (001) substrate with random and uniform chemical termination, b) Microstructures of VAN film grown on as-received substrates, showing random location of pillars in matrix, c) Annealed $SrTiO_3$ (001) substrates, with alternating strip steps of SrO and TiO_2 termination region, d) expected microstructure of VAN film grown on templated substrate.

6.4 Experimental

The substrates were commercially available $SrTiO_3$ (001) single crystalline substrates (MTI Corporation). The substrates were then annealed at 1000 ˚C for 1h in air, followed by deionized (DI) water rinsing for 30s at room temperature. The surfaces of the substrates were characterized using atomic force microscope (AFM) (Bruker Dimension Icon AFM) under tapping and contact scan mode. During the measurement, the samples were kept in dark with a humility around 23% to reduce the possible background noise.

The $(LSMO)_{0.7}$: $(CeO_2)_{0.3}$ nanocomposite targets were prepared using a conventional solid state sintering process from high purity stoichiometric La_2O_3,

$SrCO_3$,MnO_2, and CeO_2 powders. Self-assembled epitaxial LSMO: CeO_2 thin film with thickness of ~120nm were deposited on as-received and thermal treated STO (001) substrates by pulsed laser deposition (PLD). During the deposition, substrate temperature was kept at 750 °C and a 200 mTorr oxygen pressure was maintained. KrF excimer laser (λ=248 nm) with a repetition rate of 1Hz was used. After deposition, all films were cooled at 10 ˚C/min under 200 Torr O_2.

The crystallinity and microstructures of the films were investigated by X-ray diffraction (XRD) (PANalytical Empyrean XRD), transmission electron microscopy (TEM) (FEI Tecnai G2 F20 operated at 200kV) and high resolution scanning transmission electron microscopy (STEM). The samples used for (S)TEM analysis were prepared by a standard manual grinding and thinning process followed by an ion milling procedure in a precision ion polishing system (PIPS 691, Gatan). Magnetotransport properties were examined using a Physical Property Measurement System (PPMS Model 6000, Quantum Design) in a four point probe configuration (in Van der Pauw geometry) with magnetic field applied out-of-plane. 100-nm-thick gold electrodes as the contacts were deposited with shadow mask by magnetron sputtering. The MR is evaluated by the following equation: MR (%) = $[(\rho_0-\rho_H)/\rho_0] \times 100\%$, where ρ_H, ρ_0 are the electrical resistivity with and without applied magnetic field, respectively. The in-plane magnetizations of the films were measured with Vibrating Sample Magnetometer (VSM) in the PPMS system.

6.5 Substrate nanotemplating evolution

Considering the chemical termination dependent nucleation, the VAN films above could come up with a well ordered structure that following the nano-patterns of the

substrates. The evolution of the surface structures of STO (001) with the thermal treatment was examined using atomic force microscopy (AFM) with tapping scan mode. Shown in **Figure 6.2a** is the typical topography of the as-received substrates. The surface is smooth with an average roughness of 0.133 nm. Section height profile (Figure 6.2c) measured along the marked line of Figure 6. 2a shows existence of terraces with one or 1/2 unit cell (~0.4nm, ~0.2nm) steps, while the steps are quite irregular and hard to distinguish, which indicates the random coexistence of TiO_2 and SrO terminations at the substrates. This result is consistent with previous work [171,126], and is normally resulted from the chemical-mechanical polishing process during the commercial fabrication. Figure 6. 2b shows the corresponding phase image with a line profile (Figure 6. 2d). The phase image gives no obvious large area contrast, probably due to the limitation of the lateral resolution of AFM and the small dimension of the random SrO or TiO_2 termination areas. After annealing in high temperature (1000℃) for 1h, the substrates come up with clear terraces with ordered and abrupt step edges, as shown in the surface topography image in Figure 6. 3a. It's noteworthy that there're trenches emerging along the step edges. Detailed section line profile (Figure 6. 3c) shows a height difference of 3/2 u.c. (~0.6nm) and 1/2 u.c. (~0.2nm) for the trench relative with the neighboring upper and lower-side terraces, respectively. Considering the atomic stacks in STO (001), it's correlated with different chemical terminations with half unit cell height difference[122]. The lateral width of the terraces and trenches can be determined to be ~180nm and 40nm, respectively. Considering the SrO termination is the minority part of the surface of untreated STO (001) crystals based on previous reports [126,172], the trenches should be with SrO termination and the terraces are

with TiO_2 termination. The corresponding phase image (Figure 6. 3b) also verified the above discussion showing distinguished contrast for the trenches and terraces. Figure 6. 3d displays the phase line profile, the obvious phase difference consists well with the topography image.

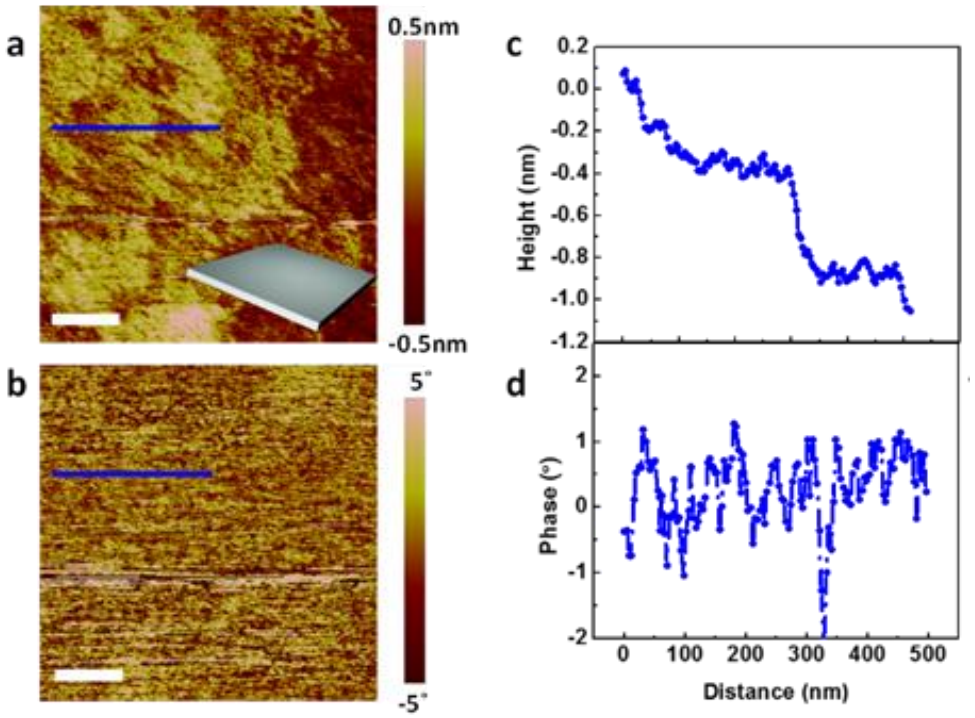

Figure 6. 2 Surface structures of as-received $SrTiO_3$ (001) substrates. AFM a) topographic and b) phase images of as-received $SrTiO_3$ (001) substrates. Corresponding line scan result of c) height and d) phase profiles indicated in a) and b) images. All scale bars corresponds to 200nm.

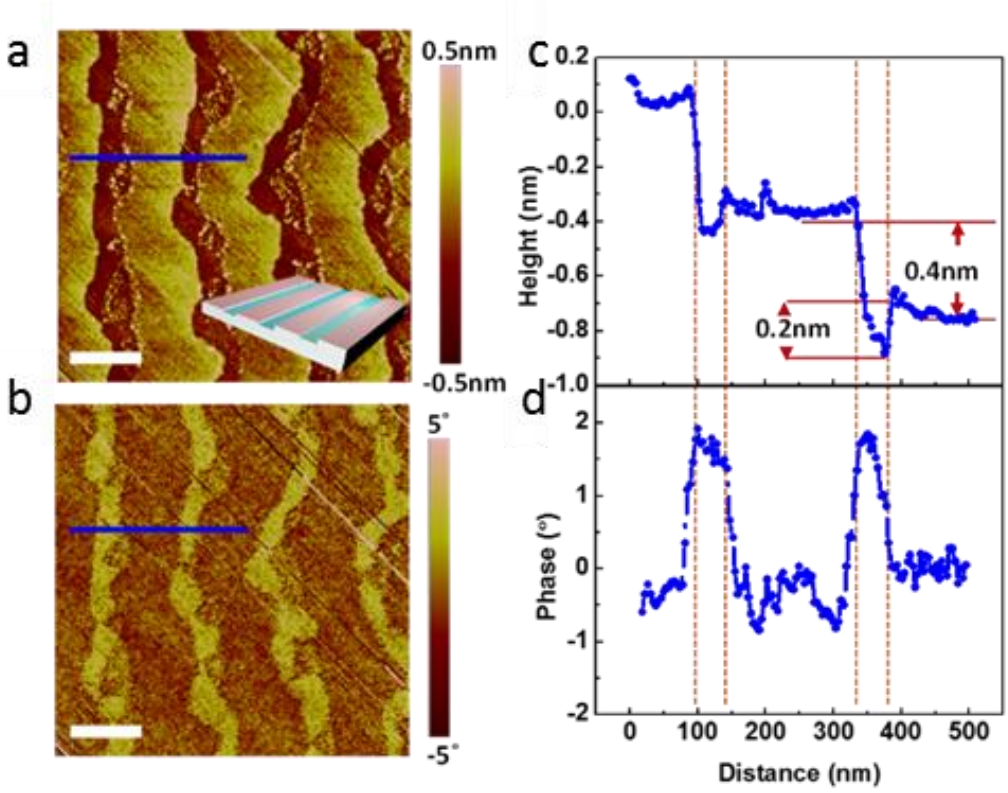

Figure 6. 3 Surface structures of templated $SrTiO_3$ (001) substrates. AFM a) topographic and b) phase images of thermal treated $SrTiO_3$ (001) substrates (1000℃, 1h in air and DI rinsing for 30s). Line scan profiles of c) height and d) phase marked in a) and b) images. Well-ordered nanopatterns can be observed in the treated substrates with alternating SrO and TiO_2 termination. All scale bars corresponds to 200nm.

AFM under contact mode was also employed to investigate the impact of the thermal treatment in templating substrates. The topography (**Figure 6. 4a**) and line scan (Figure 6. 4b) of the treated substrate indicate similar morphology of the surface, i.e, terraces and trenches with 3/2 u.c. and 1/2 u.c. difference in height as discussed above. The trace (Figure 6. 4c) and retrace (Figure 6. 4e) friction images evidence clear contrast between the terraces and the trenches, e.g., brighter contrast for trenches in the trace image. These results suggest alternating chemical termination features, in agreement with the tapping mode AFM phase images [173,174].

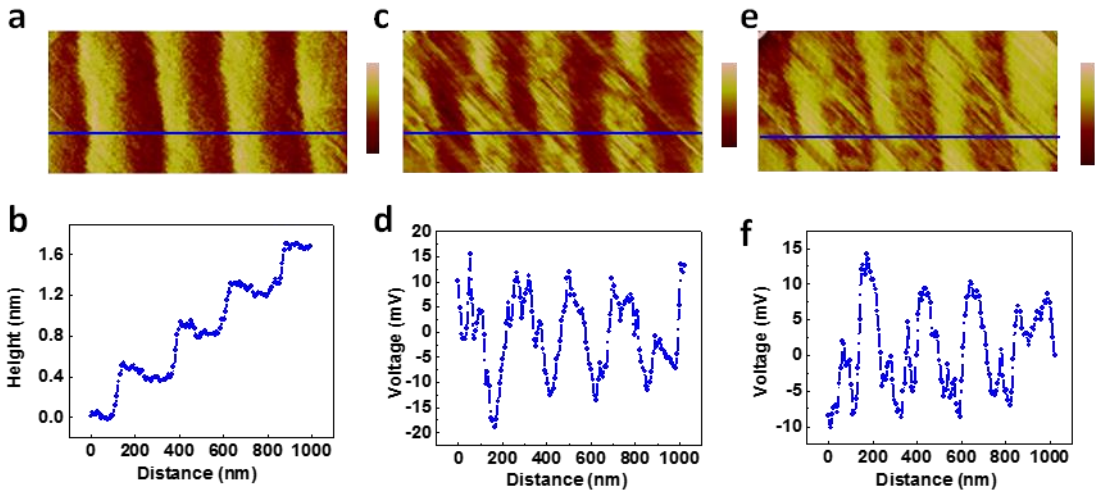

Figure 6. 4 a) AFM topography of thermal treated $SrTiO_3$ (001) substrate with line profile (b). Friction trace c) and e) retrace images of the substrate with corresponding line profile d) and f).

6.6 Self-assembly growth of LSMO: CeO_2 on templated substrate

To demonstrate the templated self-assembly growth of VAN nanocomposites on the tailored STO (001) surface, LSMO: CeO_2 has been chosen as a prototype considering the simple structure and good lattice match between LSMO and CeO_2 and the interesting magnetic and transport properties of the composites [19]. During the deposition, the laser frequency of 1Hz was used to favor low growth rate, ensuring the adatoms to diffuse to the most energy favorable nucleation center in the substrates. **Figure 6. 5** shows the typical plan-view transmission electron microscopy (TEM) images of the as-grown LSMO: CeO_2 films on as-received and termination patterned substrates. Circular CeO_2 domains embedded in LSMO matrix structures can be observed for both films grown on untreated and treated substrates. For the film on untreated STO substrates (Figure 6. 5a), random distribution of the circular CeO_2 pillars/domains without any obvious long range order has

been observed as expected, consistent with previous reports of VAN systems. Very differently, for the film on treated substrates which show ordered termination strips (Figure 6. 5b), the rectangular CeO_2 pillars are strongly confined and aligned in one-direction and formed ordered CeO_2 rows in LSMO matrix. Compared with the AFM results, which suggests minority termination surface is SrO termination, it can be concluded that the rectangular CeO_2 nanopillars are selectively grown following the pattern of SrO terminated surface areas. This remarkable selective nucleation of CeO_2 on SrO terminated and TiO_2 terminated regions could be correlated to the modulated surface energy for SrO termination and TiO_2 termination of STO (001) substrates. [175] As the alternating termination nanopattern comes up from the substrate miscut steps, in this demonstration, the unique long-range ordered VAN structure can be maintained for the whole substrate area, which is in the centimeter range for this case.

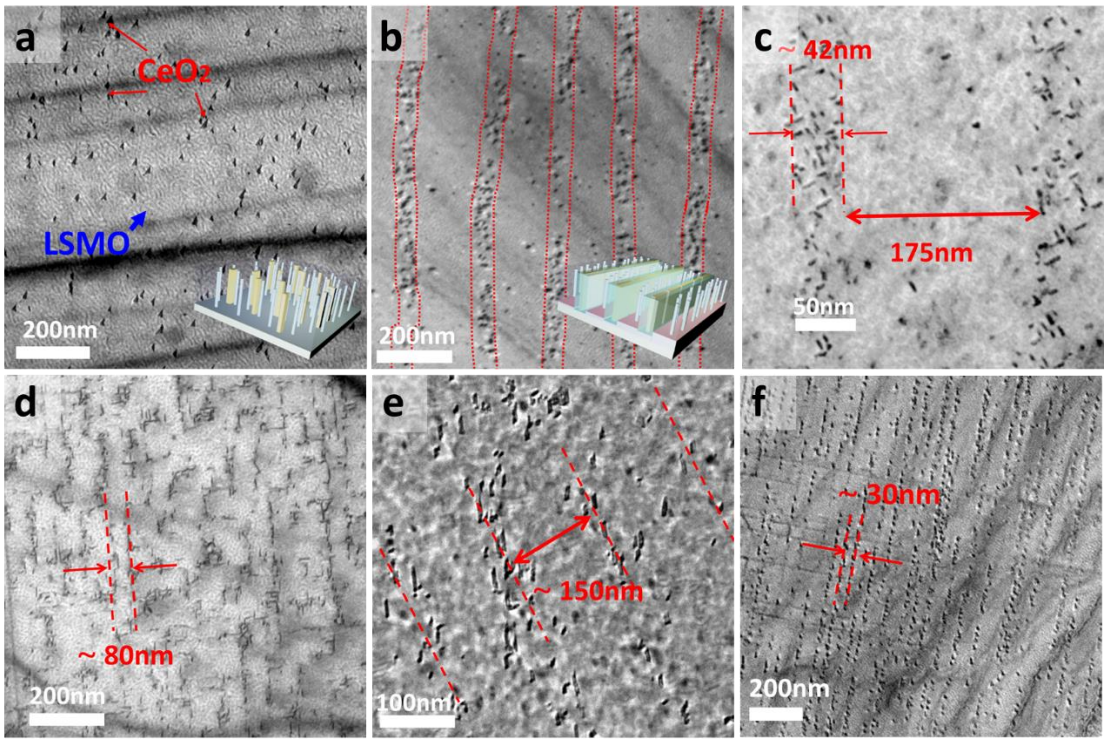

Figure 6. 5 Plan view TEM images of the LSMO: CeO_2 VAN films on templated and un-templated substrates. a) plan-view TEM image of LSMO: CeO_2 film on as-received STO substrate. b), c) plan-view TEM images of LSMO: CeO_2 film on thermal treated substrates, showing well ordered rectangular CeO_2 domain rows in LSMO matrix, with spacing of ~175nm. TEM image of LSMO:CeO_2 film on templated substrates with a miscut angle of d) ~0.38°, e) ~0.17° and f) ~1°, respectively.

Shown in Figure 6. 5b and Figure 6. 5c, it is clear that, the width of the rectangular CeO_2 rows (~42nm) and the spacing in between (~175nm), reproduce the dimension of SrO terminated trenches and TiO_2 terminated terraces on the substrate surface (Figure 6. 3a), respectively. Furthermore, the dimensions can be easily adjusted by the choice of the substrate with appropriate miscut angles. Figure 6. 5d and shows TEM image of the LSMO: CeO_2 film on a substrate with a miscut angle of ~ 0.38°, of which the AFM images are displayed in **Figure 6. 6**. The CeO_2 rows come up with a width of ~10-15nm and a

period of ~80nm, consistent well with the AFM results, where SrO trenches of ~20nm width and period of ~80nm can be derived (Figure 6. 6b). The row width is slightly smaller compared to the substrates SrO width, probably because of the so-called Ehrlich-Schwoebel (ES) barrier at the abrupt steps [176]. The lattice steps could serve as repulsive site for the CeO_2 nucleation due to the high vertical interfacial energy, similar as what was reported that on the vicinal single crystals of $LaAlO_3$ and $SrTiO_3$, CeO_2 and $Ce_{1-x}Gd_xO_{2-y}$ (CGO) nanoislands grown by chemical solution deposition were confined within the terraces [176]. Enhanced energy barrier at the surface steps due to the structural dissimilarity of the heterostructure might be the driving force. In this case, CeO_2 has been repulsed to nucleate at the edges. In addition, the limitation of the lateral resolution of AFM because of the tip radius of ~8nm might also account for such small difference between the CeO_2 rows width and the SrO band width in the AFM images. Figure 6. 5e and Figure 6. 5f display TEM images of LSMO: CeO_2 films grown on a substrate with miscut angle of ~0.17° (Figure 6. 5e) and ~1°, showing CeO_2 rows with ~150 nm and ~30nm period, respectively.

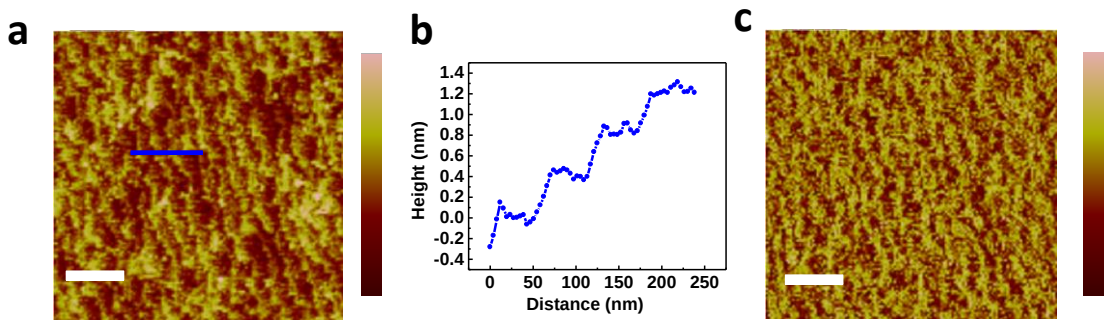

Figure 6. 6 AFM topography image of SrTiO3 (001) substrate with miscut angle of ~0.38˚ with corresponding b) line profile and c) phase image. Scale bar is 200nm.

To better understand the microstructures of such VAN films, high-resolution scanning transmission electron microscopy (STEM) and cross-section TEM imaging were conducted. **Figure 6. 7a** is the plan-view STEM image of the templated sample on treated STO substrate with miscut angle of ~1°. The corresponding low magnification STEM image inset shows clear rows of rectangular CeO_2 pillars. While apart from the obvious rectangular CeO_2 domains with long range ordering, it is interestingly noticed that some circular domains in the LSMO matrix background can be observed. Detailed analysis reveals that the CeO_2 exhibit different orientation as well as the pillar shape. Shown in Figure 6. 7b, the orientation of rectangular shape CeO_2 domains with higher contrast in TEM images can be determined to be (011) CeO2[100] ‖ (001)LSMO[100] ‖ (001)STO[100], while for the circular ones the orientation is (001)CeO_2 [110] ‖ (001)LSMO[100] ‖ (001)STO[100]. Similar orientation and shape selection of the oxide nanostructures has been reported in $Ce_{1-x}Gd_xO_{2-y}$ (CGO) on LAO (001) substrates[177], in which the modulation of the surface energy of the materials depends on growth

atmosphere and thus drives the selective growth. Here we show that the surface termination difference can provide distinguished nanoscale pattern for the selective growth of the VAN films. As previously reported, strain effects can also contribute to the different growth orientations. However considering that the treated substrates are the same single crystal lattice with only termination difference, the strain effects from two terminated surface areas should be comparable and thus we ascribe the selective nucleation and growth of the CeO_2 nanopillars to the different surface energy between SrO and TiO_2 terminated areas.

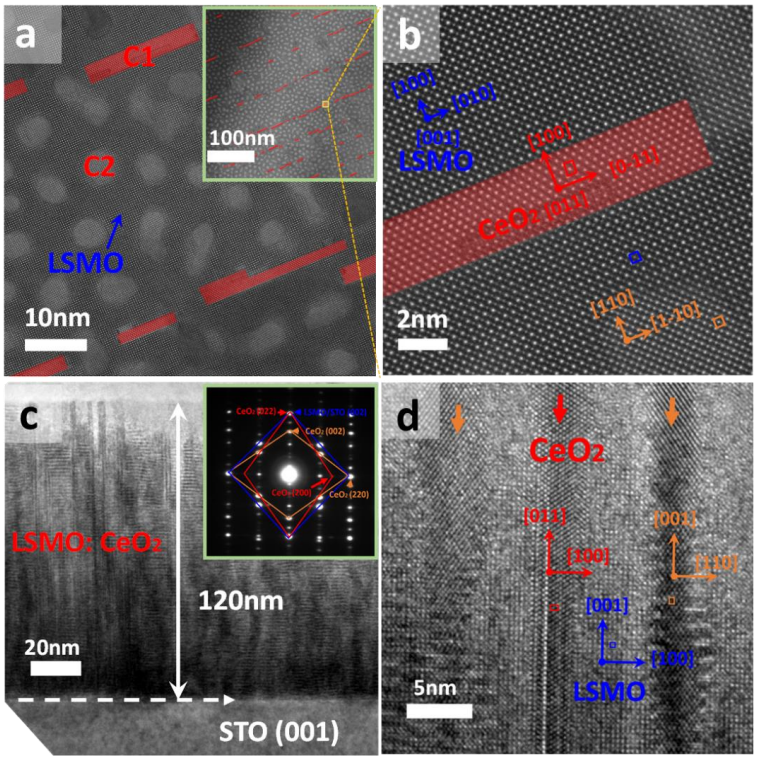

Figure 6. 7 Microstructure analysis of the templated films. a) High resolution STEM images of the LSMO: CeO_2 films grown on templated substrates with miscut angle of ~1˚. Inset of a) shows clear CeO_2 rows with long range ordering in the matrix. b) High resolution STEM displaying the orientation of the domain with different shapes. c) Cross-sectional TEM image and selective area electron diffraction pattern inset. d) High-resolution TEM image of templated LSMO: CeO_2 nanocomposite.

Cross-section TEM images shown in Figure 6. 7c display clear VAN columnar structures with both LSMO and CeO_2 directly grown from STO surface. Selected area electron diffraction (SAED) pattern (inset of Figure 6. 7c) indicate high quality epitaxial growth of both phases, in which two series dots for CeO_2 can be observed, i.e, dominated dots for CeO_2 (002) ‖ LSMO(002) ‖ STO(002) and CeO_2[220] ‖ LSMO[200] ‖ STO[200], and weak dots for CeO_2 (022) ‖ LSMO(002) ‖ STO(002) and CeO_2[200] ‖ LSMO[200] ‖ STO[200]. In high resolution TEM image of Figure 6. 7d, distinctly different atomic lattice fringes for both phases can be seen, as rectangular shaped lattice fringe corresponds to CeO_2 and square shaped fringes is LSMO. Pillars with two different orientations can be distinguished for CeO_2, consistent with the plan-view STEM results. The thickness is derived to be 120 nm. Both the STEM and TEM images suggest the successful demonstration of VAN structures with obvious long range ordering on the templated substrates.

6.7 Physical properties of the templated LSMO: CeO_2 VAN films

The physical properties between the templated and non-templated LSMO: CeO_2 nanocomposite films grown under the same conditions are compared. For all different sets of films examined, the films grown on templated substrates show obviously enhanced ferromagnetic properties. **Figure 6. 8a** shows the typical magnetic hysteresis loop (M-H) of the films measured at 10K. Much enhanced ferromagnetic properties can be seen for the templated film. The derived temperature dependent coercive field (Hc) and saturated magnetization (Ms) are plotted in Figure 6. 8b and Figure 6. 8c, respectively. It can be observed that the templated LSMO: CeO_2 films come up with enhanced ferromagnetic

properties in the entire temperature range investigated, i.e, ~50% larger Hc and ~20% stronger Ms than the non-templated films with random domain growth. **Figure 6. 9** gives measurements for another set of films, showing the reproducibility of the enhancements in different samples sets.

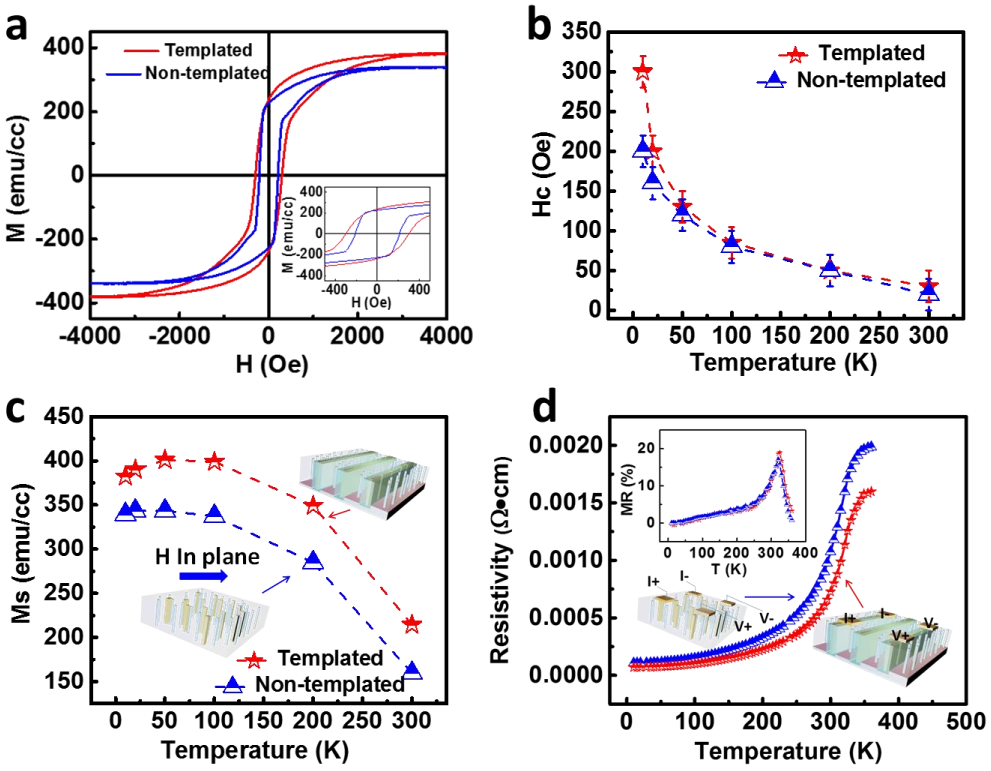

Figure 6. 8 Magnetic and transport properties of the LSMO: CeO_2 films on as-received and templated substrates: a) Magnetic hysteresis loops (M-H) measured at 10K. Temperature dependent b) Coercive filed (Hc) and c) Saturate magnetization (Ms). d) Temperature dependent Resistivity (ρ-T) and magnetoresistance (MR) measured with 1T (inset).

To understand such property enhancement, we examined pure LSMO films on templated and non-templated substrates, with magnetic hysteresis loops measured at 10K shown in **Figure 6. 9**. A coercive field of ~20Oe can be derived for the film on as-received substrate. The enhancement of Hc for LSMO: CeO_2 than that of pure LSMO can be

ascribed to the phase boundary effects, as reported previously [19,76].The insulating and non-magnetic CeO_2 domains can induce disordered phase boundaries, suppressing the double exchange interaction in the LSMO matrix, leading to enhancement of Hc. Interestingly it is noticed that the pure LSMO films on templated substrates also show an enhancement of the magnetic properties, however it is minor compared to the changes introduced by the long range ordered LSMO: CeO_2 films. Considering that both the films are grown at low-frequency of 1Hz, the films are all epitaxially grown with high quality, evidenced by the XRD Θ-2Θ scan (**Figure 6. 10**), e.g. no obvious difference can be observed for the LSMO peaks of the films in terms of non-templated or templated substrates. Here we attribute the unique property tuning effect to the long range ordering in the templated films. Considering the LSMO on SrO and TiO_2 terminations as two different domains, by growing film on striped terminated substrates, the A-site LSMO and B-site LSMO are well ordered separated, leading to enhanced exchange coupling inside the large LSMO domains, while the domain boundaries contribute to the Hc enhancement. The LSMO: CeO_2 films show more significant changes than pure LSMO films, indicating the well-ordered pillars in matrix structures help maintain strong exchange coupling within the LSMO domains and enlarge the Hc simultaneously.

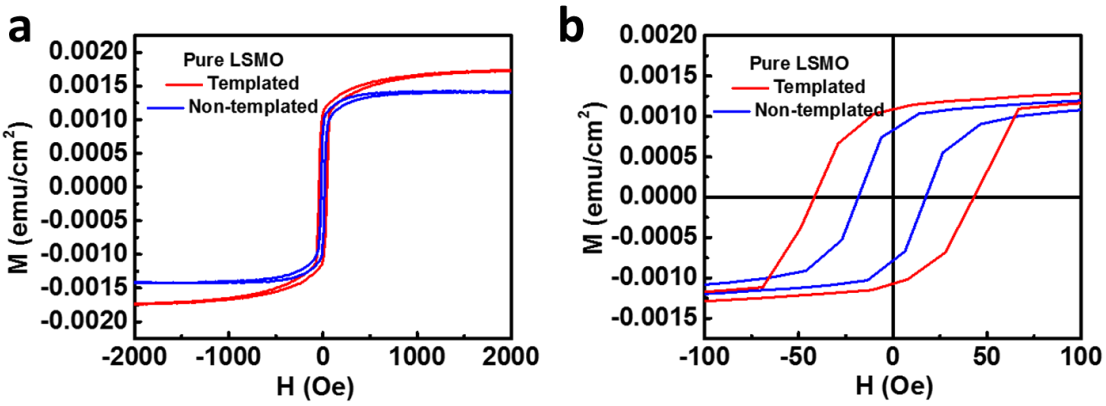

Figure 6. 9 Magnetic hysteresis loop for pure LSMO grown on templated and non-templated STO (001) substrates, measured at 10K.

Figure 6. 8d shows the temperature dependent resistivity (ρ-T) and magnetoresistance (MR) of the films. The ordered LSMO: CeO_2 film shows a slightly lower resistance compared to the random one, the magnetoresistance behavior is excellent for both films. The excellent MR behavior (above 10% in the range from 290K to 330K) together with smaller resistance and enhanced ferromagnetic properties make the well-ordered LSMO: CeO_2 film a great candidate for applications such as magnetic sensor as well as electrode materials for novel magnetic tunneling devices.

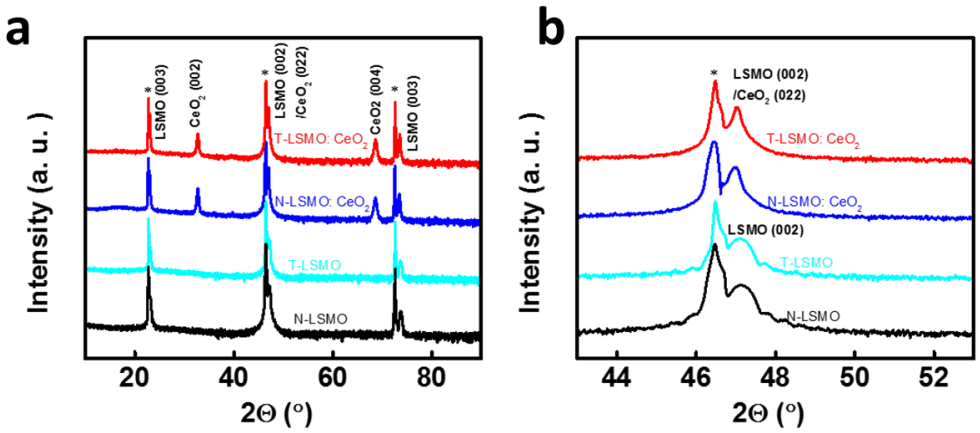

Figure 6. 10 a) XRD Θ-2Θ scan of pure LSMO and LSMO: CeO_2 nanocomposite film. b) Enlarged local XRD plots. N-LSMO and T-LSMO refers to pure LSMO films on non-templated and templated substrates, respectively. Same as N-LSMO: CeO_2 and T-LSMO: CeO_2. * corresponds to STO substrate peaks.

6.8 Summary

In conclusion, a novel method for fabricating VAN films with the long range spatial ordering has been demonstrated. Taking advantage of the chemical termination dependent nucleation of the materials, well-ordered (011) CeO_2 rectangular pillars -in-matrix structure has been achieved. LSMO: CeO_2, as a prototype, has been grown on thermal treated STO(001) substrates, which displays a nanopattern feature with alternating stripe of SrO and TiO_2 termination, and shows well aligned rows of CeO_2 rectangular pillars in LSMO matrix. Detailed analysis shows that the CeO_2 grown with different orientation on SrO ((011) out-of-plane) and TiO_2 ((001) out-of-plane) terminated areas, respectively. The spacing is easily adjustable by choosing substrates with different miscut angles. The templated LSMO: CeO_2 film exhibits excellent magnetic and transport properties. This unique and simple template growth process enables opportunities for achieving well-ordered VAN structures for a large selection of materials systems, which

could lead to a great advance in nanocomposite thin films and the new concept nanoscale devices.

CHAPTER VII

SUMMARY AND FUTURE WORK

In this dissertation, we have investigated the magnetic and transport property enhancement as well as novel functionalities demonstration in LSMO based materials for novel spintronic device applications, i.e, magnetic memories, sensors, etc. We explored the novel two phase VAN architecture to achieve the property tunability in the nanocomposite thin films. For low field magnetoresistance enhancement, we have incorporated insulating CeO_2 and semiconducting CuO as the secondary phases in the LSMO-Secondary phase VAN system. We investigated the property tuning in respect with concentration modulation, frequency adjustment as well as changing substrate. We achieved enhanced LFMR in a wide temperature range. With detailed microstructure and strain analysis, we investigated the impact of the secondary domain size, density, and the strain on the films property. We also demonstrated novel perpendicular exchange bias incorporating AFM $LaFeO_3$ as the secondary phase, and investigated the vertical FM/AFM heterointerface coupling in the system and the impact on the EB behavior. Finally, take advantage of susbstrate nanotemplating, we have successfully demonstrated a novel one-step self-assemble approach for growth of VAN structures with long range ordering, which will drastically rich the practical applications of the VAN films.

We have shown that VAN as a powerful platform with unique interface coupling can be used to explore enhanced/novel functionalities, i.e, LFMR and PEB in this dissertation. In addition, the growth of VAN structures with long range spatical ordering

is of significant importance for integration of the VAN films into novel nanoscale devices. Future research can be explored on the following aspects:

1) Fundamental growth mechanism. For example, the mechanism underline that could guide materials selection? i.e, whether VAN structures can be formed, and what determine the domain size and shape.
2) Design and fabricate new VAN systems with new and enhanced functionalities. As perpendicular exchange bias has been demonstrated in our case, leaving great opportunities in exploring new VAN materials systems, investigating performance tunability and understanding the fundamental EB mechanisms.
3) Exploring capability of substrate nanotemplating in growing ordered structures for other VAN systems, understanding the mechanism for selective growth to shadow on materials selection.
4) Integrate the VAN materials into nanoscale devices. For example, incorporate the PEB system as the electrode for magnetic or multiferroic tunneling junctions.

REFERENCES

1. MacManus-Driscoll, J. L., Suwardi, A. & Wang, H. Composite epitaxial thin films: A new platform for tuning, probing, and exploiting mesoscale oxides. *MRS Bull.* **40,** 933–942 (2015).
2. Zhang, W., Ramesh, R., MacManus-Driscoll, J. L. & Wang, H. Multifunctional, self-assembled oxide nanocomposite thin films and devices. *MRS Bull.* **40,** 736–745 (2015).
3. Ngai, J. H., Walker, F. J. & Ahn, C. H. Correlated Oxide Physics and Electronics. *Annu. Rev. Mater. Res.* **44,** 1–17 (2014).
4. Ramanathan, S. Thin film metal-oxides. *Harvard University: Springer New York Dordrecht* (2010).
5. Yang, Z., Ko, C. & Ramanathan, S. Oxide Electronics Utilizing Ultrafast Metal-Insulator Transitions. *Annu. Rev. Mater. Res.* **41,** 337–367 (2011).
6. Zhang, J. & Averitt, R. D. Dynamics and Control in Complex Transition Metal Oxides. *Annu. Rev. Mater. Res.* **44,** 19–43 (2014).
7. Nomura, K. Ohta, H, Takagi, A, Kamiya, T., Hirano, M., & Hosono, H Room-temperature fabrication of transparent flexible thin-film transistors using amorphous oxide semiconductors. *Nature* **432,** 488–492 (2004).
8. Kim, M.-G., Kanatzidis, M. G., Facchetti, A. & Marks, T. J. Low-temperature fabrication of high-performance metal oxide thin-film electronics via combustion processing. *Nat. Mater.* **10,** 382–388 (2011).
9. Wang, J., Neaton, J B., Zheng, H., Nagarajan, V. & Ramesh, R Epitaxial $BiFeO_3$

multiferroic thin film heterostructures. *Science* **299,** 1719–1722 (2003).

10. Seo, S., Lee, M. J., Seo, D. H., Jeoung, E. J. & Park, B. H. *et al.* Reproducible resistance switching in polycrystalline NiO films. *Appl. Phys. Lett.* **85,** 5655–5657 (2004).
11. Zhang, W., Jian, J., Chen, A., Jiao, L. & Wang, H. Strain relaxation and enhanced perpendicular magnetic anisotropy in $BiFeO_3$:$CoFe_2O_4$ vertically aligned nanocomposite thin films. *Appl. Phys. Lett.* **104,** 62402 (2014).
12. Aimon, N. M., Kim, D. H., Sun, X. & Ross, C. A. Multiferroic behavior of templated $BiFeO_3$:$CoFe_2O_4$ self-assembled nanocomposites. *ACS Appl. Mater. Interfaces* **7,** 2263–2268 (2015).
13. Huang, J., Fan, M., Wang, H., Chen, L. & Wang, H. Enhanced superconducting properties of $YBa_2Cu_3O_{7-\delta}$ thin film with magnetic nanolayer additions. *Ceram. Int.* **42,** 12202–12209 (2016).
14. Mott, N. F. & Friedman, L. Metal-insulator transitions in VO_2, Ti_2O_3 and $Ti_{2-x}V_xO_3$. *Philos. Mag.* **30,** 389–402 (1974).
15. Jian, J., Zhang, W., Jacob, C., Chen, A., & Wang, H. Roles of grain boundaries on the semiconductor to metal phase transition of VO_2 thin films. *Appl. Phys. Lett.* **107,** 102105 (2015).
16. Dong, R., Lee, D. S., Xiang, W. F., Oh, S. J. & Hwang, H. Reproducible hysteresis and resistive switching in metal-CuxO-metal heterostructures. *Appl. Phys. Lett.* **90,** 42107 (2007).
17. Sawa, A. Resistive switching in transition metal oxides. *Materials Today* **11,** 28–

36 (2008).

18. Parkin, S. S. P., Kaiser, C., Panchula, A., Rice, P. M. & Yang, S. H. Giant tunnelling magnetoresistance at room temperature with MgO (100) tunnel barriers. *Nat. Mater.* **3,** 862–867 (2004).

19. Fan, M., Zhang, W., Khatkhatay, F., Li, L. & Wang, H. Enhanced tunable magnetoresistance properties over a wide temperature range in epitaxial $(La_{0.7}Sr_{0.3}MnO_3)_{1-x}$:$(CeO_2)_x$ nanocomposites. *J. Appl. Phys.* **118,** 065302 (2015).

20. Urushibara, A., Moritomo, Y., Arima, T., Asamitsu, A. & Tokura, Y. Insulator-metal transition and giant magnetoresistance in $La_{1-x}Sr_xMnO_3$. *Phys. Rev. B* **51,** 14103–14109 (1995).

21. Cho, S., Yun, C., Tappertzhofen, S., Kursumovic, A. & MacManus-Driscoll, J. L. Self-assembled oxide films with tailored nanoscale ionic and electronic channels for controlled resistive switching. *Nat. Commun.* **7,** 12373 (2016).

22. Chen, A. & Jia, Q. Multiferroic Nanocomposite Thin Films. *Taylor Fr. Gr.* 189–213 (2016).

23. Zhang W. Enhanced functionalities achieved by a vertically aligned nanocomposite approach. *Texas A&M.* (2015).

24. Martin, L. W., Chu, Y. H. & Ramesh, R. Advances in the growth and characterization of magnetic, ferroelectric, and multiferroic oxide thin films. *Mater. Sci. Eng. R Reports* **68,** 89–133 (2010).

25. Von Helmolt, R., Wecker, J., Holzapfel, B., Schultz, L. & Samwer, K. Giant negative magnetoresistance in perovskitelike $La_{2/3}Ba_{1/3}MnO_x$ ferromagnetic films.

Phys. Rev. Lett. **71,** 2331–2333 (1993).

26. Moshnyaga, V., Damaschke, B., Shapoval, O., Belenchuk, A. & Samwer, K. Structural phase transition at the percolation threshold in epitaxial $(La_{0.7}Ca_{0.3}MnO_3)_{1-x}$:$(MgO)_x$ nanocomposite films. *Nat. Mater*. **2,** 247–252 (2003).

27. Miltat, J. E. & Donahue, M. J. Handbook of Magnetism and Advanced Magnetic Materials. *Weley* (2007). doi:10.1002/9780470022184

28. Hwang, H. Y., Cheong, S. W., Radaelli, P. G., Marezio, M. & Batlogg, B. Lattice effects on the magnetoresistance in doped $LaMnO_3$. *Phys. Rev. Lett.* **75,** 914–917 (1995).

29. Bowen, M., Bibes, M., Barthélémy, A., Contour, J. P. & Fert, A. Nearly total spin polarization in $La_{2/3}Sr_{1/3}MnO_3$ from tunneling experiments. *Appl. Phys. Lett.* **82,** 233–235 (2003).

30. Green, M. A., Ho-Baillie, A. & Snaith, H. J. The emergence of perovskite solar cells. *Nat. Photonics* **8,** 506–514 (2014).

31. Montini, T., Melchionna, M., Monai, M. & Fornasiero, P. Fundamentals and Catalytic Applications of CeO_2-Based Materials. *Chemical Reviews* **116,** 5987–6041 (2016).

32. Material Properties and Defect Chemistry of Ceria. 1–7 (2010). at <https://courses.physics.illinois.edu/phys466/sp2013/projects/2010/Oaks/html/node3.html>

33. Cupric oxide (CuO) property: crystal structure, lattice parameters-Group III Condensed Matter, *Springer* **6833,** 90–92 (2015)

34. Siemons, W., Koster, G., Blank, D., Hammond, R. H. & Beasley, M. R. Tetragonal CuO: End member of the 3d transition metal monoxides. *Phys. Rev. B - Condens. Matter Mater. Phys.* **79,** 1–7 (2009).

35. Bibes, M. Nanoferronics is a winning combination. *Nat. Mater.* **11,** 354–357 (2012).

36. Current, N. E. Giant Magnetoresistance Sensors : A Review on Structures and Non-Destructive Eddy Current Testing Applications. *Sensors* **16,** 298(1-30) (2016).

37. Jonker, G. H. & Van Santen, J. H. Ferromagnetic compounds of manganese with perovskite structure. *Physica* **16,** 337–349 (1950).

38. Siwach, P. K., Singh, H. & Srivastava, O. N. Low field magnetotransport in manganites. *J. Phys. Condens. Matter* **20,** 273201 (2008).

39. Electron doped manganites. 3–4 (2017). At: <http://www2.cpfs.mpg.de/~wirth/rec/mang1.html>

40. Rybchenko, S. I., Fujishiro, Y., Takagi, H. & Awano, M. Effect of grain boundaries on the magnetoresistance of magnetite. *Phys. Rev. B - Condens. Matter Mater. Phys.* **72,** (2005).

41. Gupta, A., Gong, G Q, Xiao, G., Duncombe, P R. & Sun, J Z. Grain-boundary effects on the magnetoresistance properties of perovskite manganite films. *Phys. Rev. B* **54,** R15629–R15632 (1996).

42. Mathur, N. D., Burnell, G., Isaac, S. P., Jackson, T. J. & Blamire, M. G. Large low-field magnetoresistance in $La_{0.7}Ca_{0.3}MnO_3$ induced by artificial grain boundaries. *Nature* **387,** 266–268 (1997).

43. Ning, X., Wang, Z. & Zhang, Z. Large, Temperature-Tunable Low-Field Magnetoresistance in $La_{0.7}Sr_{0.3}MnO_3$:NiO Nanocomposite Films Modulated by Microstructures. *Adv. Funct. Mater.* **24,** 5393–5401 (2014).

44. Kang, B. S., Wang, H., MacManus-Driscoll, J L, Li, Y. & Betts, J B Low field magnetotransport properties of $(La_{0.7}Sr_{0.3}MnO_3)_{0.5}$:$(ZnO)_{0.5}$ nanocomposite films. *Appl. Phys. Lett.* **88,** 192514 (2006).

45. Meiklejohn, W. H. & Bean, C. P. New Magnetic Anisotropy. *Phys. Rev.* **102,** 1413 (1956).

46. Kiwi, M. Exchange bias theory. *J. Magn. Magn. Mater.* **234,** 584–595 (2001).

47. Nogués, J., Sort, J., Langlais, V., Skumryev, V. & Baró, M.D. Exchange bias in nanostructures. *Phys. Rep.* **422,** 65–117 (2005).

48. Koval, V., Viola, G. & Tan, Y. Biasing Effects in Ferroic Materials. *Intech* 205–245 (2015).

49. Nogués, J. & Schuller, I. K. Exchange bias. *J. Magn. Magn. Mater.* **192,** 203–232 (1999).

50. Gibert, M., Zubko, P., Scherwitzl, R., Íñiguez, J. & Triscone, J.-M. Exchange bias in $LaNiO_3$–$LaMnO_3$ superlattices. *Nat. Mater.* **11,** 195–198 (2012).

51. Ali, M., Adie, P., Marrows, C. H., Greig, D. & Stamps, R. L. Exchange bias using a spin glass. *Exch. Organ. Behav. Teach. J.* **6,** 2–7 (2007).

52. Yuan, F. Te, Lin, J. K., Yao, Y. D. & Lee, S. F. Exchange bias in spin glass (FeAu)/NiFe thin films. *Appl. Phys. Lett.* **96,** 18–21 (2010).

53. Usadel, K. D. & Nowak, U. Exchange bias for a ferromagnetic film coupled to a

spin glass. *Phys. Rev. B - Condens. Matter Mater. Phys.* **80,** 1–5 (2009).

54. Fan, Y., Smith, K. J., Lüpke, G., Hanbicki, T. & Jonker, B. T. Exchange bias of the interface spin system at the Fe/MgO interface. *Nat. Nanotechnol.* **8,** 438–44 (2013).

55. Zhu, S. J., Yuan, J., Zhu, B. Y., Zhang, F. C. & Zhang, P. X. Exchange bias effect and enhanced magnetoresistance in $La_{0.67}Sr_{0.33}MnO_3$/$SrTiO_3$ superlattices. *Appl. Phys. Lett.* **90,** 112502 (2007).

56. Salonitis, K., Pandremenos, J., Paralikas, J. & Chryssolouris, G. Multifunctional materials: Engineering applications and processing challenges. *Int. J. Adv. Manuf. Technol.* **49,** 803–826 (2010).

57. Ma, J., Hu, J., Li, Z. & Nan, C. W. Recent progress in multiferroic magnetoelectric composites: From bulk to thin films. *Adv. Mater.* **23,** 1062–1087 (2011).

58. MacManus-Driscoll, J. L., Zerrer, P., Wang, H., Yang, H. & Jia, Q. Strain control and spontaneous phase ordering in vertical nanocomposite heteroepitaxial thin films. *Nat. Mater.* **7,** 314–20 (2008).

59. Lebedev, O., Verbeeck, J., Van Tendeloo, G., Shapoval, O. & Samwer, K. Structural phase transitions and stress accommodation in $(La_{0.67}Ca_{0.33}MnO_3)1$-x:(MgO)x composite films. *Phys. Rev. B* **66,** 1–10 (2002).

60. Zheng, H., Wang, J., Lofland, S. E., Ma, Z. & Ramesh, R. Multiferroic $BaTiO_3$-$CoFe_2O_4$ Nanostructures. *Science* **303,** 661–663 (2004).

61. Zhang, W., Chen, A., Bi, Z., Jia, Q. & Wang, H. Interfacial coupling in heteroepitaxial vertically aligned nanocomposite thin films: From lateral to vertical control. *Curr. Opin. Solid State Mater. Sci.* **18,** 6–18 (2014).

62. Chen, A., Bi, Z., Jia, Q., Macmanus-Driscoll, J. L. & Wang, H. Microstructure, vertical strain control and tunable functionalities in self-assembled, vertically aligned nanocomposite thin films. *Acta Mater.* **61,** 2783–2792 (2013).

63. Su, Q., Yoon, D., Chen, A., Khatkhatay, F. & Wang, H. Vertically aligned nanocomposite electrolytes with superior out-of-plane ionic conductivity for solid oxide fuel cells. *J. Power Sources* **242,** 455–463 (2013).

64. Mohaddes-Ardabili, L., Zheng, H., Ogale, S. B., Hannoyer, B. & Ramesh, R. Self-assembled single-crystal ferromagnetic iron nanowires formed by decomposition. *Nat. Mater.* **3,** 533–538 (2004).

65. Su, Q., Zhang, W., Lu, P., Fang, S. & Wang, H. Self-Assembled Magnetic Metallic Nanopillars in Ceramic Matrix with Anisotropic Magnetic and Electrical Transport Properties. *ACS Appl. Mater. Interfaces* **8,** 20283–20291 (2016).

66. Li, L., Sun, L., Gomez-Diaz, J., Hogan, N. L. & Wang, H. Self-Assembled Epitaxial Au–Oxide Vertically Aligned Nanocomposites for Nanoscale Metamaterials. *Nano Lett.* **16,** 3936–3943 (2016).

67. Harrington, S. A., Zhai, J., Denev, S., Gopalan, V. & MacManus-Driscoll, J. L. Thick lead-free ferroelectric films with high Curie temperatures through nanocomposite-induced strain. *Nat. Nanotechnol.* **6,** 491–495 (2011).

68. Schlom, D. G., Chen, L., Fennie, C. J., Gopalan, V. & Uecker, R. Elastic strain engineering of ferroic oxides. *MRS Bull.* **39,** 118–130 (2014).

69. Harrington, S. A., Zhai, J., Denev, S., Gopalan, V. & MacManus-Driscoll, J. L. Thick lead-free ferroelectric films with high Curie temperatures through

nanocomposite-induced strain. *Nat. Nanotechnol.* **6,** 491–495 (2011).

70. Khatkhatay, F., Chen, A., Lee, J. H., Zhang, W. & Wang, H. Ferroelectric properties of vertically aligned nanostructured $BaTiO_3$-CeO_2 thin films and their integration on silicon. *ACS Appl. Mater. Interfaces* **5,** 12541–12547 (2013).

71. Lee, S. Lee, Shinbuhm, S., A., Lu, P., Chen, A. & MacManus-Driscoll, J. L. Novel electroforming-free nanoscaffold memristor with very high uniformity, tunability, and density. *Adv. Mater.* **26,** 6284–6289 (2014).

72. Hsieh, Y.-H., Liou, J., Huang, B., Liang, C. & Chu, Y. Local Conduction at the $BiFeO_3$-$CoFe_2O_4$ Tubular Oxide Interface. *Adv. Mater.* **24,** 4564–4568 (2012).

73. Zheng, H., Straub, F., Zhan, Q., Yang, P. & Ramesh, R. Self-assembled growth of $BiFeO_3$-$CoFe_2O_4$ nanostructures. *Adv. Mater.* **18,** 2747–2752 (2006).

74. Zhang, W., Chen, A., Jian, J., Zhu, Y. & Wang, H. Strong perpendicular exchange bias in epitaxial $La_{0.7}Sr_{0.3}MnO_3$:$BiFeO_3$ nanocomposite films through vertical interfacial coupling. *Nanoscale* **7,** 13808–15 (2015).

75. Zhang, W., Chen, A., Khatkhatay, F., Tsai, C. & Wang, H. Integration of Self-Assembled Vertically Aligned Nanocomposite $(La_{0.7}Sr_{0.3}MnO_3)_{1-x}$:$(ZnO)_x$ Thin Films on Silicon Substrates. *ACS Appl. Mater. Interfaces* **5,** 130502154440003 (2013).

76. Chen, A., Bi, Z., Tsai, C., Lee, J. & Wang, H. Tunable Low-Field Magnetoresistance in $(La_{0.7}Sr_{0.3}MnO_3)_{0.5}$:$(ZnO)_{0.5}$ Self-Assembled Vertically Aligned Nanocomposite Thin Films. *Adv. Funct. Mater.* **21,** 2423–2429 (2011).

77. Zhang, W., Li, L., Lu, P., Fan, M. & Wang, H. Perpendicular Exchange-Biased

Magnetotransport at the Vertical Heterointerfaces in $La_{0.7}Sr_{0.3}MnO_3$:NiO Nanocomposites. *ACS Appl. Mater. Interfaces* **7,** 21646–21651 (2015).

78. Ning, X., Wang, Z. & Zhang, Z. Controllable Self-Assembled Microstructures of $La_{0.7}Ca_{0.3}MnO_3$:NiO Nanocomposite Thin Films and Their Tunable Functional Properties. *Adv. Mater. Interfaces* **2,** 1500302 (2015).

79. Chen, A., Bi, Z., Hazariwala, H., Zhang, X. & Wang, H. Microstructure, magnetic, and low-field magnetotransport properties of self-assembled $(La_{0.7}Sr_{0.3}MnO_3)_{0.5}$:$(CeO_2)_{0.5}$ vertically aligned nanocomposite thin films. *Nanotechnology* **22,** 315712 (2011).

80. Cao, J. & Wu, J. Strain effects in low-dimensional transition metal oxides. *Mater. Sci. Eng. R Reports* **71,** 35–52 (2011).

81. Sun, Y., Thompson, S. E. & Nishida, T. Strain effect in semiconductors: Theory and device applications. *Springer* (2010). doi:10.1007/978-1-4419-0552-9

82. Chu, M., Sun, Y., Aghoram, U. & Thompson, S. E. Strain: A Solution for Higher Carrier Mobility in Nanoscale MOSFETs. *Annu. Rev. Mater. Res.* **39,** 203–229 (2009).

83. Guinea, F., Katsnelson, M. I. & Geim, A. K. Energy gaps and a zero-field quantum Hall effect in graphene by strain engineering. *Nat. Phys.* **6,** 30–33 (2010).

84. Yun, W. S., Han, S. W., Hong, S. C., Kim, I. G. & Lee, J. D. Thickness and strain effects on electronic structures of transition metal dichalcogenides: 2H-MX_2 semiconductors (M= Mo, W; X= S, Se, Te) *Phys. Rev. B* **85,** 33305 (2012).

85. Liu, Y. Li, Y. Y., Rajput, S., Gilks, D. & Li, L. Tuning Dirac states by strain in the

topological insulator Bi_2Se_3. *Nat. Phys.* **10,** 1–6 (2014).

86. Sato, H. & Naito, M. Increase in the superconducting transition temperature by anisotropic strain effect in (001) $La_{1.85}Sr_{0.15}CuO_4$ thin films on $LaSrA1O_4$ substrates. *Phys. C* **274,** 221–226 (1997).

87. Zeches, R. J., Rossell, M. D., Zhang, J. X., Hatt, A. J. & Ramesh, R. A strain-driven morphotropic phase boundary in $BiFeO_3$. *Science* **326,** 977–980 (2009).

88. Choi, K. J., Biegalski, M., Li, Y. L., Sharan, A. & Eom, C. B. Enhancement of Ferroelectricity in Strained $BaTiO_3$ Thin Films. *Science* **306,** 1005–1009 (2004).

89. Schlom, D. G., Chen, L., Eom, C. B., Rabe, K. M. & Triscone, J. M. Strain Tuning of Ferroelectric Thin Films. *Annu. Rev. Mater. Res.* **37,** 589–626 (2007).

90. Takamura, Y., Chopdekar, R. V, Arenholz, E. & Suzuki, Y. Control of the magnetic and magnetotransport properties of $La_{0.67}Sr_{0.33}MnO_3$ thin films through epitaxial strain. *Appl. Phys. Lett.* **92,** 162504 (2008).

91. Adamo, C., Ke, X., Wang, H. Q., Xin, H. L. & Schlom, D. G. Effect of biaxial strain on the electrical and magnetic properties of (001) $La_{0.7}Sr_{0.3}MnO_3$ thin films. *Appl. Phys. Lett.* **95,** 112504 (2009).

92. Chen, A., Zhou, H., Bi, Z., Zhu, Y. & Wang, H. A new class of room-temperature multiferroic thin films with bismuth-based supercell structure. *Adv. Mater.* **25,** 1028–1032 (2013).

93. Lee, J. H., Fang, L., Vlahos, E., Ke, X. & Schlom, D. G. A strong ferroelectric ferromagnet created by means of spin-lattice coupling. *Nature* **466,** 954–8 (2010).

94. Haeni, J. H., Irvin, P., Chang, W., Uecker, R. & Schlom, D. G. Room-temperature

ferroelectricity in strained $SrTiO_3$. *Nature* **430,** 758–761 (2004).

95. Eerenstein, W., Mathur, N. D., Scott, J. F. & F, J. Scott: Multiferroic and magnetoelectric materials. *Nature* **442759,** 759–765 (2006).

96. Chen, Z., Luo, Z., Huang, C., Qi, Y. & Chen, L. Low-symmetry monoclinic phases and polarization rotation path mediated by epitaxial strain in multiferroic $BiFeO_3$ thin films. *Adv. Funct. Mater.* **21,** 133–138 (2011).

97. Lebeugle, D., Colson, D., Forget, A. & Viret, M. Very large spontaneous electric polarization in $BiFeO_3$ single crystals at room temperature and its evolution under cycling fields. *Appl. Phys. Lett.* **91,** 22907 (2007).

98. Hatt, A. J., Spaldin, N. A. & Ederer, C. Strain-induced isosymmetric phase transition in $BiFeO_3$. *Phys. Rev. B - Condens. Matter Mater. Phys.* **81,** (2010).

99. Sando, D., Agbelele, A., Daumont, C., Rahmedov, D. & Bibes, M. Control of ferroelectricity and magnetism in multi-ferroic $BiFeO_3$ by epitaxial strain. *Philos. Trans. A. Math. Phys. Eng. Sci.* **372,** 20120438 (2014).

100. Kim, D. H., Lee, H. N., Biegalski, M. D. & Christen, H. M. Effect of epitaxial strain on ferroelectric polarization in multiferroic $BiFeO_3$ films. *Appl. Phys. Lett.* **92,** 012911 (2008).

101. Zhang, J. X., He, Q., Trassin, M., Luo, W. & Ramesh, R. Microscopic origin of the giant ferroelectric polarization in tetragonal-like $BiFeO_3$. *Phys. Rev. Lett.* **107,** 147602 (2011).

102. Jang, H. W., Baek, S. H., Ortiz, D., Folkman, C. M. & Eom, C. B. Strain-induced polarization rotation in epitaxial (001) $BiFeO_3$ thin films. *Phys. Rev. Lett.* **101,**

107602 (2008).

103. Li, Y. L. & Chen, L. Q. Temperature-strain phase diagram for $BaTiO_3$ thin films. *Appl. Phys. Lett.* **88,** 72905 (2006).

104. Damodaran, A. R., Breckenfeld, E., Chen, Z., Lee, S. & Martin, L. W. Enhancement of ferroelectric curie temperature in $BaTiO_3$ films via strain-induced defect dipole alignment. *Adv. Mater.* **26,** 6341–6347 (2014).

105. Li, Y. L., Choudhury, S., Haeni, J. H., Biegalski, M. D. & Chen, L. Q. Phase transitions and domain structures in strained pseudocubic (100) $SrTiO_3$ thin films. *Phys. Rev. B - Condens. Matter Mater. Phys.* **73,** 184112 (2006).

106. Jin, S., Tiefel, T. H., McCormack, M., Fastnacht, R. & Chen, L. H. Thousandfold change in resistivity in magnetoresistive $LaCaMnO_3$ films. *Science* **264,** 413–5 (1994).

107. Fang, Z. & Terakura, K. Surface Magnetic Phase Diagram of Tetragonal Manganites. *J. Phys. Soc. Japan* **70,** 3356–3361 (2001).

108. Pesquera, D., Herranz, G., Barla, A., Pellegrin, E. & Fontcuberta, J. Surface symmetry-breaking and strain effects on orbital occupancy in transition metal perovskite epitaxial films. *Nat. Commun.* **3,** 1189 (2012).

109. Wang, B., You, L., Ren, P., Yin, X. & Wang, J. Oxygen-driven anisotropic transport in ultra-thin manganite films. *Nat. Commun.* **4,** 2778 (2013).

110. Cui, B., Song, C., Wang, G. Y., Mao, H. J. & Pan, F. Strain engineering induced interfacial self-assembly and intrinsic exchange bias in a manganite perovskite film. *Sci. Rep.* **3,** 2542 (2013).

111. Xie, Q. Y., Wu, X. S., Gao, J. & Jia, Q. J. Exchange bias induced by the fully strained $La_{2/3}Ca_{1/3}MnO_3$ dead layers. *J. Appl. Phys.* **115,** 10–13 (2014).

112. Aimon, N. M., Choi, H. K., Sun, X. Y., Kim, D. H. & Ross, C. A. Templated Self-Assembly of Functional Oxide Nanocomposites. *Adv. Mater.* **26,** 3063–3067 (2014).

113. Choi, H. K., Aimon, N. M., Kim, D., Sun, X. Y. & Ross, C. A. Hierarchical templating of a $BiFeO_3$-$CoFe_2O_4$ multiferroic nanocomposite by a triblock terpolymer film. *ACS Nano* **8,** 9248–9254 (2014).

114. Comes, R., Liu, H., Khokhlov, M., Kasica, R. & Wolf, S. Directed self-assembly of epitaxial $CoFe_2O_4$-$BiFeO_3$ multiferroic nanocomposites. *Nano Lett.* **12,** 2367–73 (2012).

115. Stratulat, S. M., Lu, X., Morelli, A., Hesse, D. & Alexe, M. Nucleation-induced self-assembly of multiferroic $BiFeO_3$-$CoFe_2O_4$ nanocomposites. *Nano Lett.* **13,** 3884–9 (2013).

116. Okada, K., Sakamoto, T., Fujiwara, K., Hattori, A. N. & Tanaka, H. Three dimensional nano-seeding assembly of ferromagnetic Fe/$LaSrFeO_4$ nano-hetero dot array. *J. Appl. Phys.* **112,** 0–7 (2012).

117. Sakamoto, T., Okada, K., Hattori, A. N., Kanki, T. & Tanaka, H. Position-controlled functional oxide lateral heterostructures consisting of artificially aligned $(Fe,Zn)_3O_4$ nanodots and $BiFeO_3$ matrix. *Nanotechnology* **23,** 335302 (2012).

118. Zheng, H., Zhan, Q., Zavaliche, F., Sherburne, M. & Ramesh, R. Controlling self-assembled perovskite-spinel nanostructures. *Nano Lett.* **6,** 1401–1407 (2006).

119. Zhan, Q., Yu, R., Crane, S. P., Zheng, H. & Ramesh, R. Structure and interface chemistry of perovskite-spinel nanocomposite thin films. *Appl. Phys. Lett.* **89,** (2006).

120. Prakash, B. & Chakraverty, S. Realization of atomically flat steps and terraces like surface of $SrTiO_3$ (001) single crystal by hot water etching and high temperature annealing. *Solid State Commun.* **213–214,** 28–30 (2015).

121. Solmaz, A., Huijben, M., Koster, G., Egoavil, R. & Rijnders, G. Domain Selectivity in $BiFeO_3$ Thin Films by Modified Substrate Termination. *Adv. Funct. Mater.* **3,** 201505065 (2016).

122. Connell, J. G., Isaac, B. J., Ekanayake, G. B., Strachan, D. R. & Seo, S. S. A. Preparation of atomically flat $SrTiO_3$ surfaces using a deionized-water leaching and thermal annealing procedure. *Appl. Phys. Lett.* **101,** 48–51 (2012).

123. Sánchez, F., Ocal, C. & Fontcuberta, J. Tailored surfaces of perovskite oxide substrates for conducted growth of thin films. *Chem. Soc. Rev.* **43,** 2272–85 (2014).

124. Sanchez, F., Arcia-Cuenca, M., Errater, C., Arela, M. & Ontcuberta, J. Transition from three- to two-dimensional growth in strained $SrRuO_3$ ilms on $SrTiO_3$ (001). *Appl. Phys. Lett.* **83,** 902–904 (2003).

125. Baeumer, C., Xu, C., Gunkel, F., Raab, N. & Dittmann, R. Surface Termination Conversion during $SrTiO_3$ Thin Film Growth Revealed by X-ray Photoelectron Spectroscopy. *Sci. Rep.* **5,** 11829 (2015).

126. Bachelet, R., Sánchez, F., Santiso, J., Munuera, C. & Fontcuberta, J. Self-Assembly of $SrTiO_3$ (001) Chemical-Terminations: A Route for Oxide-Nanostructure

Fabrication by Selective Growth. *Chem. Mater.* **21,** 2494–2498 (2009).

127. Foerster, M., Bachelet, R., Laukhin, V., Fontcuberta, J. & Herranz, G. Laterally confined two-dimensional electron gases in self-patterned $LaAlO_3/SrTiO_3$ interfaces. *Appl. Phys. Lett.* **100,** 231607 (2012).

128. Agilent Technologies. Atomic Force Microscopy (2012). at <http://www.home.agilent.com/agilent/editorial.jspx?cc=MX&lc=spa&ckey=1774141&nid=-33986.0.02&id=1774141>

129. R. von Helmolt, J. Wecker, B. Holzapfel, L. Schultz, & K. S. Giant negative magnetoresistance in perovskitelike $La_{2/3}Ba_{1/3}MnO_x$ ferromagnetic films. *Phys. Rev. Lett.* **71,** 2331–2333 (1993).

130. Li, X. W., Gupta, A., Xiao, G. & Gong, G. Q. Low-field magnetoresistive properties of polycrystalline and epitaxial perovskite manganite films. *Appl. Phys. Lett.* **71,** 1124 (1997).

131. Balcells, L., Carrillo, a E., Martinez, B. & Fontcuberta, J. Enhanced field sensitivity close to percolation in magnetoresistive $La_{2/3}Sr_{1/3}MnO_3/CeO_2$ composites. *Appl. Phys. Lett.* **74,** 4014–4016 (1999).

132. Mitani, S., Takahashi, S., Takanashi, K., Yakushiji, K. & Fujimori, H. Enhanced Magnetoresistance in Insulating Granular Systems: Evidence for Higher-Order Tunneling. *Phys. Rev. Lett.* **81,** 2799–2802 (1998).

133. Chen, A., Bi, Z., Hazariwala, H., Zhang, X. & Wang, H. Microstructure, magnetic, and low-field magnetotransport properties of self-assembled $(La_{0.7}Sr_{0.3}MnO_3)_{0.5}:(CeO_2)_{0.5}$ vertically aligned nanocomposite thin films.

Nanotechnology **22,** 315712 (2011).

134. Staruch, M., Hires, D., Chen, A., Bi, Z. & Jain, M. Enhanced low-field magnetoresistance in $La_{0.67}Sr_{0.33}MnO_3$: MgO composite films. *J. Appl. Phys.* **110,** 113913 (2011).

135. Chen, A., Zhang, W., Khatkatay, F., Su, Q. & Wang, H. Magnetotransport properties of quasi-one-dimensionally channeled vertically aligned heteroepitaxial nanomazes. *Appl. Phys. Lett.* **102,** 093114 (2013).

136. Bi, Z., Luo, H., Chen, A., MacManus-Driscoll, J. L. & Wang, H. Microstructural and magnetic properties of $(La_{0.7}Sr_{0.3}MnO_3)_{0.7}$:$(Mn_3O_4)_{0.3}$ nanocomposite thin films. *J. Appl. Phys.* **109,** 54302 (2011).

137. Gillen, R., Clark, S. J. & Robertson, J. Nature of the electronic band gap in lanthanide oxides. *Phys. Rev. B - Condens. Matter Mater. Phys.* **87,** 125116, (2013).

138. Bi, L., Kim, H. S., Dionne, G. F., Ross, C. A. & Park, Y. C. Orientation control and self-assembled nanopyramid structure of $LaFeO_3$ films epitaxially grown on $SrTiO_3$ (001) substrates. *Appl. Phys. Lett.* **95,** 121908 (2009).

139. Adamo, C., Ke, X., Wang, H. Q., Xin, H. L. & Schlom, D. G. Effect of biaxial strain on the electrical and magnetic properties of (001) $La_{0.7}Sr_{0.3}MnO_3$ thin films. *Appl. Phys. Lett.* **95,** 112504 (2009).

140. Millis, a J., Darling, T. & Migliori, A. Quantifying strain dependence in 'colossal' magnetoresistance manganites. *J. Appl. Phys.* **83,** 1588 (1998).

141. Kumar, N., Khurana, G., Gaur, A. & Kotnala, R. K. Room temperature low field magnetoresistance in $Sr_2FeMoO_6/Zn_xFe_{1-x}Fe_2O_4$ composites. *J. Appl. Phys.* **114,**

53902 (2013).

142. Chen, A., Hu, J., Lu, P., Yang, T. & Jia, Q. Role of scaffold network in controlling strain and functionalities of nanocomposite films. *Sci. Adv.* **2,** 1–10 (2016).

143. Sr, L., Cuo, M. & Al, O. Effect of second introduced phase on magnetotransport properties of. *Mater. Sci.* **33,** 2–8 (2008).

144. Díaz-Guerra, C., Vila, M. & Piqueras, J. Exchange bias in single-crystalline CuO nanowires. *Appl. Phys. Lett.* **96,** 18–21 (2010).

145. Radu, F., Abrudan, R., Radu, I., Schmitz, D. & Zabel, H. Perpendicular exchange bias in ferrimagnetic spin valves. *Nat. Commun.* **3,** 715 (2012).

146. Ikeda, S., Miura, K., Yamamoto, H., Mizunuma, K. & Ohno, H. A perpendicular-anisotropy CoFeB-MgO magnetic tunnel junction. *Nat. Mater.* **9,** 721–724 (2010).

147. Maat, S., Takano, K., Parkin, S. & Fullerton, E. Perpendicular Exchange Bias of Co/Pt Multilayers. *Phys. Rev. Lett.* **87,** 87202 (2001).

148. Huang, J., Tsai, C., Chen, L., Jian, J. & Wang, H. Magnetic properties of $(CoFe_2O_4)x:(CeO_2)_{1-x}$ vertically aligned nanocomposites and their pinning properties in $YBa_2Cu_3O_{7-\delta}$ thin films. *J. Appl. Phys.* **115,** 123902(1)-123902(7) (2014).

149. Zhang, W., Fan, M., Li, L., Chen, A. & Wang, H. Heterointerface design and strain tuning in epitaxial $BiFeO_3$: $CoFe_2O_4$ nanocomposite films. *Appl. Phys. Lett.* **107,** 212901 (2015).

150. Fujii, T., Matsusue, I. & Takada, J. Superparamagnetic Behaviour and Induced Ferrimagnetism of $LaFeO_3$ Nanoparticles Prepared by a Hot-Soap Technique. *Adv.*

Asp. Spectrosc. (2012). at <http://cdn.intechopen.com/pdfs-wm/38538.pdf>

151. Lee, S., Zhang, W., Khatkhatay, F., Jia, Q. & Macmanus-Driscoll, J. L. Strain Tuning and Strong Enhancement of Ionic Conductivity in $SrZrO_3$-RE_2O_3 (RE = Sm, Eu, Gd, Dy, and Er) Nanocomposite Films. *Adv. Funct. Mater.* **25,** 4328–4333 (2015).

152. Nolting, F., Scholl, A., Stohr, J., Seo, J. W. & Padmore, H. A. Direct observation of the alignment of ferromagnetic spins by antiferromagnetic spins. *Nature* **405,** 767–9 (2000).

153. Cui, B., Song, C., Wang, G. Y., Mao, H. J. & Pan, F. Strain engineering induced interfacial self-assembly and intrinsic exchange bias in a manganite perovskite film. *Sci. Rep.* **3,** 2542 (2013).

154. Yu, T., Ning, X. K., Liu, W., Feng, J. N. & Zhang, Z. D. Exchange bias effect in epitaxial $La_{0.67}Ca_{0.33}MnO_3/SrMnO_3$ thin film structure. *J. Appl. Phys.* **116,** 83908 (2014).

155. Ding, J. F., Lebedev, O. I., Turner, S., Tian, Y. F. & Wu, T. Interfacial spin glass state and exchange bias in manganite bilayers with competing magnetic orders. *Phys. Rev. B - Condens. Matter Mater. Phys.* **87,** 1–7 (2013).

156. Ning, X. K., Wang, Z. J., Zhao, X. G., Shih, C. W. & Zhang, Z. D. Exchange bias in $La_{0.7}Sr_{0.3}MnO_3$/NiO and $LaMnO_3$/NiO interfaces. *J. Appl. Phys.* **113,** (2013).

157. Ning, X., Wang, Z., Zhao, X., Shih, C. & Zhang, Z. Exchange Bias Effect and Magnetic Properties in $La_{0.7}Sr_{0.3}MnO_3$: NiO Nanocomposite Films. *IEEE Trans. Magn.* **50,** 1–4 (2014).

158. Patra, M., De, K., Majumdar, S. & Giri, S. Exchange bias with Fe substitution in $LaMnO_3$. *Eur. Phys. J. B* **58,** 367–371 (2007).

159. Alonso, J., Fdez-Gubieda, M. L., Barandiarán, J. M., Svalov, A. & Orue, I. Crossover from superspin glass to superferromagnet in Fe_xAg_{100-x} nanostructured thin films ($20 \leq x \leq 50$). *Phys. Rev. B* **82,** 54406 (2010).

160. Takamura, Y., Folven, E., Shu, J. B. R., Lukes, K. R. & Grepstad, J. K. Spin-flop coupling and exchange bias in embedded complex oxide micromagnets. *Phys. Rev. Lett.* **111,** 1–5 (2013).

161. Yu, P., Lee, J. S., Okamoto, S., Rossell, M. D. & Ramesh, R. Interface ferromagnetism and orbital reconstruction in $BiFeO_3$-$La_{0.7}Sr_{0.3}MnO_3$ heterostructures. *Phys. Rev. Lett.* **105,** (2010).

162. Ong, Q. K., Wei, A. & Lin, X. M. Exchange bias in Fe/ Fe_3O_4 core-shell magnetic nanoparticles mediated by frozen interfacial spins. *Phys. Rev. B - Condens. Matter Mater. Phys.* **80,** 1–6 (2009).

163. Rui, W. B., Hu, Y., Du, A., You, B. & Du, J. Cooling field and temperature dependent exchange bias in spin glass/ferromagnet bilayers. *Sci. Rep.* 1–10 (2015).

164. Del Bianco, L., Fiorani, D., Testa, A. M., Bonetti, E. & Signorini, L. Field-cooling dependence of exchange bias in a granular system of Fe nanoparticles embedded in an Fe oxide matrix. *Phys. Rev. B - Condens. Matter Mater. Phys.* **70,** 6–9 (2004).

165. Tang, Y. K., Sun, Y. & Cheng, Z. H. Exchange bias associated with phase separation in the perovskite cobaltite La1-x Srx CoO3. *Phys. Rev. B - Condens. Matter Mater. Phys.* **73,** (2006).

166. Olena Gomonay, I. L. Magnetostriction-induced anisotropy in the exchange biased bilayers. *Metallofiz. i Noveishie Technol.* **36,** 1453–1464 (2014).

167. Ali, M., Marrows, C. & Hickey, B. Onset of exchange bias in ultrathin antiferromagnetic layers. *Phys. Rev. B* **67,** 1–4 (2003).

168. Kung, K. T. Y., Louie, L. K. & Gorman, G. L. MnFe structure-exchange anisotropy relation in the NiFe/MnFe/NiFe system. *J. Appl. Phys.* **69,** 5634–5636 (1991).

169. Zhang, W., Chen, A., Jian, J., Zhu, Y. & Wang, H. Strong perpendicular exchange bias beyond thickness limitation through vertical interfacial coupling. *Nanoscale,* **7,** 13808-13815 (2015).

170. Fan, M., Zhang, W., Jian, J., Huang, J. & Wang, H. Strong perpendicular exchange bias in epitaxial $La_{0.7}Sr_{0.3}MnO_3$: $LaFeO_3$ nanocomposite thin films. *APL Mater.* **4,** 0–8 (2016).

171. Kawasaki, M., Maeda, T., Tsuchiya, R. & Koinuma, H. the $SrTiO_3$ Crystal Surface. *Science* **266,** 1–3 (1993).

172. Kawasaki, M., Prosandeev, S., Liu, J., Gan, C. & Chakhalian, J. Atomic control of the $SrTiO_3$ crystal surface. *Science* **266,** 1540 (1994).

173. Koster, G., Kropman, B. L., Rijnders, G. J. H. M., Blank, D. H. A. & Rogalla, H. Quasi-ideal strontium titanate crystal surfaces through formation of strontium hydroxide. *Appl. Phys. Lett.* **73,** 2920–2922 (1998).

174. Gunnarsson, R., Kalabukhov, A. S. & Winkler, D. Evaluation of recipes for obtaining single terminated perovskite oxide substrates. *Surf. Sci.* **603,** 151–157 (2009).

175. Woo, S., Jeong, H., Lee, S., Seo, H. & Choi, W. S. Surface properties of atomically flat poly-crystalline SrTiO3 . *Sci. Rep.* **5,** 8822 (2015).

176. Gibert, M., Puig, T., Obradors, X., Benedetti, A. & Hühne, R. Self-Organization of Heteroepitaxial CeO_2 Nanodots Grown from Chemical Solutions. *Adv. Mater.* **19,** 3937–3942 (2007).

177. Gibert, M., Abellán, P., Martínez, L., Román, E. & Obradors, X. Orientation and shape selection of self-assembled epitaxial $Ce_{1-x}Gd_xO_{2-y}$ nanostructures grown by chemical solution deposition. *CrystEngComm* **13,** 6719 (2011).